CDF/PHYS/BOTTOM/CDFR/10073
Version 1.1
March 3, 2010

Measurement of the Polarization Amplitudes of the $B_s \to \phi\phi$ decay

Mirco Dorigo[*], B. Di Ruzza,
Marco Rescigno, A.M. Zanetti

Abstract

In this note we present the first measurement of the polarization amplitudes for the charmless $B_s^0 \to \phi\phi \to [K^+K^-][K^+K^-]$ decay of the B_s^0 meson. The result is achieved using an unbinned Maximum Likelihood fit to the data collected by CDF II using the Two Track Trigger, in the period starting from March 2001 till April 2008, which corresponds to an integrated luminosity of 2.9 fb^{-1}. The yield consists of approximately 300 signal events.

The three estimated polarization amplitudes and the phase are:

$$\begin{aligned} |A_0|^2 &= 0.348 \pm 0.041(\text{stat}) \pm 0.021(\text{syst}) \\ |A_\parallel|^2 &= 0.287 \pm 0.043(\text{stat}) \pm 0.011(\text{syst}) \\ |A_\perp|^2 &= 0.365 \pm 0.044(\text{stat}) \pm 0.027(\text{syst}) \\ \cos\delta_\parallel &= -0.91^{+0.15(\text{stat})+0.09(\text{syst})}_{-0.13(\text{stat})-0.09(\text{syst})} \end{aligned}$$

and the resulting polarization fractions are:

$$\begin{aligned} f_\text{L} &= 0.348 \pm 0.041(\text{stat}) \pm 0.021(\text{syst}) \\ f_\text{T} &= 0.652 \pm 0.041(\text{stat}) \pm 0.021(\text{syst}) \end{aligned}$$

We perform the same analysis for the $B_s^0 \to J\psi\phi$ decay as well. The polarizations amplitudes we find are consistent with the published ones [1].

---

[*] mirco.dorigo@ts.infn.it

Contents

1 Introduction

We describe the analysis performed to measure the $B_s^0 \to \phi\phi$ polarization amplitudes. It is the natural evolution of the branching ratio measurement of this decay performed in 2005 with 180 pb^{-1} [2] and recently updated with 2.9 fb^{-1} of data [3]. This update represents the starting point of the present analysis: a sample of about 300 $B_s^0 \to \phi\phi$ events have been selected.

We perform an unbinned Maximum Likelihood fit to the mass and the three helicity angles distributions of the reconstructed B candidates. The mass distribution is used in the fit to discriminate the signal yield with respect to the background while the angular variables provide us with an insight on the polarization amplitudes. The fitter framework will be checked by three tests: the pseudo-experiments pulls distributions, the fit on realistic Monte Carlo data and the fit of the $B_s^0 \to J/\psi\phi$ decays selected with the Two Track Trigger. Because the $B_s^0 \to J\psi\phi$ decay properties are well known, this decay is a powerful control sample.

In the angular analysis of the topological similar decay $B_d^0 \to \phi K^{0\star}$ performed at CDF II [4], we have an yield of 60 events and the statistical uncertainty on the polarization amplitudes is of the order of 10%. In our $B_s^0 \to \phi\phi$ sample we have about a factor 4 in the events number, then we expect a factor 1/2 in the amplitude statistical uncertainties: they should be about 5%. The precision is sufficient to discriminate between various QCD predictions, provided the systematic uncertainty is kept at the same level.

The note is organized as follows:

Section 2 a summary of the main physics motivations for the study of the $B_s^0 \to \phi\phi$ decay in general and for the polarization amplitudes measurement in particular is given.

Section 3 the definition of the reference frames and the formalism used for the angular analysis are explained.

Section 4 briefly explains the data samples and the different trigger selections.

Section 5 the off-line selections for $B_s^0 \to \phi\phi$ and $B_s^0 \to J/\psi\phi$ and the $B_s^0 \to \phi\phi$ and $B_s^0 \to J/\psi\phi$ event yields are shown. The main sources of background are discussed.

Section 6 comparison of significant distributions between data and Monte Carlo simulations are presented.

Section 7 the fitting technique is introduced and it consists in an unbinned maximum likelihood fit of the reconstructed B candidates mass and the three helicity angles distributions of the B decay products. It is designed for the estimation of the polarization amplitudes. The fitter framework is checked by three tests: the pseudo-experiments pulls distributions, the fit of $B_s^0 \to J/\psi\phi$ decay as a control sample, and the fit on realistic MC data.

Section 8 further studies on the fit are presented.

Section 9 the systematics uncertainties are evaluated.

Section 10 provides the conclusions.

Appendix A the decay amplitudes as computed in the helicity and transversity basis are described.

Appendix B the technique to compute the normalization of the probability distribution functions of the likelihood are explained.

Appendix C reports the description and the performed analysis and tests of an earlier fitter version with a slightly different set of floating parameters.

Appendix D the analysis performed for the $B_s^0 \to J\psi\phi$ is described.

Appendix E a note on the test of goodness of fit is repoted.

Appendix F presents the EVTGEN decay files.

2 Physics Motivations

A class of B decays which is particularly intriguing involves processes whose principal contribution comes from $\bar{b} \to \bar{s}$ penguin amplitudes. The reason is that there are already several results in these processes conflicting with the current SM expectations. First, the CP asymmetry in $B_d^0 \to J/\psi K_{\mathrm{S}}$ should be approximately equal to that in penguin-dominated $\bar{b} \to \bar{s}q\bar{q}$ transitions ($q = u$, d, s) within the SM; however, on average, these latter measurements yield a smaller value [5, 6, 7, 8]. Second, within the SM, one expects no triple-product asymmetries in $B \to \phi K^\star$ [9].[1] Nonetheless, both BaBar and Belle have measured such effects, albeit at low statistical significance [10, 11]. Third, the data on $B \to \pi K$ branching ratios and CP asymmetries [12, 13, 14, 15, 16] appear to be inconsistent with a SM fit [17, 18].

In the same scenario, another powerful challenge occurs in $B \to V_1 V_2$ decays, where the V_i are light vector mesons. Such systems have the peculiar nature that the decay rate can be explained by the definition of three specific decay amplitudes: these correspond to the three possible relative angular momenta L between the vector mesons. In fact, for two spin 1 particles, L can be equal to 0, 1, or 2 to obtain the spin 0 initial state. Different formalisms could be involved in this description; the most suitable one makes use of three *polarization* amplitudes (one longitudinal and two transverse). Since these are observable quantities, they can be measured from an angular analysis of the decay products: the emission angles of the final states particles (*i. e.*, the products from the V_i mesons decays) have to be studied in a proper reference frame to separate the three decay amplitudes.[2] If the final-state is a CP-eigenstate, this disentanglement allows one to investigate the B system CP-properties.

Within the SM, the expectation is that these amplitudes result in a dominant longitudinal polarization, with the transversely-polarized amplitudes suppressed by a factor m_V/m_B. While this is experimentally confirmed for $B \to \rho\rho$ decays, which receive $\bar{b} \to \bar{d}$ penguin contributions, in $B \to \phi K^\star$, a $\bar{b} \to \bar{s}$ penguin decay, it has been measured that the transverse polarization is about equal to the longitudinal one [19, 20, 21]. This surprising result is known as “Polarization Puzzle”. This phenomenon could be more evident in the B meson decays involving penguin diagram, like the $B_s^0 \to \phi\phi$. New physics [22, 23], and SM [24, 25] explanations have been proposed.

---

[1] The triple-product for a B meson decay to two vector mesons takes the form $\vec{q} \cdot (\vec{\varepsilon_1} \times \vec{\varepsilon_2})$, where $\vec{q}$ is the momentum of one of the vector mesons; $\vec{\varepsilon_1}$ and $\vec{\varepsilon_2}$ are the polarizations of the two vector mesons.

[2] This quantities are complex number. Then, experimentally on can extract their moduli and relative phases. The three amplitudes satisfy a unitarity relation: the sum of the three squared moduli is equal to 1. Thus, they are usual expressed as percentages or fractions of total polarization.

The work presented here draws motivation from the above intriguing puzzles related to $\bar{b} \to \bar{s}$ penguin processes. The note describes the study of $B_s^0 \to \phi\phi$ decay. This is governed by the $\bar{b} \to \bar{s}$ transition and it is a pseudoscalar to vector-vector decay: it includes all the characteristics described above. Thus, it is an appealing candidates whose experimental analysis could bring more comprehension in the polarization puzzle as well as a better understanding of the low-energy strong interactions. Moreover, since each ϕ decay into two charged K mesons, the final state is a CP-eigenstate: this also offers the possibility to look for CP violations. Actually, this is an attractive topic because the first measurements of CP violation made at Tevatron for the B_s^0 mesons (in the $B_s^0 \to J/\psi\phi$ decay) seems not to be in agreement with the SM predictions [26, 27].

In addition, in the SM, the mixing-induced CP asymmetries in the dominant B_s^0 decay modes practically vanish: new physics is needed to change this prediction.[3] While such new contributions are likely to affect also B_d^0–$\bar{B}_d^0$ mixing, they appear in the B_d^0 system as a correction to a non-zero SM prediction for the mixing-induced CP asymmetry. In the B_s^0 system, however, the new physics contribution is a correction to essentially zero [28]. Thus, they could be easily tested: a non-zero measured asymmetry is an unequivocal new physics proof. Obviously, measurements of both direct and mixing-induced CP asymmetries require high statistics data sample. Indeed, these represent a very prominent goal of the b-physics program at the forthcoming experiments [29]. The polarization analysis, discussed in this note, is an intermediate and obliged step toward the achievement of that goal and can potentially already reveal the presence of new physics.

The aim of the analysis presented here is the first measurement of $B_s^0 \to \phi\phi$ polarization amplitudes. It is the natural evolution of the first branching ratio measurement of this decay in 2005, with 180 pb^{-1} of data collected by the CDF experiment at the Tevatron p$\bar{\text{p}}$ collider [2]. The latter was recently updated [3] with 2.9 fb^{-1} of data: this update represents the starting point of the present analysis.

2.1 Purpose and Current Experimental Status

The purpose of this note is the first measurements of the polarization amplitudes $|A_0|^2$, $|A_\parallel|^2$ and $|A_\perp|^2$ for the $B_s^0 \to \phi\phi$ decay. Their theoretical predictions can be done only with approximate methods: there are different approaches, some of them affected by large uncertainties. We summarize the predicted values of the longitudinal (f_L) and the transverse (f_T) polarization fractions in tab. 1.

These polarization measurements are of particular interest because they can help to understand the so-called "polarization puzzles", described below, related to $\bar{b} \to \bar{s}$ penguin processes. The interest in the polarization and CP-asymmetry measurements in penguin transition, such as $b \to s$ decays $B \to \phi K^\star$, $\rho K^\star$, $\omega K^\star$, and $b \to d$ decay $B \to K^\star \bar{K}^\star$, is mainly motivated by their potential sensitivity to physics beyond the SM.

The amplitude hierarchy $|A_0| \gg |A_\parallel| \simeq |A_\perp|$ (*i. e.*, $f_\text{L} \gg f_\text{T}$) was expected in the B decays to light vector particles in both the penguin transition [33] and the tree-level transition [34]. There is confirmation by BaBar and Belle experiments of predominantly longitudinal polarization in the tree-level $b \to u$ transition, such as $B^0 \to \rho^+\rho^-$ [35, 36], $B^+ \to \rho^0\rho^+$ [37], and $B^+ \to \omega\rho^+$ [38], which is consistent with the analysis of the quark helicity conservation [34]. Because the longitudinal amplitude dominates the decay, a detailed amplitude analysis is not possible with current B samples, and limits on the transverse amplitude fraction are obtained. Only limits have

---

[3] Because they are governed by the tiny phase $\arg(-V_{tb}V_{ts}^\star/V_{cb}V_{cs}^\star)$.

	f_{L} [%]	f_{T} [%]	Comments
QCD factorization 1.a	43^{+0+61}_{-0-34}	57^{+0+61}_{-0-34}	
QCD factorization 1.b	48^{+0+26}_{-0-27}	52^{+0+26}_{-0-27}	WA from data
QCD factorization 2	86.6	13.4	see erratum
Naive factorization	88.3	11.7	see erratum
NLO EWP 1	86.3	13.7	T and P
NLO EWP 2	86.3	13.7	T, P and EWP
perturbative QCD	$61.9^{+3.6+2.5+0.0}_{-3.2-3.3-0.0}$	$38.1^{+3.6+2.5+0.0}_{-3.2-3.3-0.0}$	

Table 1: $B_s \to \phi\phi$ polarization amplitudes: theoretical predictions. $\Gamma_{\mathrm{L}}/\Gamma$ and $(\Gamma_{\perp} + \Gamma_{\parallel})/\Gamma$ are the fraction of longitudinal and transverse polarisation, respectively. WA stands for "Weak Annihilation"; T, P and EWP stand for "Tree", "Penguin" and "Electroweak Penguin", respectively. The references are: [24] for QCD factorization 1.a and 1.b, [30] for QCD factorization 2 and Naive factorization, [31] for NLO EWP 1 and 2, [32] for perturbative QCD.

been set on the $B^0 \to \omega\rho^0$, $\omega\omega$ [38] and evidence found for $B^0 \to \rho^0\rho^0$ [39] decays, still indicating that $b \to d$ penguin pollution is small in the charmless, strangeless vector-vector B decays.

On the other hand, the decay amplitudes for $B \to \phi K^\star$ have been measured by the BaBar and Belle experiments [19, 40, 41] and the fractions of longitudinal polarization $f_{\mathrm{L}} = 0.50 \pm 0.05$ for the $B^+ \to \phi K^{\star +}$ decay, and $f_{\mathrm{L}} = 0.484 \pm 0.033$ for the $B^0 \to \phi K^{\star 0}$ decay, indicate significant departure from the naive expectation of predominant longitudinal polarization. These suggest other contributions to the decay amplitude, previously neglected, either within the SM, such as penguin annihilation [42] or QCD rescattering [43], or from physics beyond the SM [44].

The search for vector-tensor $B \to \phi K^\star_J$ decays with $J = 2, 3, 4$ revealed a large fraction of longitudinal polarization in the decay $B \to \phi K^\star_2(1430)$ with $f_{\mathrm{L}} = 0.85 \pm 0.08$ [19, 45]. Like $B \to \phi K^\star$, the decays $B \to \rho K^\star$ and $B \to \omega K^\star$ may be sensitive to new physics. Measurements of the longitudinal polarization fraction in $B^+ \to \rho^0 K^{\star 0}$ and $B^+ \to \rho^+ K^{\star 0}$ [46, 20] reveal a polarization anomaly similar to $B \to \phi K^\star$. At the same time, first measurement of the polarization in the $b \to d$ penguin decay $B^0 \to K^{\star 0}\bar{K}^{\star 0}$ indicates a large fraction of longitudinal polarization $f_{\mathrm{L}} = 0.81^{+0.12}_{-0.13}$ [47].

The measurement of polarization in the penguin dominated B_s decay could challenge the SM explanation of the polarization puzzle or at least can offer the opportunity to further constrain theoretical parameters thus improving the predictive power of current theoretical tools.

3 The $P \to VV$ decay: Angular Distributions

The nomenclature $P \to VV$ stands for the class of the decays of a Pseudoscalar meson (with $\mathsf{J}^{\mathsf{P}} = 0^-$), like the B, into two Vector mesons ($\mathsf{J} \neq 0$). The angular distribution of the B meson decay to two mesons with non-zero spin is of special interest because it is sensitive to quark-spin alignment in decay transition, and reflects both weak- and strong-interaction dynamics.

Most B-decay polarization analyses are limited to the case when the spin of the B-meson daughters is 1. In that case, there are only three independent amplitudes, corresponding to the probability that the B^0_s meson decays in a state with one of the three possible relative angular momenta: if L is the relative angular momentum of the two vector mesons, with two spin 1 particles one can have $L = 0$, 1, 2 to obtain the spin 0 of the initial state.

This is the case of the $B_s^0 \to \phi\phi$ and $B_s^0 \to J/\psi\phi$ decays studied here; remind that

$$\mathsf{J}^{\mathsf{PC}}[\phi] = 1^{--} \quad \text{and} \quad \mathsf{J}^{\mathsf{PC}}[J/\psi] = 1^{--} \tag{1}$$

In Appendix A the formalism and necessary definitions to describe the decays are reported. In the following subsections we present the formulae of the decay rates of interest.

3.1 $B_s^0 \to \phi\phi$

Let start with the main one: $B_s^0 \to \phi\phi$. The daughters state is made of two particles that are identical bosons: we need to choose a basis in which the two K^+K^- pairs from the two ϕ's are treated symmetrically, in order to obey Bose statistics. The natural basis that satisfy this requirement comes from the helicity formalism. Then, we treat the $B_s^0 \to \phi\phi$ decay using the three angles defined in eq. 39 (see Appendix A), $\vec{\omega} = (\vartheta_1, \vartheta_2, \Phi))$.

We mention in the Appendix A that the transversity basis has the advantage of a more easily treatment of the system CP properties. Since the final state in $B_s^0 \to \phi\phi$ is an admixture of CP-even and CP-odd eigenstates, we can use eq. 45a to obtain the polarization amplitudes. The resulting differential angular decay rate can be written as

$$\frac{d^4\Lambda(\vec{\omega}, t)}{dt d\vec{\omega}} = \frac{9}{32\pi} \sum_{i=1}^{6} K_i(t) f_i(\vec{\omega}) \tag{2}$$

where the angular functions $f_i(\vec{\omega})$ are given by

$$\begin{aligned}
f_1(\vec{\omega}) &= 4\cos^2\vartheta_1 \cos^2\vartheta_2 \\
f_2(\vec{\omega}) &= \sin^2\vartheta_1 \sin^2\vartheta_2 (1 + \cos 2\Phi) \\
f_3(\vec{\omega}) &= \sin^2\vartheta_1 \sin^2\vartheta_2 (1 - \cos 2\Phi) \\
f_4(\vec{\omega}) &= -2\sin^2\vartheta_1 \sin^2\vartheta_2 \sin 2\Phi \\
f_5(\vec{\omega}) &= \sqrt{2}\sin 2\vartheta_1 \sin 2\vartheta_2 \cos\Phi \\
f_6(\vec{\omega}) &= -\sqrt{2}\sin 2\vartheta_1 \sin 2\vartheta_2 \sin\Phi
\end{aligned} \tag{3}$$

while the time-dependent functions $K_i(t)$ are defined as

$$\begin{aligned}
K_1(t) =& \frac{1}{2}|A_0|^2 \left[(1+\cos\phi_{\rm s})e^{-\Gamma_{\rm L}t} + (1-\cos\phi_{\rm s})e^{-\Gamma_{\rm H}t} + 2e^{-\Gamma t}\sin(\Delta m t)\sin\phi_{\rm s} \right] \\
K_2(t) =& \frac{1}{2}|A_\parallel|^2 \left[(1+\cos\phi_{\rm s})e^{-\Gamma_{\rm L}t} + (1-\cos\phi_{\rm s})e^{-\Gamma_{\rm H}t} + 2e^{-\Gamma t}\sin(\Delta m t)\sin\phi_{\rm s} \right] \\
K_3(t) =& \frac{1}{2}|A_\perp|^2 \left[(1-\cos\phi_{\rm s})e^{-\Gamma_{\rm L}t} + (1+\cos\phi_{\rm s})e^{-\Gamma_{\rm H}t} - 2e^{-\Gamma t}\sin(\Delta m t)\sin\phi_{\rm s} \right] \\
K_4(t) =& |A_\parallel||A_\perp| \Bigg[e^{-\Gamma t}\Big(\sin(\delta_\perp - \delta_\parallel)\cos(\Delta m t) - \cos(\delta_\perp - \delta_\parallel)\sin(\Delta m t)\cos\phi_{\rm s} \Big) - \\
& - \frac{1}{2}\Big(e^{-\Gamma_{\rm H}t} - e^{-\Gamma_{\rm L}t} \Big)\cos(\delta_\perp - \delta_\parallel)\sin\phi_{\rm s} \Bigg] \\
K_5(t) =& \frac{1}{2}|A_0||A_\parallel|\cos(\delta_\parallel) \\
& \left[(1+\cos\phi_{\rm s})e^{-\Gamma_{\rm L}t} + (1-\cos\phi_{\rm s})e^{-\Gamma_{\rm H}t} + 2e^{-\Gamma t}\sin(\Delta m t)\sin\phi_{\rm s} \right] \\
K_6(t) =& |A_0||A_\perp| \Bigg[e^{-\Gamma t}\Big(\sin\delta_\perp\cos(\Delta m t) - \cos\delta_\perp\sin(\Delta m t)\cos\phi_{\rm s} \Big) - \\
& - \frac{1}{2}\Big(e^{-\Gamma_{\rm H}t} - e^{-\Gamma_{\rm L}t} \Big)\cos\delta_\perp\sin\phi_{\rm s} \Bigg]
\end{aligned} \tag{4}$$

The time-dependent angular distribution for a $\bar{B}_s^0$ meson can be obtained by reversing the sign of the terms proportional to $\sin(\Delta m t)$ or $\cos(\Delta m t)$ in the $K_i(t)$ functions. The symbols are defined in the following:

- the three polarization amplitudes are $|A_0|^2$, $|A_\parallel|^2$ and $|A_\perp|^2$;
- we denote the masses and widths of the two mass eigenstates with $M_{\rm H,L}$ and $\Gamma_{\rm H,L}$ and define

$$\Delta m = M_{\rm H} - M_{\rm L}\,, \tag{5a}$$

$$\Gamma = \frac{1}{\tau_B} = \frac{\Gamma_{\rm L} + \Gamma_{\rm H}}{2}\,, \tag{5b}$$

$$\Delta\Gamma = \Gamma_{\rm L} - \Gamma_{\rm H}; \tag{5c}$$

the last update results [48] for B_s meson are:

$$\Delta\Gamma_s = 0.062^{+0.034}_{-0.037}\,\text{ps}^{-1} \tag{6a}$$

$$\frac{\Delta\Gamma_s}{\Gamma_s} = 0.092^{+0.051}_{-0.054} \tag{6b}$$

$$\tau_{\rm L} = \frac{1}{\Gamma_{\rm L}} = 1.408^{+0.033}_{-0.030}\,\text{ps} \tag{6c}$$

$$\tau_{\rm H} = \frac{1}{\Gamma_{\rm H}} = 1.543^{+0.058}_{-0.060}\,\text{ps}. \tag{6d}$$

- The phase $\phi_{\rm s}$ is the physical phase related to the CP violation; in the SM, this phase can be expressed in terms of the CKM matrix elements that contribute to the respective mixing and decay diagrams:
$$\phi_{\rm s} \simeq \arg(V_{tb}V_{ts}^{\star})^2 - \arg(V_{cb}V_{cs}^{\star})^2 \tag{7}$$
and, because $\arg(V_{tb}V_{ts}^{\star}) \simeq \arg(V_{cb}V_{cs}^{\star})$ and the remaining corrections are small (because suppressed by a factor m_c^2/m_b^2), $\phi_{\rm s}^{\rm SM}$ is predicted to be very small [10]:
$$\phi_{\rm s}^{\rm SM} = 0.0041 \pm 0.0008. \tag{8}$$

- We define the two strong phases:
$$\begin{aligned} \delta_{\parallel} &= \arg(A_0^{\star}A_{\parallel}) \\ \delta_{\perp} &= \arg(A_0^{\star}A_{\perp}) \end{aligned} \tag{9}$$

Assuming that:

1. we are not able to distinguish a B_s^0 meson from a $\bar{B}_s^0$ meson and thus we have to sum over the B_s^0 and $\bar{B}_s^0$ terms of distribution[4];
2. we are not interested in measuring $\phi_{\rm s}$ and we assume its value in the SM. We then fix $\phi_{\rm s} = 0$ in the $K_i(t)$ functions;

then the differential angular decay rate of eq. 2 becomes

$$\frac{d^4\Lambda(\vec{\omega},t)}{dtd\vec{\omega}} = \frac{9}{32\pi}\Big[\mathcal{F}_{\rm e}(\vec{\omega})\mathcal{K}_{\rm L}(t) + \mathcal{F}_{\rm o}(\vec{\omega})\mathcal{K}_{\rm H}(t)\Big] \tag{10}$$

where we distinct two time-dependent and two angular-dependent terms:

$$\mathcal{F}_{\rm e}(\vec{\omega}) = |A_0|^2 f_1(\vec{\omega}) + |A_{\parallel}|^2 f_2(\vec{\omega}) + |A_0||A_{\parallel}|\cos\delta_{\parallel} f_5(\vec{\omega}) \tag{11a}$$
$$\mathcal{F}_{\rm o}(\vec{\omega}) = |A_{\perp}|^2 f_3(\vec{\omega}) \tag{11b}$$
$$\mathcal{K}_{\rm L}(t) = 2e^{-\Gamma_{\rm L}t} \tag{11c}$$
$$\mathcal{K}_{\rm H}(t) = 2e^{-\Gamma_{\rm H}t} \tag{11d}$$

A nice comment on eq. 10:

- $\mathcal{F}_{\rm e}(\vec{\omega}) \sim |\langle {\rm f}|B_{\rm L}\rangle|^2$ represents the probability to find the $|\phi\phi\rangle$ state with $L = 0$ or $L = 2$ (S- or D-wave): $\mathsf{CP}\,|\phi\phi\rangle = (-1)^L\,|\phi\phi\rangle = |\phi\phi\rangle$, then $\mathsf{CP}\,|B_{\rm L}\rangle = |B_{\rm L}\rangle$; the light mass (short-lived) eigenstate is also a CP-even eigenstate.

- $\mathcal{F}_{\rm o}(\vec{\omega}) \sim |\langle {\rm f}|B_{\rm H}\rangle|^2$ represents the probability to find the $|\phi\phi\rangle$ state with $L = 1$: $\mathsf{CP}\,|\phi\phi\rangle = (-1)^L\,|\phi\phi\rangle = -\,|\phi\phi\rangle$, then $\mathsf{CP}\,|B_{\rm H}\rangle = -\,|B_{\rm H}\rangle$; the heavy mass (long-lived) eigenstate is also a CP-odd eigenstate.

---

[4] We are supposing that B_s^0 and $\bar{B}_s^0$ are produced in equal numbers at the Tevatron.

3.2 $B_s^0 \rightarrow J/\psi\phi$

The customary choice for the $B_s^0 \rightarrow J/\psi\phi$ angular analysis is the transversity basis. The differential angular decay rate has the same form of eq. 2, with the $f_i(\vec{\Omega})$ functions defined by:

$$\begin{aligned}
f_1(\vec{\Omega}) &= 4\cos^2\Psi(1-\sin^2\Theta\cos^2\Phi) \\
f_2(\vec{\Omega}) &= \sin^2\Psi(1-\sin^2\Theta\sin^2\Phi) \\
f_3(\vec{\Omega}) &= \sin^2\Psi\sin^2\Theta \\
f_4(\vec{\Omega}) &= -\sin^2\Psi\sin 2\Theta\sin\Phi \\
f_5(\vec{\Omega}) &= \frac{1}{\sqrt{2}}\sin 2\Psi\sin^2\Theta\sin 2\Phi \\
f_6(\vec{\Omega}) &= \frac{1}{\sqrt{2}}\sin 2\Psi\sin 2\Theta\cos\Phi
\end{aligned} \tag{12}$$

and replacing ϕ_s with $2\beta_s$ in the $K_i(t)$ terms.

As for $B_s^0 \rightarrow \phi\phi$, if we sum over B_s^0 and $\bar{B}_s^0$ terms and assume for β_s the SM value ($\beta_s \simeq 0$), we get the analogous distribution for $B_s^0 \rightarrow J/\psi\phi$ as the one described by eq. 10.

4 Datasets and Triggers

The data was recorded in a period starting from March 2001 till April 2008. The used sample corresponds to an integrated luminosity of 2.9 fb^{-1} collected with the Two Track Trigger.

In this work, we refer to exclusive trigger configurations. These are defined as follow:

- `HIGHPT`: only `B_CHARM_HIGHPT`;
- `ScA` (Scenario A) : events selected by `B_CHARM_L1` and not by `B_CHARM_HIGHPT`;
- `LOWPT`: events selected by `B_CHARM_LOWPT` but not by both `B_CHARM_L1` and `B_CHARM_HIGHPT`.

Their percentages on the total sample are listed in tab. 2 for both decays. We request the matching between at least two reconstructed tracks and the SVT tracks. The confirmation of the `B_CHARM_LOWPT` trigger selections is imposed.

Trigger Paths	Fractions	
	$B_s^0 \rightarrow \phi\phi$	$B_s^0 \rightarrow J/\psi\phi$
`HIGHPT`	0.39 ± 0.05	0.42 ± 0.02
`ScA`	0.38 ± 0.05	0.33 ± 0.02
`LOWPT`	0.22 ± 0.04	0.26 ± 0.02

Table 2: Trigger paths fractions (exclusive selection).

5 Offline Selection and Decay Data Samples

In this section we briefly recall the results of the branching ratio analysis both for the $B_s^0 \rightarrow \phi\phi$ and the $B_s^0 \rightarrow J/\psi\phi$ decay. The reader should refer to [3] for details.

5.1 Useful Variables

We introduce some relevant quantities used in the analysis. All quantities are calculated in the laboratory frame and are illustrated in fig. 1 and their meaning is self-explanatory. They can be defined for each particles of the two decays of interest ($B_s^0 \to \phi\phi \to [K^+K^-][K^+K^-]$ and $B_s^0 \to J/\psi\phi \to [K^+K^-][\mu^+\mu^-]$).

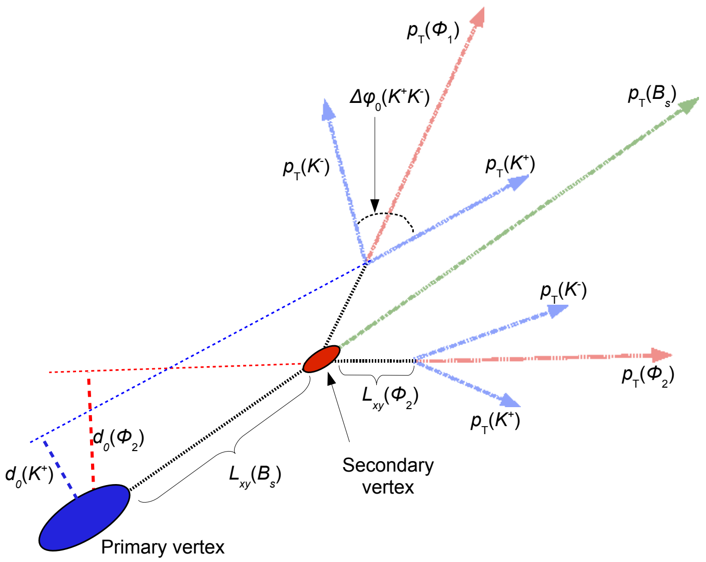

Figure 1: Sketch of the$B_s^0 \to \phi\phi \to [K^+K^-][K^+K^-]$ decay projected into the transverse plane. Ellipses indicate vertexes, arrows indicate the transverse momenta (*i. e.*, the direction) of charged particles. Nothing is to scale.

5.2 Offline Selection

Our data selection starts from the available `BStntuple` [49] of the hadronic dataset. Only kinematic variables are used, since these where the most reliable ones. These variables are:

- for the $B_s^0 \to \phi\phi$ decay:
  - L_{xy}^B: transverse decay length of the reconstructed B;
  - d_0^B: impact parameter of the reconstructed B;
  - $d_0^{\phi_{\max}}$: impact parameter of the ϕ with higher momentum;
  - $p_{\mathrm{T\,min}}^K$: transverse momentum of the softer kaon;
  - χ_{xy}^2: χ^2 of the fit used in the reconstruction of the secondary vertex;
- for the $B_s^0 \to J/\psi\phi$ decay:
  - L_{xy}^B: transverse decay length of the reconstructed B;

- d_0^B: impact parameter of the reconstructed B;
- p_{T}^{ϕ}: transverse momentum of the ϕ;
- $p_{\mathrm{T}}^{J/\psi}$: transverse momentum of the J/ψ;
- χ^2_{xy}: χ^2 of the fit used in the reconstruction of the secondary vertex;

The optimized cuts for the two signals selections are summarized in tab. 3.

Variables		Requirements	
		$B_s^0 \to \phi\phi$	$B_s^0 \to J/\psi\phi$
L_{xy}^B	[μm]	> 330	> 290
$p_{\mathrm{T\,min}}^K$	[GeV/c]	> 0.7	
p_{T}^{ϕ}	[GeV/c]		> 1.4
χ^2_{xy}		< 17	< 15
d_0^B	[μm]	< 65	< 80
$d_0^{\phi_{\max}}$	[μm]	> 85	
$p_{\mathrm{T}}^{J/\psi}$	[GeV/c]		> 2.0

Table 3: Optimized selection cuts.

5.3 The Final Data Sample

Applying the cuts listed in Tab.3, the invariant mass distributions, $m_{K^+K^-K^+K^-}$ for the $B_s^0 \to \phi\phi$ and $m_{K^+K^-\mu^+\mu^-}$ for the $B_s^0 \to J/\psi\phi$, are obtained (fig. 2 and fig. 3). These provides us with a first insight on the background and signal composition. In these distributions at least three components can be identified:

the signal: we have the following number of signal events:

	$B_s^0 \to \phi\phi$	$B_s^0 \to J/\psi\phi$
Yield	295 ± 20	1766 ± 48

These yields are extracted from a binned fit [3]: the fit function used is the sum of two gaussians (having the same mean value but different resolutions) and a decreasing exponential.

combinatorics background: these are random combinations of charged tracks accidentally satisfying the selection requirements. They produce a continuous invariant B_s^0 mass distribution and we expect a smooth slowing decreasing distribution in the signal region. It is the more important source of background in our analysis.

physics background: it is due to partially reconstructed heavy flavor decays or to an incorrect mass assignment to the tracks of other B meson decays (they are often referred to as *reflections*). We expect a distribution with a peak under the signal:

- for the $B_s^0 \to \phi\phi$: the decays that could produce reflections in the B_s^0 mass window are: $B_d^0 \to \phi K^\star \to [K^+K^-][K^{+(-)}\pi^{-(+)}]$ and $B_s^0 \to \bar{K}^\star K^\star \to [K^{+(-)}\pi^{-(+)}][K^{+(-)}\pi^{-(+)}]$; these reflections occur when the $K^\star$ is incorrectly reconstructed as a ϕ. The estimated number of reflection events is [3]:

	$B_s^0 \to \bar{K}^\star K^\star$	$B_d^0 \to \phi K^\star$
Events	0	8 ± 3
Fraction respect to signal events [%]	10^{-6}	3 ± 1

  Since its tiny percentage respect to the signal events, the $B_d^0 \to \bar{K}^\star K^\star$ reflection is neglected.

- for the $B_s^0 \to J/\psi\phi$: the more frequent background decay is the $B_d^0 \to J/\psi K^\star \to [\mu^+\mu^-][K^{+(-)}\pi^{-(+)}]$ decay; it occurs when in the reconstruction the daughter tracks of the $K^\star$ are assumed to be two kaons and an incorrect invariant mass is computed. The estimated number of reflection events is [3]:

	$B_d^0 \to J/\psi K^\star$
Events	70 ± 20
Fraction respect to signal events [%]	4 ± 1

6 Monte Carlo Data and its Validation

In this analysis, simulation of B production and decay processes and of the subsequent detector response is used for several reasons:

- to model physics background;
- to model the acceptance of the combined detector and trigger system in the space of helicity (transversity) angular variables;
- to test the fitter framework;
- to estimate some systematic uncertainties.

We used the chain BGENERATOR + EVTGEN + CDFSIM [50, 51, 52] and the output of the MC simulation is processed with the `BStntuple` software which reconstructs B decays and writes the output events in the `BStntuple` format. The $B \to VV$ decay is modeled through EVTGEN in different ways in order to produce samples for specific purposes as described in the following.

In order to model the angular acceptance for both $B_s^0 \to \phi\phi$ and $B_s^0 \to J/\psi\phi$ decays large samples (respectively $40 \cdot 10^6$ and $20 \cdot 10^6$ events) have been generated using the `PHSP` decay model in EVTGEN that performs the decay using only phase space, averaging all final state spin values and without taking into account any spin correlations between the two vectors in the final state. This amounts to generate all possible angular configurations of final state particles allowing to easily derive the 3D acceptance function described in Sec. 7.

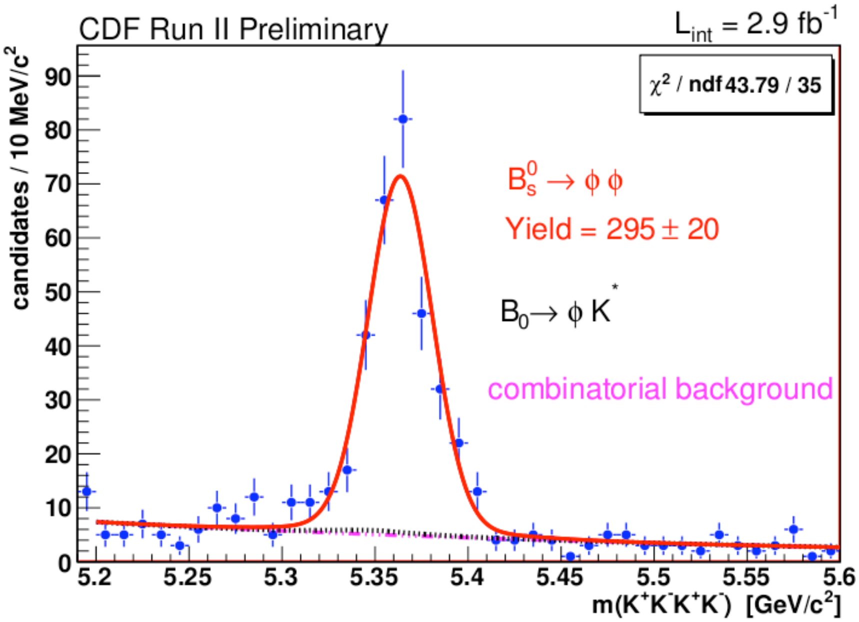

Figure 2: Background and signal composition in the $B_s^0 \to \phi\phi$ decay. The blue points represent data after the optimized selection; the red line is the total fit distribution; in black the reflection component; in purple the combinatorial background.

In order to study specific polarization amplitudes for the $B_s^0 \to \phi\phi$ and $B_s^0 \to J/\psi\phi$ decays realistic MC samples were generated using the `SVV_HELAMP` decay models. This model is completly specified giving a set of polarization amplitudes in the helicity base. In Appendix F we report some of the `SVV_HELAMP` decay files used in this analysis. One further detail worth to be discussed here is that the `SVV_HELAMP` decay model do not handle at all the lifetime difference of B_s^0 mesons eigen-states. To emulate effects related to $\Delta\Gamma_s$ we generate separate CP-even and CP-odd sample with relative amount of events dictated by the wanted transverse perpendicular polarization fraction. We then evolve the CP-even and CP-odd sample modifying the input ${B_s^0}_L$ and ${B_s^0}_H$ values by using custom "pdt" tables. In order to reproduce the single exponential behaviour of the CP-even and CP-odd sample we need to fix both ${B_s^0}_L$ and ${B_s^0}_H$ lifetime to a single value.

6.1 Monte Carlo and Data Comparison

The realistic run dependent Monte Carlo simulation have been extensively validated for the $B_s^0 \to \phi\phi$ branching ratio measurement [3], we refer to the available documentation for a number of plots showing the ability of the simulation to reproduce relevant kinematic distributions for both the abundant $B_s^0 \to J/\psi\phi$ events as well as for the rarer $B_s^0 \to \phi\phi$ decays.

The study in [3] found that the MC input B p_T spectrum is significantly softer that it should be to match the data. An additional p_T re-weigthing procedure has been adopted to correct for this, and is mantained in the current analysis. This is based on the Data/MC comparision of B_s^0 p_T using the large sample of $B_s^0 \to J/\psi\phi$ events. The ratio of Data over Monte Carlo simulated events is shown in Fig. 4 as a function of B_s^0 p_T. The overalaid first order polynomial fit will be

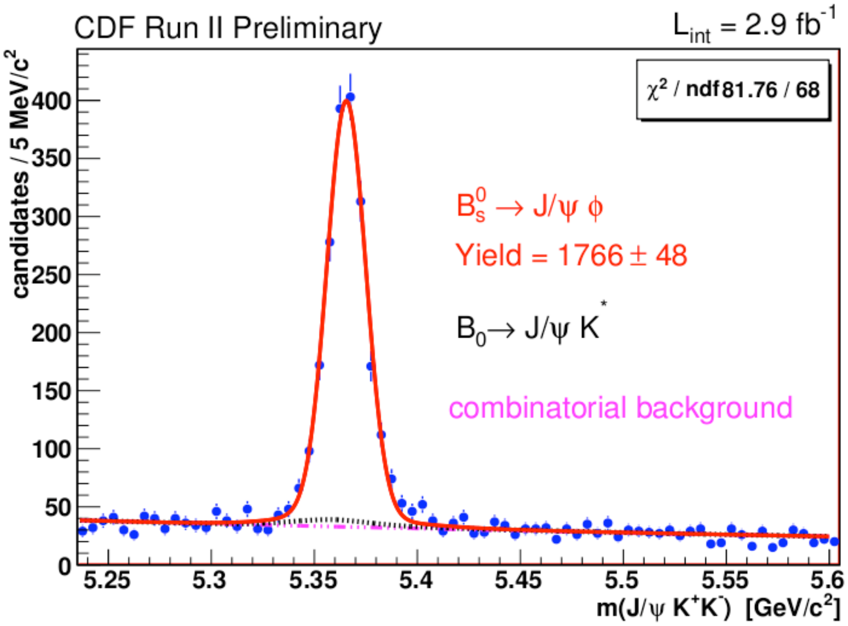

Figure 3: Background and signal composition in the $B_s^0 \to J/\psi\phi$ decay. The blue points represent the data satisfying the off-line selection; the red line is the total fit distribution; in black the reflection component; in purple the combinatorial background.

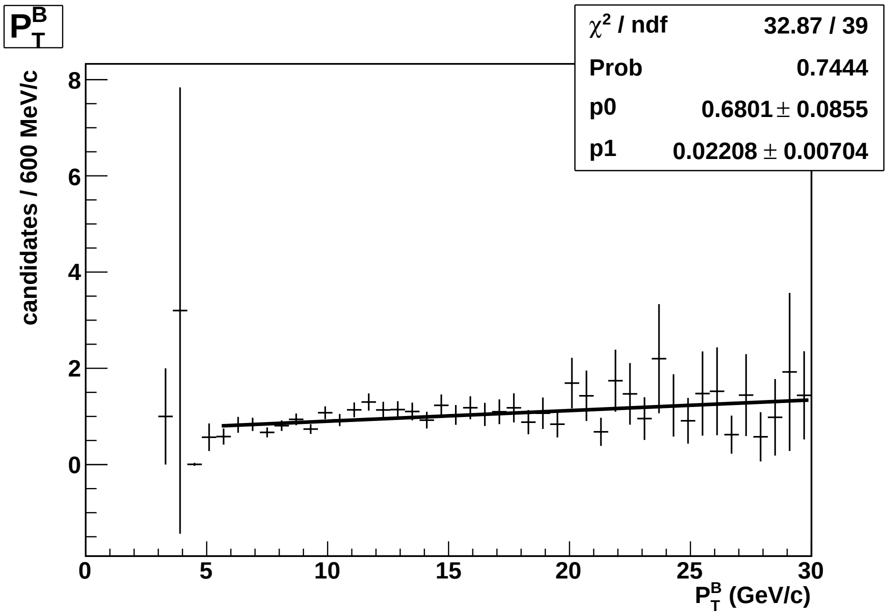

Figure 4: Ratio of B_s^0 p_T in Data and MC for the sideband subtracted $B_s^0 \to J/\psi\phi$ events, reproduced from [3]

used as a reweighting function in the following.

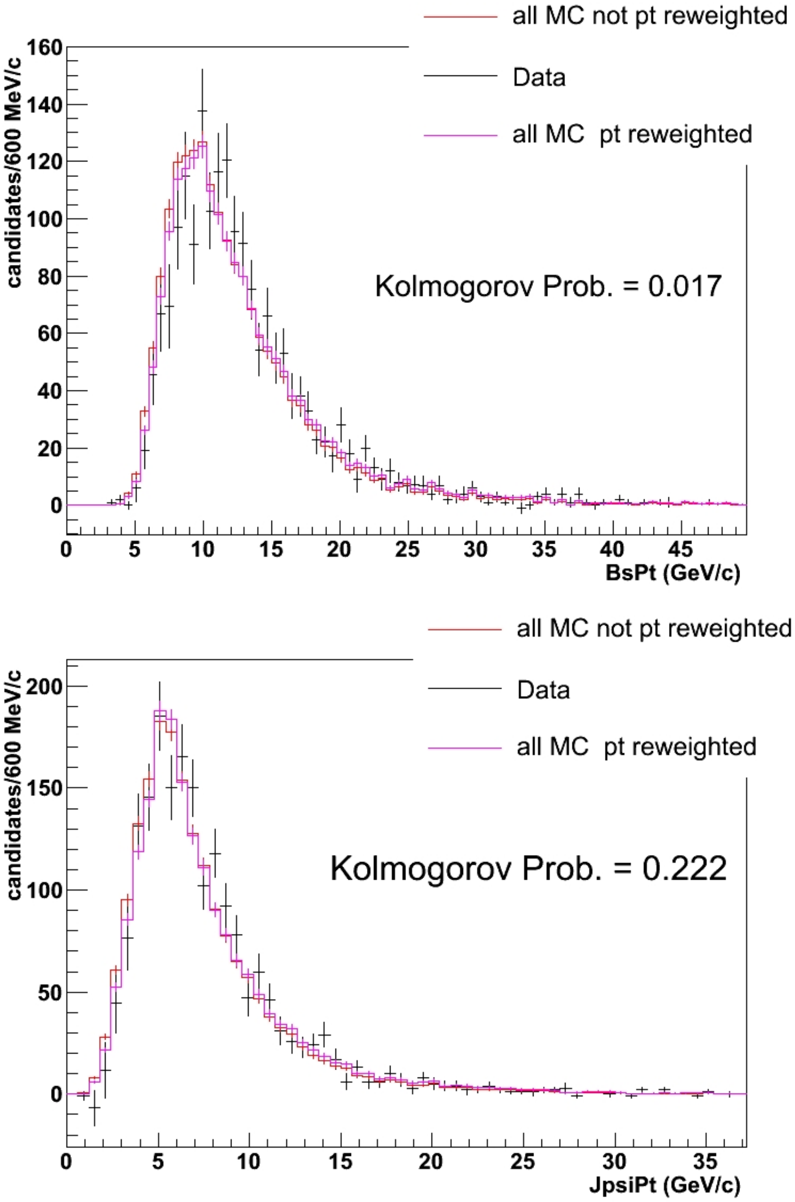

Figure 5: $B_s^0 \rightarrow J/\psi\phi$ comparision of B p_T and J/ψ p_T with and without reweight , reproduced from [3]

We observe in general a better data-MC agreement after the p_T reweight for both $B_s^0 \rightarrow J/\psi\phi$ and $B_s^0 \rightarrow \phi\phi$ candidates for all the p_T related quantities as shown in Figs. 5 and 6.

In the comparison, we adopt the following nomenclature: the *side-band subtraction* is the operation performed on the real data subtracting from the events, in a window around the signal region in the invariant mass histogram of the B_s^0 candidate, $[5.32; 5.42]\,\mathrm{GeV}/c^2$, those events which are located in the sidebands. The two sidebands are: the left one from 5.244 to $5.294\mathrm{GeV}/c^2$ and the right one from 5.444 to $5.494\mathrm{GeV}/c^2$.

Finally for $B_s^0 \rightarrow \phi\phi$ we show the relevant comparisons for the variables used in the signal

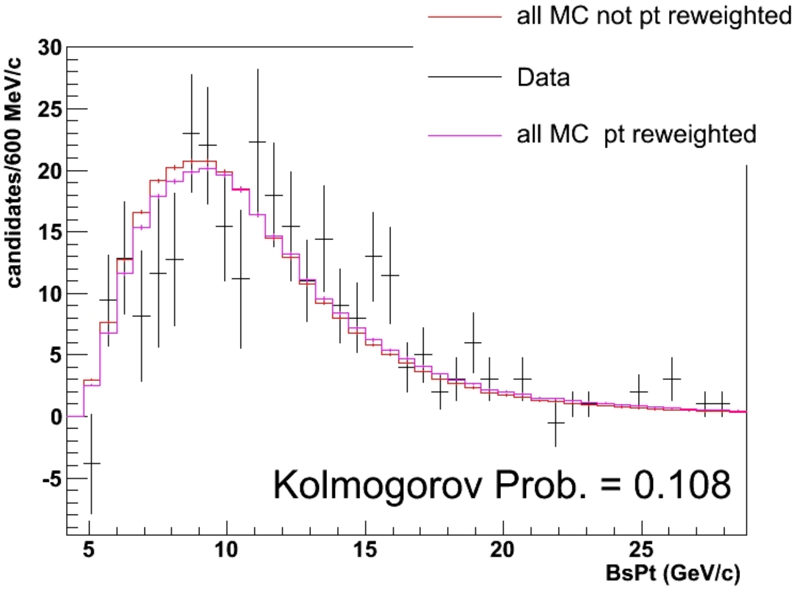

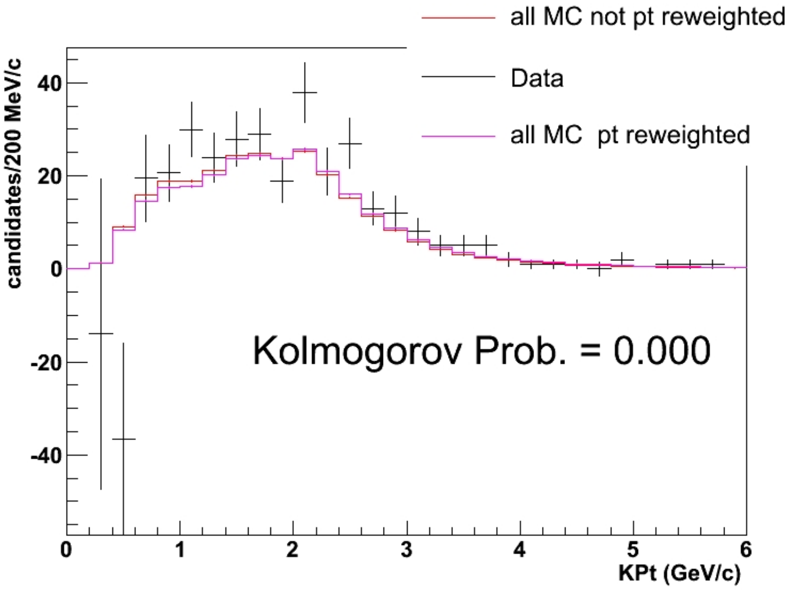

Figure 6: $B_s^0 \to J/\psi\phi$ comparision of B p_T and Kaon momentum with and without reweight, reproduced from [3]

selection in figs. 7, and the p_T distribution for the K^+ and K^- particles in figs. 8 (relevant for the angular acceptance definition).

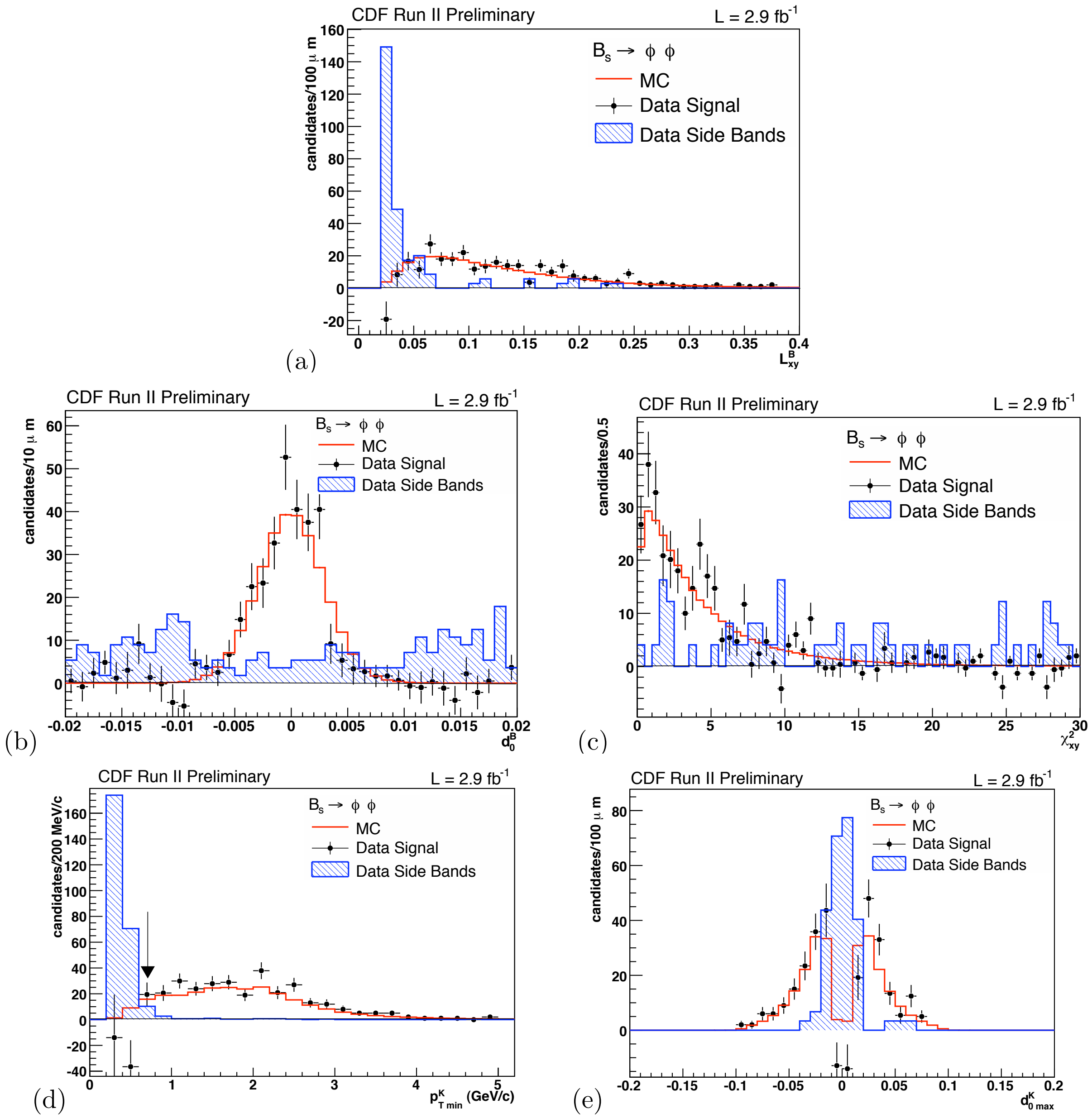

Figure 7: Variables used in the $B^0_s \to \phi\phi$ selection: L^B_{xy} (a), d^B_0 (b), χ^2_{xy} (c), $p^K_{\mathrm{T\ min}}$ (d) and $d^{\phi}_{0\,\mathrm{max}}$ (e). The black points are side-bands subtracted data (see Sect. 6); the red line is the reweighted MC; the blue histogram is the sidebands data distribution.

6.2 Angular Distribution

In the analysis we would like to use the reconstructed B candidates coming from the union of the three exclusive trigger selections, `HIGHPT`, `ScA` and `LOWPT`. Since the different trigger requirements may introduce some large discrepancies from one trigger selection to another, we look for these differences in the variables distributions. In particular, we check the consistencies of the angular

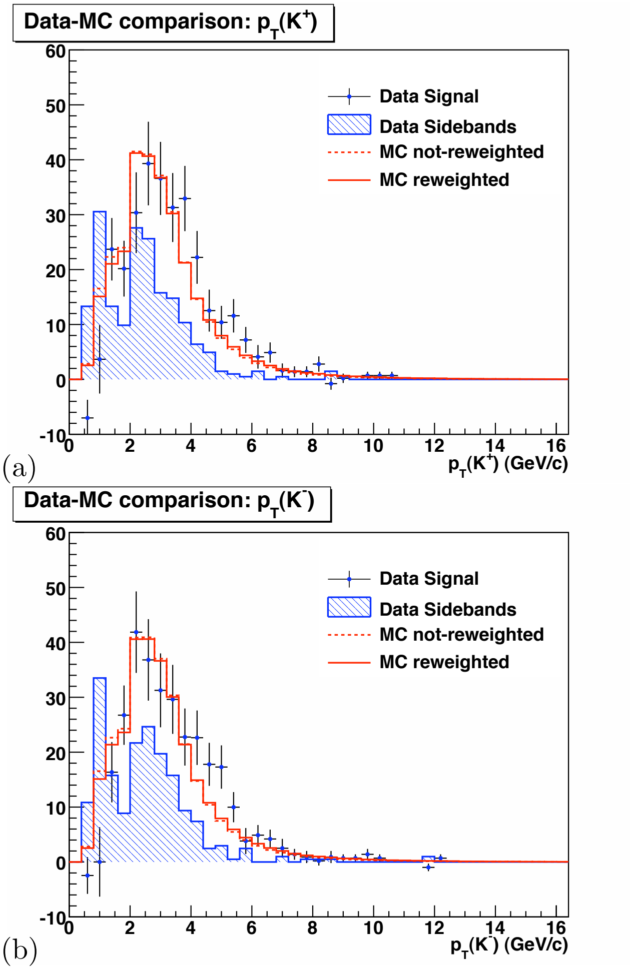

Figure 8: p_{T} distribution for the K^+ (a) and K^- (b) particles for the $B_s^0 \to \phi\phi$. The black points are side-bands subtracted data (see Sect. 6); the red line is the reweighted MC; the red dotted line is the not-reweighted MC; the blue histogram is the sidebands data distribution. The Kolmogorov probability for the comparison of Data and the reweighted MC distributions is 0.08 for (a) and it is 0.15 for (b).

variables, which are the most significant for our analysis. The comparison of the three trigger selections are shown in figs. 9 – 11. For other distributions we point to [3]. A good agreement is seen: the Kolmogorov test performed returns probabilities which are

- about 5% for distributions (a) and (b) in fig 9;
- greater than 30% for distributions (c) and (d) in fig 9;
- greater than 10% for distributions in figs. 10 and 11.

This allow us to easily use all the three exclusive subsamples together in a single fit.

Another check performed is the comparison between the distributions for the high-luminosity runs and the low-luminosity ones. We split the events into two sets:

- events for run numbers > 228596, which correspond to high-luminosity data sample,

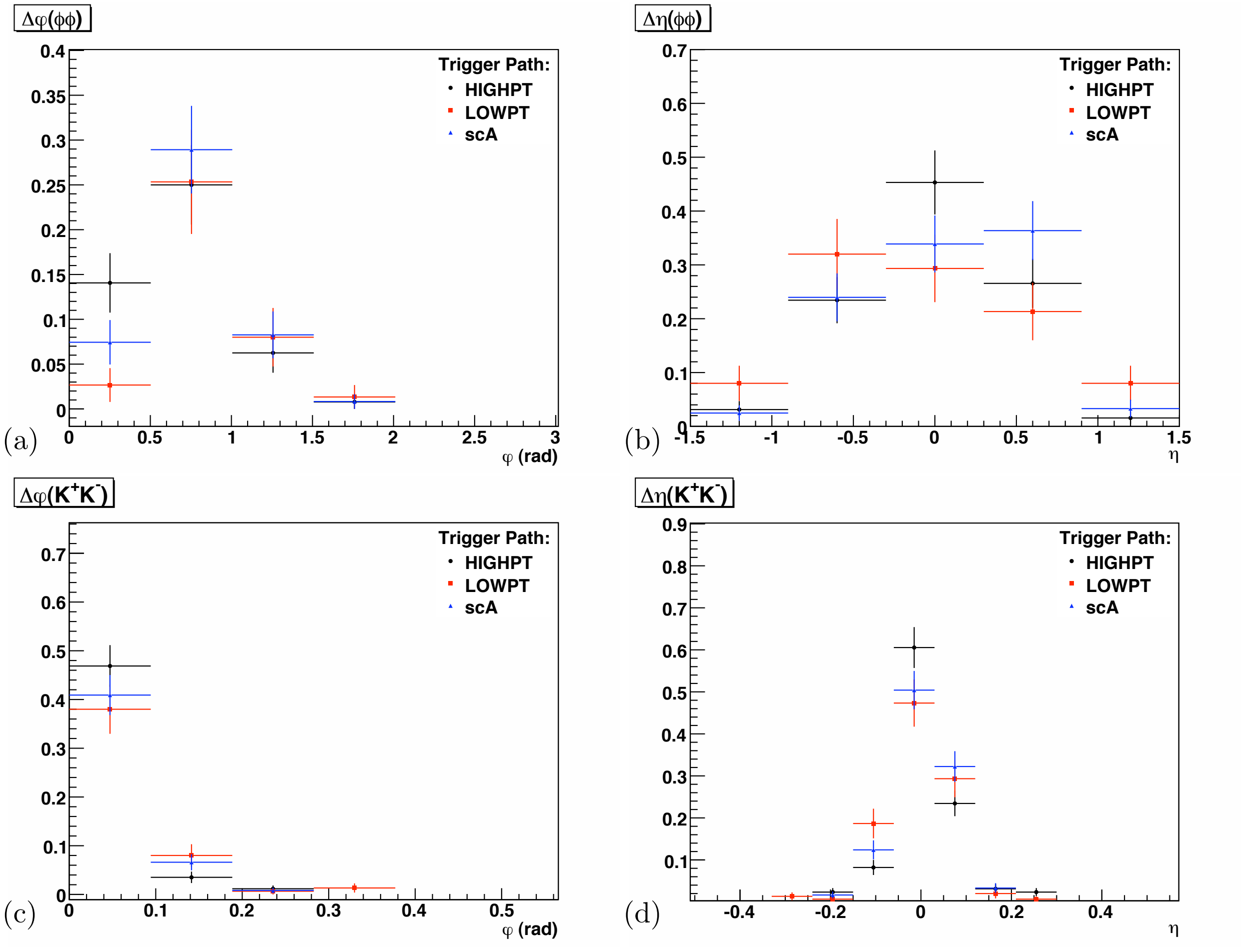

Figure 9: Comparison of trigger paths for the $B_s^0 \to \phi\phi$ decay: $\Delta\varphi$ (a) and $\Delta\eta$ (b) between the ϕ, $\Delta\varphi$ (c) and $\Delta\eta$ (d) between the K^+K^-. The black points are `HIGHPT` the blue points are `LOWPT` and the red ones are `ScA`.

- events for run numbers ≤ 228596, which correspond to low-luminosity data sample,

and we look for discrepancies in the distributions shapes. These comparisons are reported in fig. 12. Again, a good agreement is seen, since the Kolmogorov test performed returns probabilities greater than 85%.

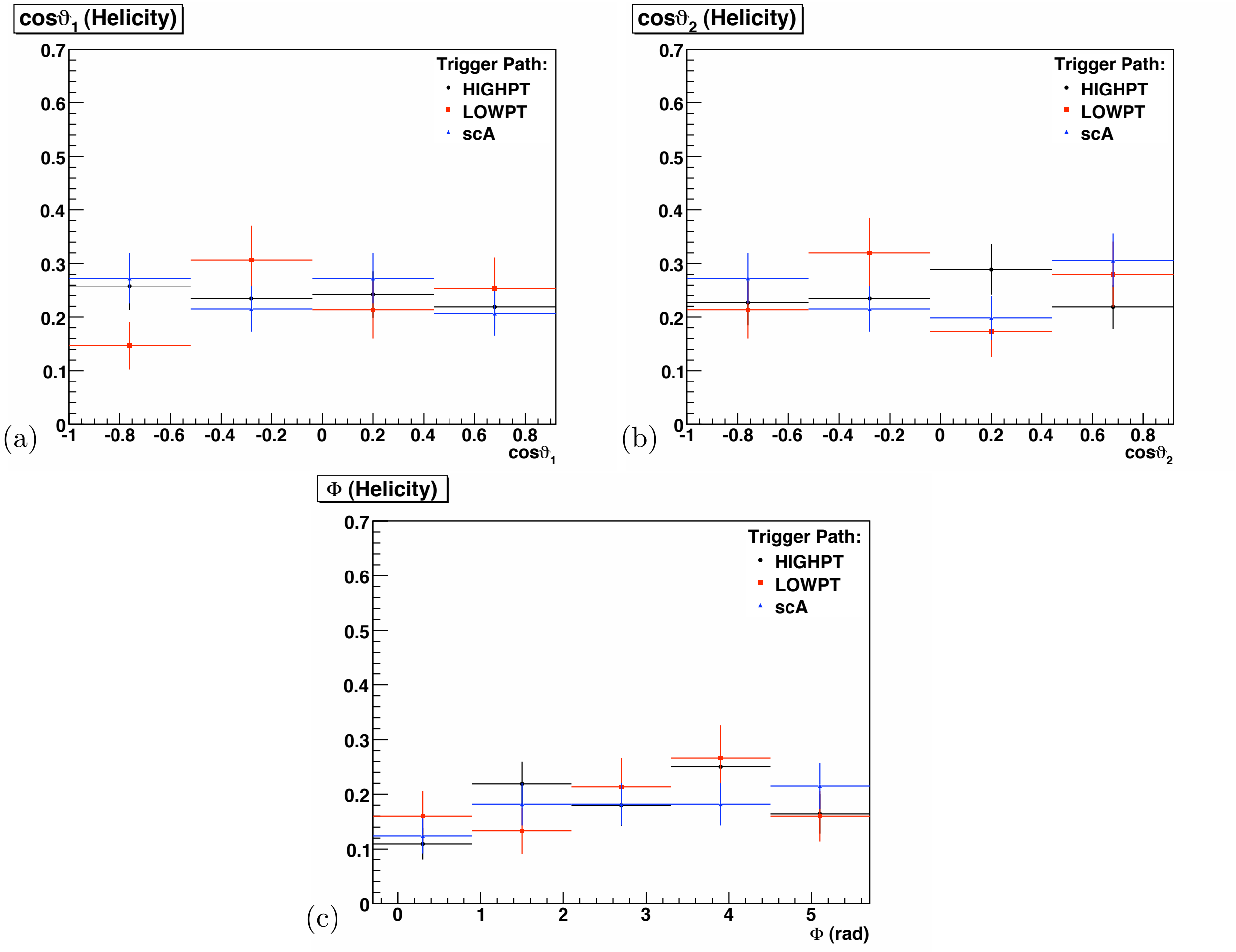

Figure 10: Helicity angles of the $B_s^0 \to \phi\phi$ for the different trigger paths: $\cos\vartheta_1$ (a), $\cos\vartheta_2$ (b) and Φ (c) . The black points are `HIGHPT`, the blue points are `LOWPT` and the red ones are `ScA`.

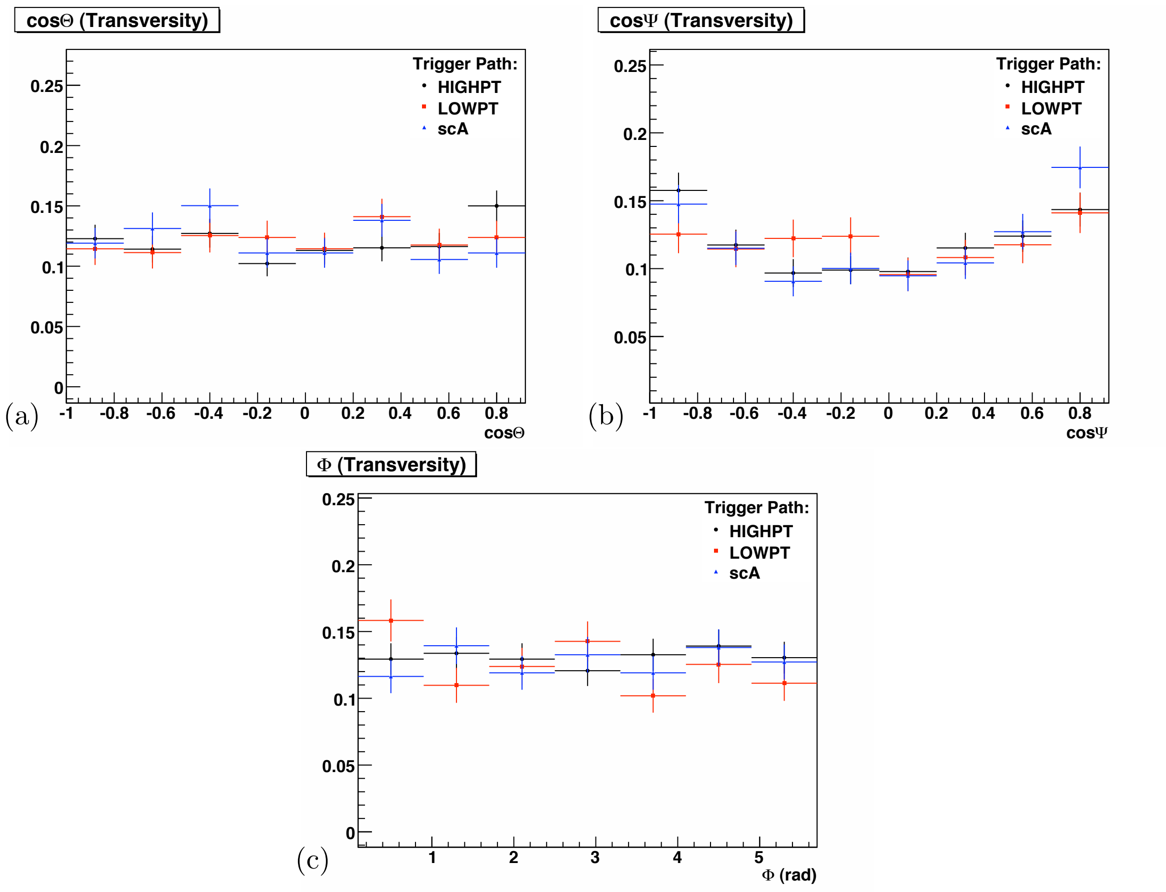

Figure 11: Transversity angles of the $B_s^0 \to J/\psi\phi$ for the different trigger paths: $\cos\Theta$ (a), $\cos\Psi$ (b) and Φ (c) . The black points are `HIGHPT`, the blue points are `LOWPT` and the red ones are `ScA`.

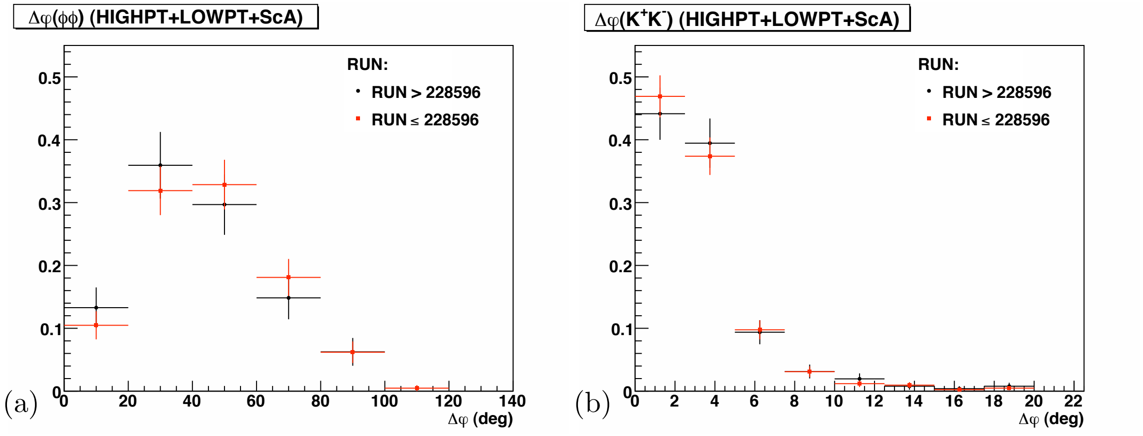

Figure 12: Comparison of high-luminosity and low-luminosity runs for the $B_s^0 \to \phi\phi$ decay: $\Delta\varphi$ between the ϕ (b), $\Delta\varphi$ between the K^+K^- (b). The black points are high-luminosity runs, the red points are low-luminosity ones.

7 Time-Integrated Analysis

In this section we present the measurement of the $B_s^0 \to \phi\phi$ polarization amplitudes using a the time-integrated analysis. A fit to the reconstructed mass and angular variables is developed and tested on simulated- experiments, real data and high statistics realistic MC. In the present Section we present several components of the fitter and the related study on the data.

7.1 Strategy

The aim of the analysis is the estimation of the two polarization amplitudes, $|A_0|^2$ and $|A_\parallel|^2$ and the relative phase between them, $\delta_\parallel$, using as probability density function the angular decay rate distribution of eq. 10 integrated in time. We want to perform an unbinned Maximun Likelihood (ML) fit to the mass and the three helicity angles distributions of the reconstructed B candidates. The mass distribution is used in the fit to discriminate the signal yield with respect to the background. Since in eq. 10 the time and the angular terms do not factorize, the time integration introduces a bias in the estimated parameters. In fact, the time evolution in eq. 10 is represented by two expressions having different live times: $\tau_{\rm L} = 1/\Gamma_{\rm L}$ and $\tau_{\rm H} = 1/\Gamma_{\rm H}$. Our hypothesis is that the statistical uncertainty of our measurement is bigger than the systematic one induced by the time integration. The latter should not be greater than $\Delta\Gamma/\Gamma \sim 10\%$.

In eq. 10 we fix $\Gamma_{\rm L}$ and $\Gamma_{\rm H}$ to the latest PDG values. Moreover, the CP-violation's phase $\phi_{\rm s}$ is set equal to zero, as its value in the SM prediction is very small. In the analysis we don't distinguish between B_s^0 and $\bar{B}_s^0$ at the production time (*untagged* analysis). The detector acceptance in the angular variables defined in Sec. A.1 is assumed unrelated to the B meson proper decay time. This acceptance is determined with the MC program.

The fitter framework will be checked by three tests: the pseudo-experiments pulls distributions, the fit of the $B_s^0 \to J/\psi\phi$ decays as a control sample, and the fit on realistic MC data.

7.2 The Probability Density Function

Suppose we have a set of n measured quantities $\vec{x} = (x_1, \ldots, x_n)$ described by a joint probability density function (pdf) $g(\vec{x}; \vec{\xi})$, where $\vec{\xi} = (\xi_1, \ldots, \xi_k)$ is a set of k parameters whose values are unknown. The likelihood function is given by the pdf evaluated with $\vec{x}$, but expressed as a function of the parameters, *i. e.*, $\mathcal{L}(\vec{\xi}) = g(\vec{x}; \vec{\xi})$. If the measurements x_i are statistically independent and each follow the pdf $g(\vec{x}; \vec{\xi})$, then the joint pdf for $\vec{x}$ factorizes and the likelihood function is

$$\mathcal{L}(\vec{\xi}) = \prod_{i=1}^{n} g(x_i; \vec{\xi}). \tag{13}$$

Then, one needs to known the pdf of the data sample to construct the likelihood function. The pdf functional form is presented for our cases, describing it component by component.

As input variables to the fitter we use the following reconstructed quantities:

- the mass m;
- the angles
  - $\vec{\omega} = (\cos\vartheta_1, \cos\vartheta_2, \varPhi)$, for the $B_s^0 \to \phi\phi$ decay;
  - $\vec{\Omega} = (\cos\Theta, \cos\Psi, \Phi)$, for the $B_s^0 \to J/\psi\phi$ decay;

Here, m is the reconstructed mass of the B_s^0 candidate. For the $B_s^0 \to \phi\phi$ decay, the angles forming the vector $\vec{\omega}$ are defined in the helicity basis; the vector Ω is composed by angles defined in the customary transversity basis for the $B_s^0 \to J/\psi\phi$ decay (see Appendix A). Since our main purpose is the $B_s^0 \to \phi\phi$ angular analysis, in the following all the notations refer to its study. We leave the description of the $B_s^0 \to J/\psi\phi$ analysis in a separate section (Sec. 7.6).

In the $B_s^0 \to \phi\phi$ decay, the identification of the two ϕ as ϕ_1 and ϕ_2 (and then of the two angles ϑ_1 and ϑ_2) is randomly implemented in the code to avoid any bias caused by the internal ordering (*e. g.*, in $p_{\rm T}(\phi)$) of the particles in the `BStntuple`, in order to carry out the symmetry mentioned above. We proceed as follow: for each reconstructed B_s^0 candidate,

- if the event number is even, we use the internal ordering of the `BStntuple`;
- if the event number is odd, the two indexes, 1 and 2, of the `BStntuple` order are exchanged among each other.

This simple algorithm assures the symmetry of the variables under indexes exchange 1 ↔ 2.

The observables m and $\vec{\omega}$ give rise to the vector

$$\vec{x}_i = (m_i, \vec{\omega}_i) \tag{14}$$

where i spans over the number of events in the data sample, and the measurements vector is $\vec{x} = (\vec{x}_1, \ldots, \vec{x}_N)$. The pdf is the sum of two components: $g_{\rm s}$, representing the signal set, and $g_{\rm b}$, for the background events, *i. e.*,

$$g(\vec{x}_i, \vec{\xi}) = (1 - f_{\rm b}) g_{\rm s}(\vec{x}_i, \vec{\xi}_{\rm s}) + f_{\rm b} g_{\rm b}(\vec{x}_i, \vec{\xi}_{\rm b}), \tag{15}$$

where $f_{\rm b}$ is the fraction of background events ($0 \leq f_{\rm b} \leq 1$). Since the mass and the angular variables are statistically independent, the pdf can be factorized in two corresponding terms:

$$g_{\rm s}(\vec{x}_i, \vec{\xi}_{\rm s}) = g_{\rm s}^{(m)}(m_i, \vec{\xi}_{\rm s}^{m}) g_{\rm s}^{(\omega)}(\vec{\omega}_i, \vec{\xi}_{\rm s}^{\omega}), \tag{16a}$$

$$g_{\rm b}(\vec{x}_i, \vec{\xi}_{\rm b}) = g_{\rm b}^{(m)}(m_i, \vec{\xi}_{\rm b}^{m}) g_{\rm b}^{(\omega)}(\vec{\omega}_i, \vec{\xi}_{\rm b}^{\omega}) \tag{16b}$$

$$\tag{16c}$$

The pdf must be normalized to one, thus the following relations hold:

$$\int g_{\rm s/b}^{(m)}\, dm = 1, \tag{17a}$$

$$\int g_{\rm s/b}^{(\omega)}\, d\vec{\omega} = 1. \tag{17b}$$

We evaluate the best parametrization of the pdf components, using also the MC simulation. They are presented in the following sections. This procedure allowed us to fix some parameters in the function parametrization and then to make a global fit with a limited number of free parameters.

We don't consider the reflection components in the background parametrization: since they are a tiny percentage of the total data sample, they can be neglected at first order (see Sec. 9). Thus, if it is not properly pointed out, when we refer to the background, we mean only the dominant combinatorial component.

7.3 Mass Model

The signal distribution has a width of around 20 MeV for the $B_s^0 \to \phi\phi$ (see fig. 2 in the previous section). It is parametrized with two gaussian functions having the same mean value M but different resolutions, σ and $k\sigma$. This choice is fairly standard and takes into account the detector effects that cause an additional spread in the tail distributions. The function used to parametrize the distributions is the following:

$$g_{\mathrm{s}}^{(m)} = h\frac{1}{\sqrt{2\pi}\sigma}e^{-\frac{(m-M)^2}{2\sigma^2}} + (1-h)\frac{1}{\sqrt{2\pi}k\sigma}e^{-\frac{(m-M)^2}{2k^2\sigma^2}} \tag{18}$$

where h is the fraction of one gaussian component with respect to the other. Fitting the MC events of fig. 13, we obtained the parameters summarized in tab. 4. In the final fit the multiplicative factor k and the fraction h are fixed, while the other parameters are left free.

Parameter	MC fit value
M [GeV/c^2]	5.36995 ± 0.00004
σ [GeV/c^2]	0.01577 ± 0.00004
k	2.87 ± 0.03
h	0.932 ± 0.002

Table 4: Parameters of MC data mass fit for $B_s^0 \to \phi\phi$. All symbols are defined in the text.

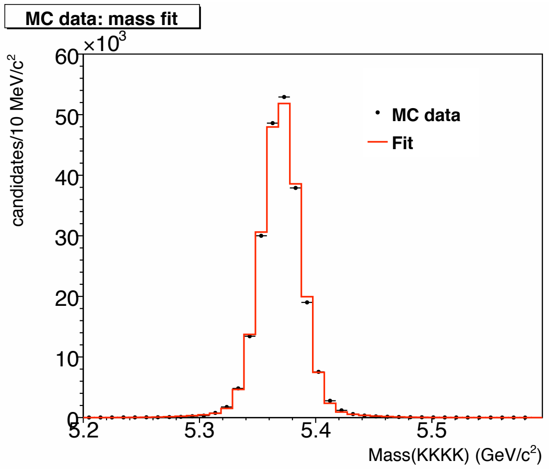

Figure 13: Mass fit of MC data for $B_s^0 \to \phi\phi$. The black points are the MC data; the red line is the resulting fit distribution.

The mass background follows, with a good approximation, an exponentially decreasing behavior:

$$g_{\mathrm{b}}^{(m)} = \frac{b}{e^{-bm_{\min}} - e^{-bm_{\max}}}e^{-bm} \tag{19}$$

where b is the slope of the exponential function, and m spans the interval $[m_{\min} = 5.2, m_{\max} = 5.6]$ GeV/c^2. In this case, we didn't perform a MC study and a simple parametrization has been used instead.

7.3.1 Comparison with Binned Likelihood Fit of the BR Analysis

We can compare the results of this unbinned ML fit of the reconstructed B mass with respect to the binned fit performed in the branching ratio analysis [3]. This allows us to check the tiny effects of the reflections in the background component, since the binned fit takes them into account and since the data sample is the same for the two fits. Table 5 reports the two fit's results and the mass distributions are shown in fig. 14. We obtain a very good agreement in the central values and in their uncertainties.

Parameter	Unbinned fit	Binned fit
M [GeV/c^2]	5.364 ± 0.001	5.364 ± 0.001
σ [GeV/c^2]	0.016 ± 0.001	0.017 ± 0.001
f_{b}	0.38 ± 0.03	0.39 ± 0.03
b	2.7 ± 0.7	2.5 ± 0.7

Table 5: Comparison of the mass fit results with the branching ratio analysis' ones [3].

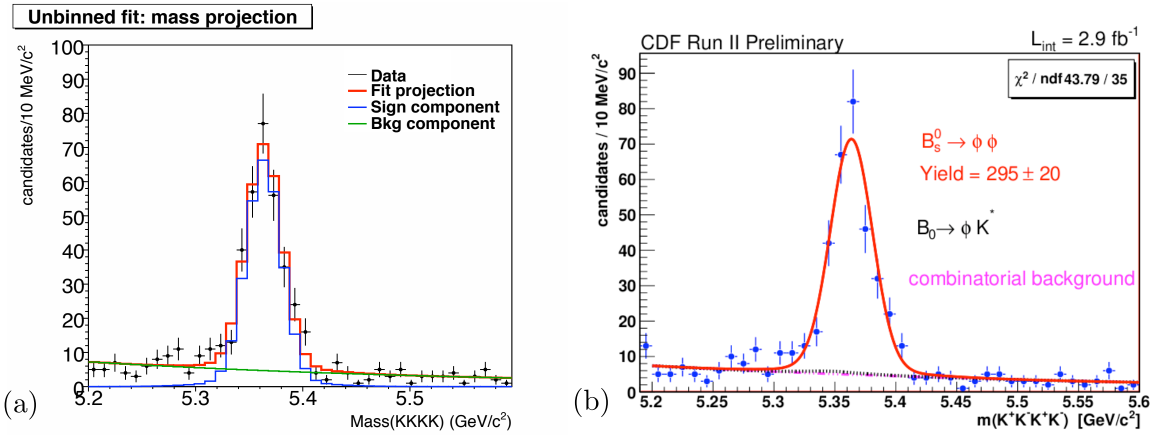

Figure 14: Comparison of our fit mass projection with the fit of the branching ratio analysis. (a) mass projection of the unbinned fit; (b) binned fit in [3].

7.4 Angular Model

The pdf used to describe the helicity angular distribution for the signal is obtained integrating in time the theoretical differential decay rate reported in eq. 10 of sec. 3.1. It is important to stress that this formula has been obtained summing over the initially produced B_s^0 and $\bar{B}_s^0$, without attempting to tag the production flavor identification at the production time, and, assuming no CP violation, fixing $\phi_{\mathrm{s}} = 0$ as in the SM. Thus, the resulting signal angular pdf is:

$$g_{\mathrm{s}}^{(\omega)} = \frac{d^3\Lambda(\vec{\omega})}{d\vec{\omega}} = \frac{9}{32\pi}\frac{1}{\tilde{W}}\left[\tilde{\mathcal{F}}_{\mathrm{e}}(\vec{\omega}) + \tilde{\mathcal{F}}_{\mathrm{o}}(\vec{\omega})\right] \tag{20}$$

where

$$\tilde{\mathcal{F}}_{\mathrm{e}} = \frac{2}{\Gamma_{\mathrm{L}}}\left[|A_0|^2 f_1(\vec{\omega}) + |A_{\parallel}|^2 f_2(\vec{\omega}) + |A_0||A_{\parallel}|\cos\delta_{\parallel} f_5(\vec{\omega})\right] \tag{21a}$$

$$\tilde{\mathcal{F}}_{\mathrm{o}} = \frac{2}{\Gamma_{\mathrm{H}}}|A_{\perp}|^2 f_3(\vec{\omega}) \tag{21b}$$

$$\tilde{W} = \frac{|A_0|^2 + |A_{\parallel}|^2}{\Gamma_{\mathrm{L}}} + \frac{|A_{\perp}|^2}{\Gamma_{\mathrm{H}}} \tag{21c}$$

Since we want to measure only the polarization amplitudes, we fix Γ_{L} and Γ_{H} to the latest PDG values (see eq. (6a)) in the final fit.

7.4.1 Detector Angular Acceptance

We expect not to have a uniform acceptance in the helicity (transversity) angles. The trigger paths and the off-line selection could modify the angular distribution as well. Another source of inefficiency is due to the p_{T} acceptance: the helicity variables are strictly related to the K p_{T} since, in practice, the computation of the angles is based on the reconstructed momenta. Thus, a part of the angular inefficiency comes from the events which have in the final state K with low p_{T} that are lost in the on-line selection. So it is crucial for the analysis to be able to unfold all these effects, we refer to as "angular acceptance".

In order to study the detector impact on the angular distributions, we generate a "phase space MC" data sample (in the following we refer to it as "PHSP" MC). Phase space MC means that the MC simulates the decays considering only the phase space variables of the particles. The PHSP model generates final state particles with a spin density matrix that is diagonal. For a vector this means 1/3 probability for each of the 3 polarization states. There are no correlations between the two vector decays in the $B_s^0 \to \phi\phi$ decay when the PHSP model is used. This means that the angular distributions are generated uniform.

The simulated events are passed through the full-fledged detector simulation. Then, they are selected with the same on-line and off-line requirements of the real data. Thus, we can obtain a three-dimensional acceptance curve $\mathcal{A}(\vec{\omega})$, which accounts for the detector acceptance in the angular variables. In practice, we construct $\mathcal{A}(\vec{\omega})$ as a three-dimensional histogram $H(\vec{\omega})$, and the acceptance is calculated as the ratio of accepted and generated events in each three-dimensional bin in ω divided by the total number of generated events such that the sum of the weights in all the bins in the histogram is 1. The three-dimensional histogram is made of 440000 events, which fill $20 \times 20 \times 20$ bins. Thus, the acceptance function can be interpreted as the probability to find an event at each position in the $\vec{\omega}$ space. The projections of $H(\vec{\omega})$ onto the three axes of the helicity angles basis are shown in fig. 15. We note that the detector and the other selections don't change the Φ distribution, that is still flat.

The angular acceptance effect is finally taken into account by the multiplicative term $\mathcal{H}(\vec{\omega})$ in the signal angular pdf:

$$g_{\mathrm{s}}^{(\omega)} = \frac{d^3\Lambda(\vec{\omega})}{d\vec{\omega}} \to g_{\mathrm{s}}^{(\omega)} = \frac{1}{\mathcal{N}}\frac{d^3\Lambda(\vec{\omega})}{d\vec{\omega}}\mathcal{H}(\vec{\omega}) \tag{22}$$

where $\mathcal{N}$ is a normalization term. The presence of $\mathcal{H}(\vec{\omega})$ bring some complication in the normalization process: both the angular distribution and the acceptance distribution are independently normalized, however, it is not assured that their product will be normalized as well. The normalization procedure for the calculation of $\mathcal{N}$ is described in Appendix B.

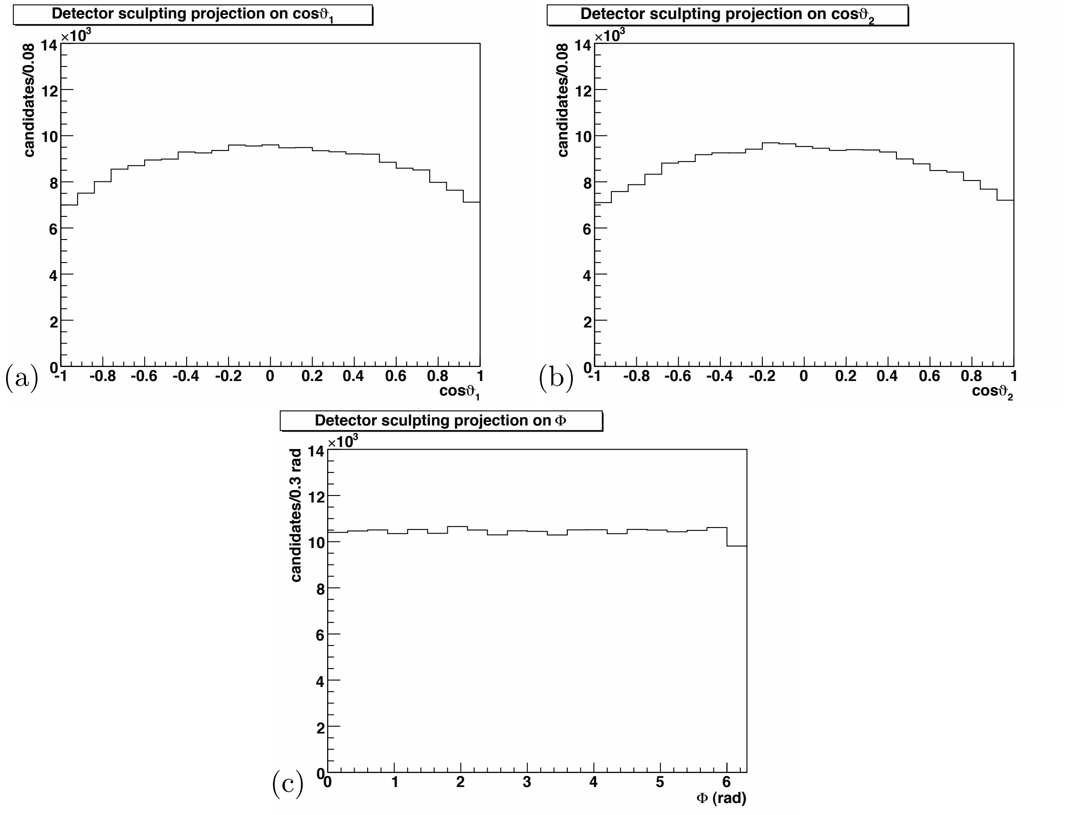

Figure 15: Detector angular acceptance projections: $\cos\vartheta_1$ (a), $\cos\vartheta_2$ (b) and Φ (c).

7.4.2 Effect of Different Trigger Path on the Detector Angular Acceptance

There is the possibility that the acceptance curve is different for the three trigger path selections. If this happens, more complications arise in the analysis of all exclusive trigger sets together. To check if this is the case, we look at the projections of $H(\vec{\omega})$ for the different trigger paths. They are shown in fig. 16: we can conclude that $H(\vec{\omega})$ is quite similar for each trigger selection. This test also guarantees no dependencies on the integrated luminosity collected with the three different trigger paths. These allows us to use in a straightforward way all the exclusive data set together, minimizing the statistical errors on ours measurements. Anyway, in the systematic treatment, we estimate the impact on our fit estimates of this assumption.

7.4.3 Dependence of the Angular Acceptance on the B Proper Decay Time

We assume that $\mathcal{A}(\vec{\omega})$ is not dependent on the reconstructed B_s^0 proper decay time t. Thus, we check if this hypothesis is correct, by dividing the MC data sample in three sets (see fig. 17):

- set_1: events which have $ct \in [0.00; 0.05]$ cm;
- set_2: events which have $ct \in]0.05; 0.10]$ cm;
- set_3: events which have $ct \in]0.10; 0.50]$ cm.

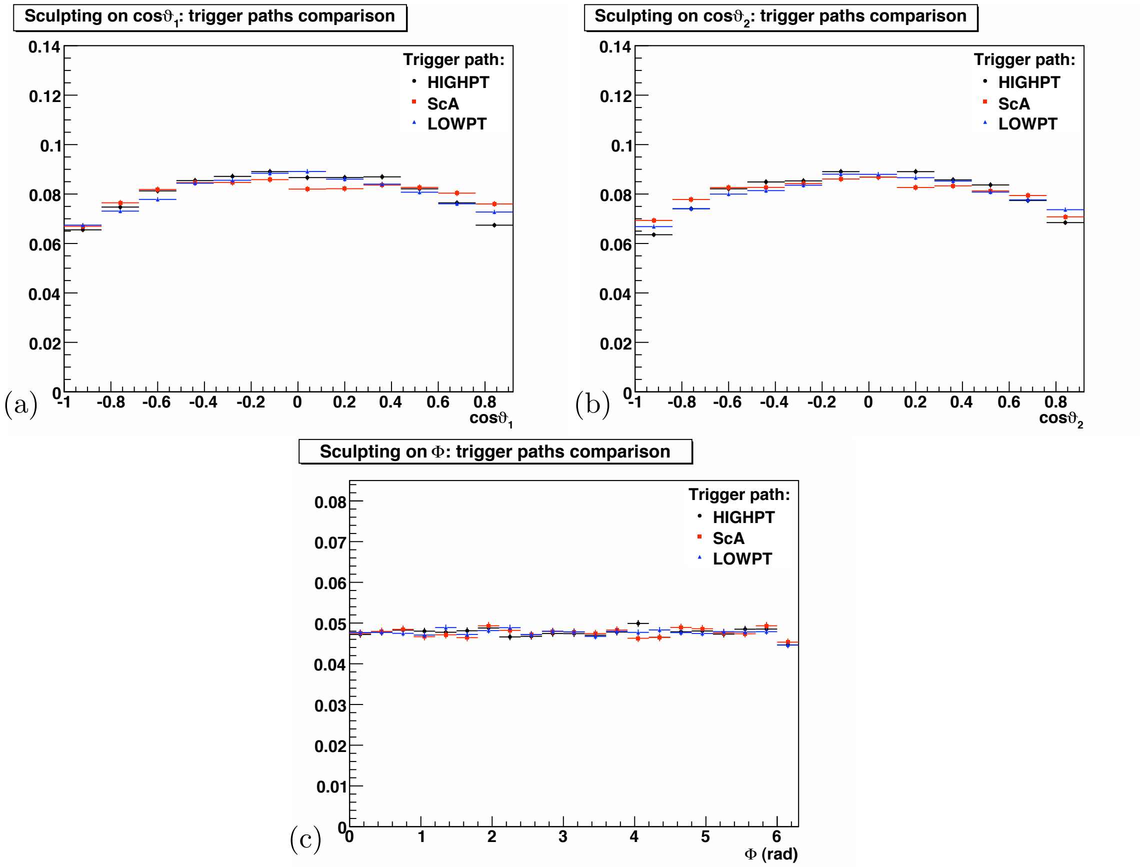

Figure 16: Effect of different trigger path on angular detector angular acceptance: $\cos\vartheta_1$ (a), $\cos\vartheta_2$ (b) and Φ (c).

For each set the three-dimensional histogram representing the angular acceptance, $H_i(\vec{\omega})$ ($i = 1, 2, 3$), is built, and then its projections on the three helicity angles are produced. We call this the operation of "binning the angular acceptance in slices of *ct*". Thus, we compare the three different

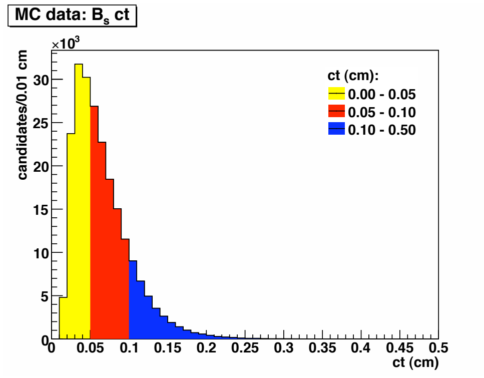

Figure 17: *ct* distribution of PHSP MC data sample. The three *ct* slices are represented with different colors: in yellow 0.00 cm $< ct <$ 0.05 cm, in red 0.05 cm $\leq ct <$ 0.10 cm and in blue 0.10 cm $< ct <$ 0.50 cm.

slices in ct for each $H_i(\vec{\omega})$ projection. They are shown in fig. 18. From these plots the effect of the angular acceptance dependence on ct is evident in the $\cos\vartheta_1$ and $\cos\vartheta_2$ variables; the Φ projection, instead, is quite the same for each bin of ct. We perform a Kolmogorov test (tab. 6) on these projections, that confirms the changes of the $\cos\vartheta_{1(2)}$ projections with ct. However, in the fit we will use the $H_i(\vec{\omega})$ histogram assuming that there is no ct-dependence and leave the evaluation of possible impacts of this assumption on the fit estimates in the systematics treatment.

Variable		Kolmogorov Probability
$\cos\vartheta_1$	set_1 Vs set_2	2×10^{-4}
	set_2 Vs set_3	9×10^{-4}
	set_1 Vs set_3	1×10^{-9}
$\cos\vartheta_2$	set_1 Vs set_2	5×10^{-5}
	set_2 Vs set_3	5×10^{-5}
	set_1 Vs set_3	1×10^{-12}
Φ	set_1 Vs set_2	0.36
	set_2 Vs set_3	0.57
	set_1 Vs set_3	0.65

Table 6: Comparison between three different slices of ct of the angular acceptance.

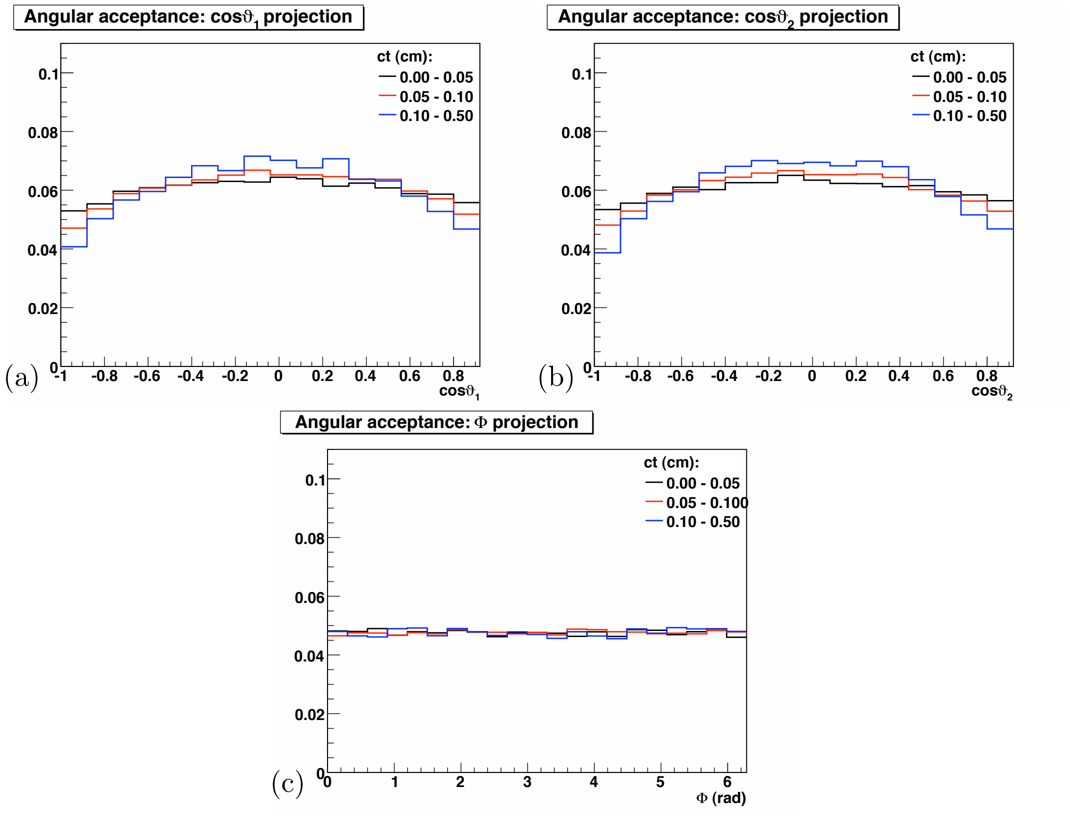

Figure 18: Dependence of detector angular acceptance projections on ct: $\cos\vartheta_1$ (a), $\cos\vartheta_2$ (b) and Φ (c).

7.4.4 Comparison with Previous Works

In some of the previous CDF angular analysis, another method has been adopted to treat the detector angular acceptance. Like the one presented above, it makes use of the flat MC, but in a different way.

In principle, the angular acceptance besides the angular variables is a function of kinematic variables as well as the detailed trigger criteria: we have $\mathcal{A}(\vec{\omega}, \vec{k})$, where $\vec{k}$ is the vector of the kinematic variables. Thus, remembering the form of the differential decay rate of eq. (2), the signal pdf is

$$\frac{1}{\mathcal{N}}\frac{d^3\Lambda(\vec{\omega})}{d\vec{\omega}}V(\vec{k})\mathcal{A}(\vec{\omega}, \vec{k}) = \frac{V(\vec{k})\mathcal{A}(\vec{\omega}, \vec{k})}{\mathcal{N}}\sum_{i=1}^{6} K_i f_i(\vec{\omega}) \tag{23}$$

where $V(\vec{k})$ is the distribution of the candidates in the $\vec{k}$ space. $\mathcal{N}$ is the normalization factor:

$$\begin{aligned}\mathcal{N} &= \int\int d\vec{\omega} d\vec{k} \frac{d^3\Lambda(\vec{\omega})}{d\vec{\omega}}V(\vec{k})\mathcal{A}(\vec{\omega}, \vec{k}) = \\ &= \sum_{i=1}^{6} K_i \left[\int\int d\vec{\omega} d\vec{k} f_i(\vec{\omega})V(\vec{k})\mathcal{A}(\vec{\omega}, \vec{k})\right] \\ &= \sum_{i=1}^{6} K_i \zeta_i\end{aligned} \tag{24}$$

In the last line of eq. (24), the coefficients ζ_i are the result of the double integral in the second line: they can be computed once using the flat MC. In fact, in the limit of infinite number of reconstructed candidates, $N \to \infty$, the following relation holds:

$$\zeta_i = \frac{1}{N}\sum_{j}^{N} f_i(\omega_j), \text{ with } \omega_j \in \{\text{flat MC}\} \tag{25}$$

Then, the method of ML requires the maximization of the $\log\mathcal{L}$:[5]

$$\begin{aligned}\log\mathcal{L} &= \sum_{j}^{N}\log\left[\frac{V(\vec{k_j})\mathcal{A}(\vec{\omega_j}, \vec{k_j})}{\mathcal{N}}\sum_{i=1}^{6} K_i f_i(\vec{\omega_j})\right] \\ &= \sum_{j}^{N}\log\left[\sum_{i=1}^{6} K_i f_i(\vec{\omega_j})\right] - N\log\left[\sum_{i=1}^{6} K_i\zeta_i\right] + \sum_{j}^{N}\log\left[V(\vec{k_j})\mathcal{A}(\vec{\omega_j})\right]\end{aligned} \tag{26}$$

Since the last term of the second line of eq. (26) doesn't depend on the fit parameters, it can be removed from the likelihood function: it is a constant in the maximization procedure. Thus, the final fit doesn't depend on the knowledge of the analytic form of the detector angular acceptance: the entire information of its effect is contained in the ζ_i coefficients.

This method seems more convenient than ours, but, paying attention of some assumptions in this approach, we will realize that they are not so different. This method is based on the eq. (25). This formula is an approximation, because:

---

[5] For simplicity, here is considered only the angular part.

1. the identity is valid only in the limit of $N \to \infty$;
2. the equation represents a good description as well as the MC data can reproduce the real data.

The same considerations can be done for our method. First, the histogram takes automatically into account the $V(\vec{k})$ distribution. Second, if we model the acceptance curves $\mathcal{A}(\vec{\omega}, \vec{k})$ with a three-dimensional histogram $H(\vec{\omega}, \vec{k})$, coming from the flat MC, this is subjected to the same two issues presented above:

1. the histogram reproduces a continuum function only in the limit of an infinitesimal bin's volume, *i. e.*, an infinite number of bins, which requires an infinite number of events;
2. since the histogram comes from the MC simulation, its quality depends on the MC's ability to reproduce the real data.

Finally, we don't find any reasons to prefer one of the two methods. Our choice comes only from a pragmatic motivation: the framework used to perform the analysis is a modification of an older one involving the histogram's method.

A further comparison with the previous works is to look at the angular acceptance projections. This is the first time that the $B_s^0 \to \phi\phi$ decay is studied and its descriptions make use of the helicity angles. However, the other decays analyzed at CDFII are all described in the transversity basis: they are $B_s^0 \to J\psi\phi$ and $B_d^0 \to J/\psi K^{0\star}$ in [1, 53], $B_d^0 \to J/\psi K^{0\star}$ and $B_d^0 \to \phi K^{0\star}$ in [4] . Anyway, ϑ_{1-2} (of helicity basis) and Ψ (of the transversity basis) are the same angles (see the definitions in Appendix A). Thus, it is correct to compare the $\cos\vartheta_{1-2}$ angular acceptance distribution with the one of $\cos\Psi$. Looking at the analysis listed above, we find that:

- the distributions' shape is the same of fig. 15;
- the difference between the maximum of the distribution at $\cos\Psi = 0$ and the minimum at $\cos\Psi = \pm 1$ is about 20% and it is of the same order of what we find in our distribution.

If one wants to look at the other angles, the control samples used here ($B_s^0 \to J\psi\phi$), which is described with the transversity angles, must be considered. We only mention here that no discrepancies are found with respect to the analysis in [1, 53, 4], as can be seen from the plots in fig. 54 of the Appendix D, which represent the transversity angular acceptance projections for the $B_s^0 \to J\psi\phi$ decay.

The agreement with the angular acceptance projections of the previous work confirms that the main consequence of the angular acceptance on the angular distributions comes from the detector geometry; it is independent of certain trigger details.

7.4.5 Background Parametrization

It is reasonable to suppose that the helicity angles do not have any intrinsic meaning for the combinatorial background. To verify this hypothesis in fig. 19 we compare the side-bands angular distributions and those of the flat MC data. Thus, we use a purely empirical model derived by analysing the angular distributions in the mass sidebands to model the background. In order to increase the statistic of the side-bands region, we enlarge the side-bands width ranges with respect to the ones defined in Sect 6, choosing the two intervals $[5.02; 5.22]$ GeV/c^2 and $[5.52; 5.72]$ GeV/c^2 ;

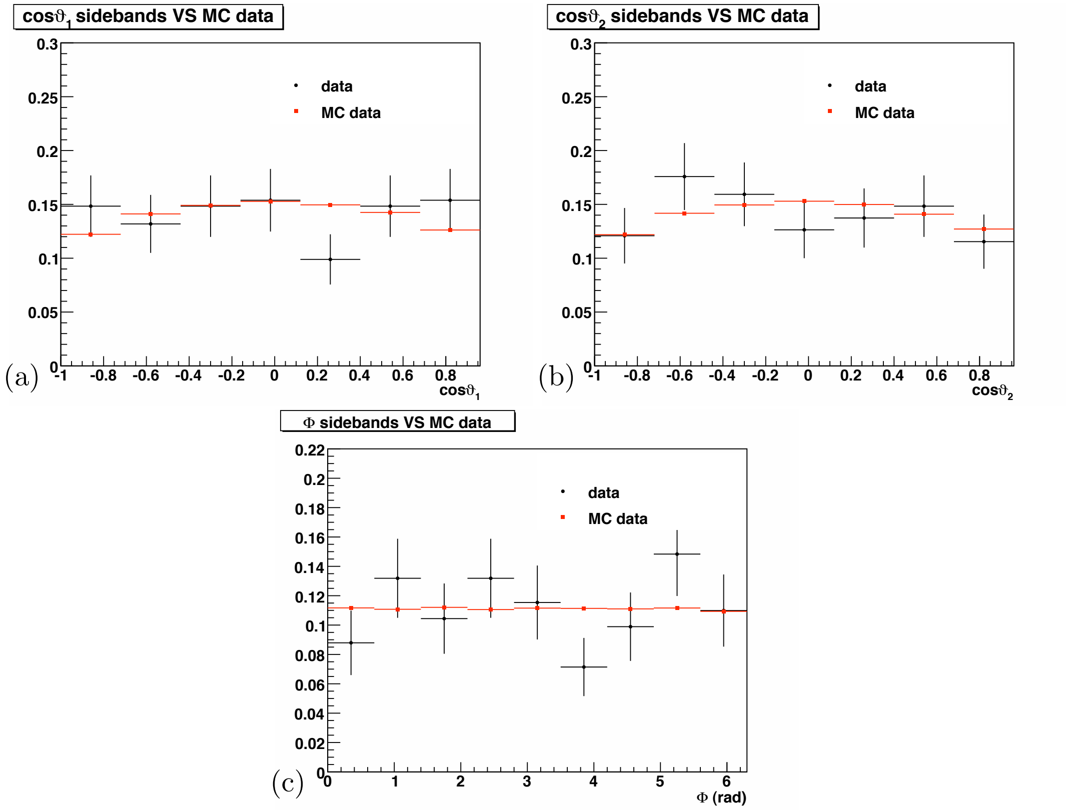

Figure 19: Comparison between side-bands and MC data angular distributions: $\cos\vartheta_1$ (a), $\cos\vartheta_2$ (b) and Φ (c). Black points are side-bands data; red points are MC data. All plots present a Kolmogorov test probability greater than 88%.

then we also remove the $L_{xy} > 330\ \mu$m cut selection, which doesn't have any appreciable effects on the angular variables distributions, as one can see in fig. 20.

Looking at the scatter plots in fig. 21, we see that the angular variables are not correlated in the sideband regions; then the angular background pdf factorizes in the product of three terms:

$$g_{\mathrm{b}} = g_{\mathrm{b}}^{(\omega_1)} g_{\mathrm{b}}^{(\omega_2)} g_{\mathrm{b}}^{(\omega_3)} \tag{27}$$

In order to minimize the number of floating parameters in the fit, we use the symmetry between the $\cos\vartheta_1$ and $\cos\vartheta_2$ variables and we adopt the same functional form with a single free parameter, B, for both these variables. Moreover, it seems reasonable to use a uniform distribution to model the Φ background distribution (see fig.19c). Thus for the $B_s^0 \to \phi\phi$ decay the adopted parametrizations are:

$$g_{\mathrm{b}}^{(\omega_1)} = \frac{1}{2(1+\frac{B}{3})}\left(1 + B\cos^2\vartheta_1\right), \tag{28a}$$

$$g_{\mathrm{b}}^{(\omega_2)} = \frac{1}{2(1+\frac{B}{3})}\left(1 + B\cos^2\vartheta_2\right), \tag{28b}$$

$$g_{\mathrm{b}}^{(\omega_3)} = \frac{1}{2\pi}. \tag{28c}$$

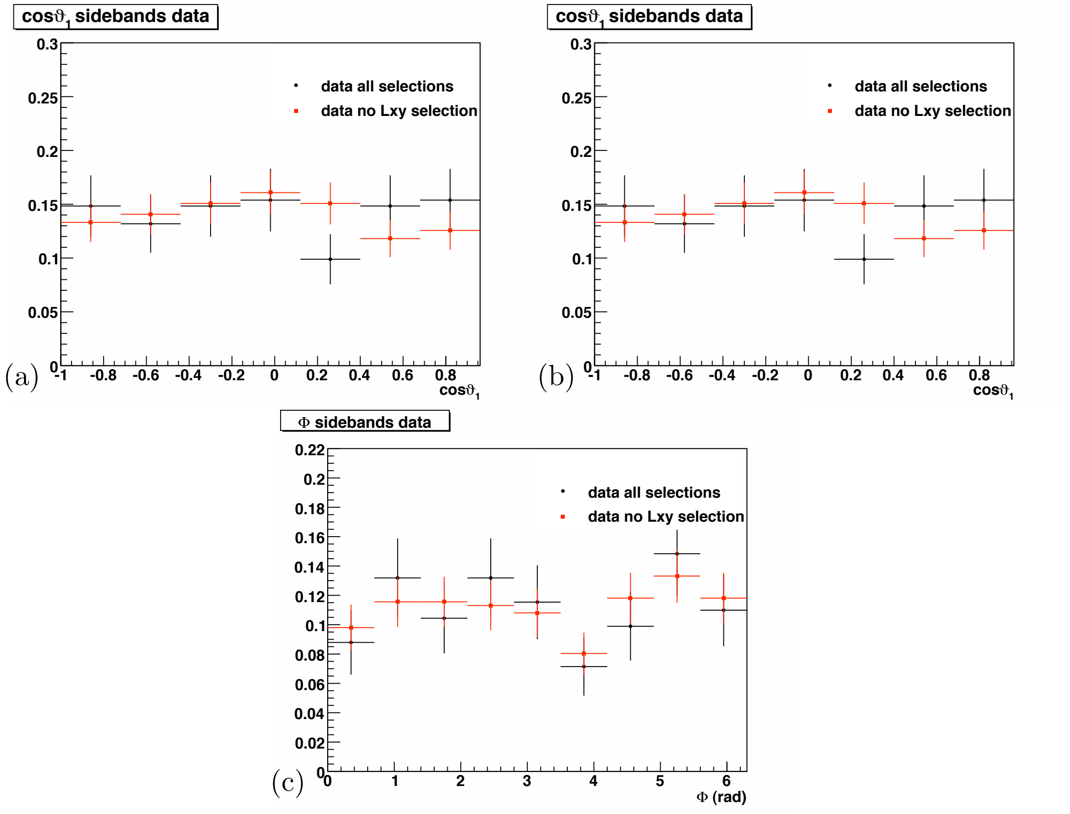

Figure 20: Comparison between side-bands data angular distributions with and without the L_{xy} selection: $\cos\vartheta_1$ (a), $\cos\vartheta_2$ (b) and Φ (c). Black points are side-bands data with all selections (see Sect. 5); red points are side-bands data removing the $L_{xy} > 330$ μm selection. All plots present a Kolmogorov test probability greater than 80%.

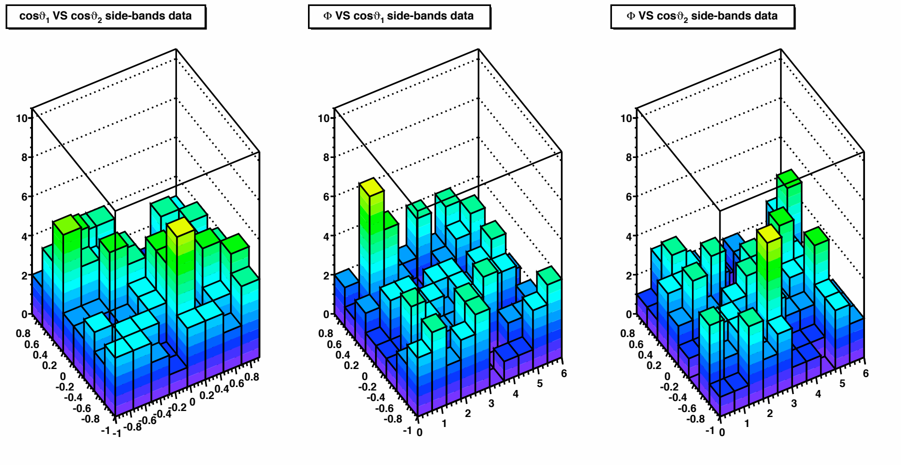

Figure 21: Scatter plots for test of angular variables correlation in the side-band regions. On the right, $\cos\vartheta_1$ versus $\cos\vartheta_2$. In the middle, $\cos\vartheta_1$ versus Φ. On the left, $\cos\vartheta_2$ versus Φ.

We perform a binned fit to the sideband angular distributions using the above equations. Though this is a simple description, we find that it is adequate to describe the angular distributions in the sidebands (see Figure 22).

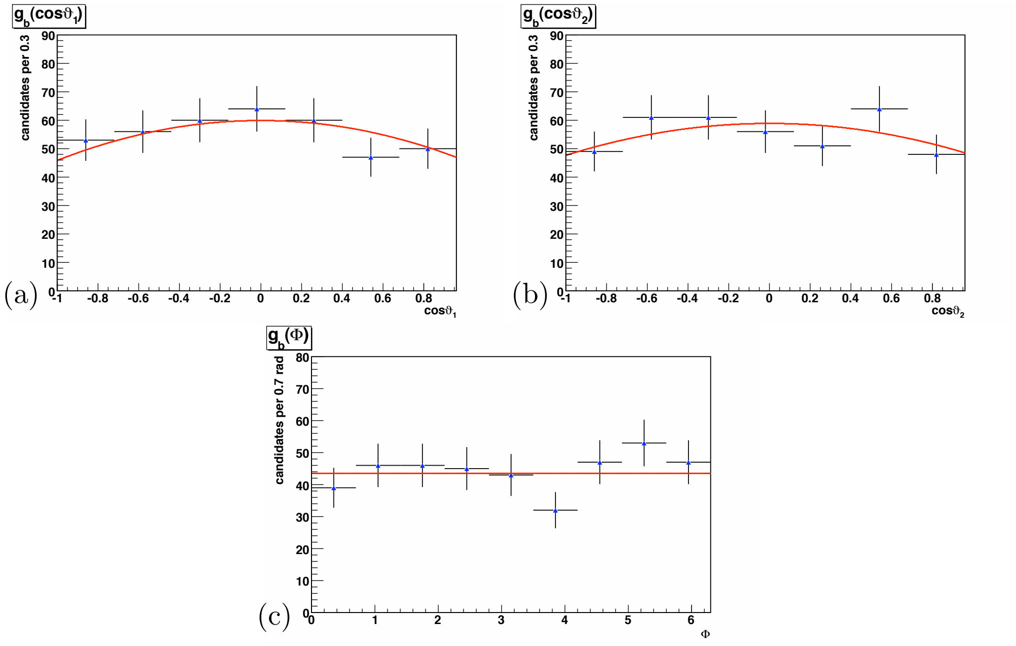

Figure 22: Side-bands data fit to determine the background parametrizations for the $B_s^0 \to \phi\phi$ decay: $\cos\vartheta_1$ (a), $\cos\vartheta_2$ (b) and $\varPhi$ (c). Black points are side-bands data; red lines are the fitting functions described in the text.

7.4.6 Parameters Summary

Let us summarize all the parameters that enter the complete Likelihood in the final fit. The input variables are the mass m and the helicity angles $\vec{\omega} = (\vartheta_1, \vartheta_2, \varPhi)$ for each reconstructed candidate that passed the off-line selection. The eight fit parameters are reported in tab. 7.

	Signal	Background
Mass	M, σ	f_{b}, b
Angular	$\lvert A_0\rvert^2$, $\lvert A_\parallel\rvert^2$, $\cos\delta_\parallel$	B

Table 7: Parameters summary of the time-integrated $B_s^0 \to \phi\phi$ fit.

The following quantities are fixed in the final fit:

- k and h, from the MC fit;
- τ_{L} and τ_{L}, the two mean life-time of the B_s^0 mass eigenstates, are taken from the last PDG values (eq. (6a));

Initially a slightly different set of parameters has been employed, which used $\delta_\parallel$ instead of $\cos\delta_\parallel$ and a different parametrization of the angular background pdf. The description and the results of this fitter version are reported in Appendix C. The use of $\cos\delta_{\|}$ instead of $\delta_{\|}$ in the angular signal model (see eq. 20) allows us to avoid some issues concerning the $\delta_{\|}$ estimates, both in the pulls distributions test and in the likelihood scan (see App.C). The likelihood as a function of $\cos\delta_{\|}$ is expected to be more regular, at the very least because it lacks the double minima present when fitting directly for the strong phases. Although the fit may allow unphysical values ($|\cos\delta_{\|}| > 1$), we do not put bounds neither in the pdf definition nor in the minimization process.

Before carrying out the fit over the data sample, we perform several tests. The aim is to validate the correctness of the implementation, to investigate the likelihood behavior as function of the parameters, to look at their resolutions and to detect any potential fit biases. The tests that we perform are:

1. the pulls distributions;
2. the fit of $B_s^0 \to J/\psi\phi$, used as a control sample;
3. the fit of the realistic MC;

They are described in the following sections.

7.5 Pulls Distributions

The study of pulls distributions are a commonly used method. The procedure is as follows: we generate a large set of pseudo-experiments (referred to as "toysMC"), randomly polling the probability density function in each variable subspace to assign a value to the event variables. As a consequence, each pseudo-experiment yields a different random sample of events. For each of these pseudo-experiments, we perform a fit in the same way we do on the data. For each parameter ξ_i on the fit, the corresponding pull $\mathcal{P}_i$ is defined as:

$$\mathcal{P}_i = \frac{\xi_i^{\text{fit}} - \xi_i^{\text{input}}}{\sigma_i} \tag{29}$$

where ξ_i^{input} is the parameter assigned in the random generation of the pseudo-experiment variables, ξ_i^{fit} is its value found by the fitter, and σ_i is its uncertainty. In principle, the variables $\mathcal{P}_i$ are gaussian distributed, with mean and width equal to 0 and 1, respectively. Thus, if the fitter is correct, we expect to find this kind of pulls distributions.

7.5.1 Expected Resolution on the Polarization Observables

We perform the pulls test for the fitter, generating 1000 pseudo-experiments of 480 events for each (the statistic of the actual sample). The generation of pseudo-experiments is done using as input parameters the results of the fit performed on the actual $B_s^0 \to \phi\phi$ sample (see Sec.7.8). We observe that in about 2% of the pseudo-experiments the fits fails because MIGRAD is not able to minimize the Likelihood. The results of this test are reported in tab. 8, and the pulls distributions are shown in fig. 23. The parameters resolution (third column of the table) are consistent with the one expected in Sect. 1 (4%).

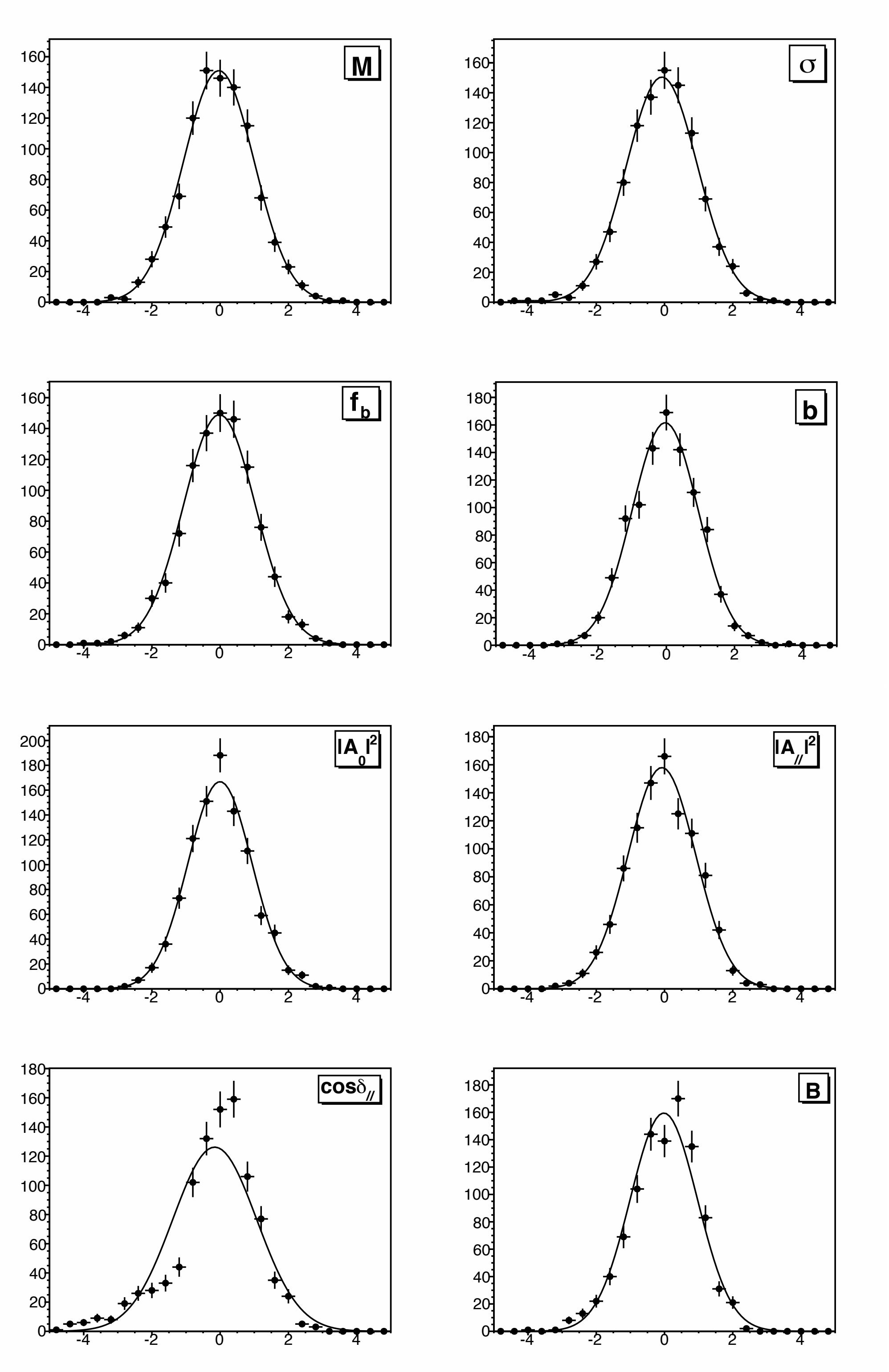

Figure 23: Pulls distributions of fit parameters for $B_s^0 \to \phi\phi$ (480 events per pseudo-experiment).

Parameter	Input value	Average fit error	Mean	Variance	Prob(χ^2) [%]
M	5.364 GeV/c^2	0.0012 GeV/c^2	-0.04 ± 0.03	1.04 ± 0.02	87
σ	0.016 GeV/c^2	0.0010 GeV/c^2	-0.08 ± 0.03	1.04 ± 0.02	84
$f_{\rm b}$	0.38	0.03	-0.02 ± 0.03	1.05 ± 0.02	95
b	2.7 c^2/GeV	0.7 c^2/GeV	-0.03 ± 0.03	0.97 ± 0.02	74
$\|A_0\|^2$	0.35	0.040	0.01 ± 0.03	0.94 ± 0.02	64
$\|A_\parallel\|^2$	0.29	0.039	0.08 ± 0.03	0.99 ± 0.02	69
$\cos\delta_\parallel$	-0.90	0.15	-0.16 ± 0.03	1.23 ± 0.02	0
B	0.5	0.3	0.02 ± 0.03	0.98 ± 0.02	0

Table 8: Pulls mean and variance for $B_s^0 \to \phi\phi$ (480 events per pseudo-experiment). In the second column the input parameters of the generation are listed. The third column reports the average error in the pseudo-experiments fit (resolution). The fourth and the fifth columns list the mean value and the variance of the pull distributions, respectively. The sixth column presents the χ^2 probability for a gaussian fit of the pulls distribution with mean and variance 0 and 1, respectively.

We find that the fitter returns unbiased estimates for all parameters, except for the $\cos\delta_\parallel$ parameters that nevertheless show a much better behaviour than in the fit for the phase itself, actually the accumulation of experiments with a minimum at exactly π has disappeared (see App. C). There is also a tiny bias in the $|A_\parallel|^2$ of order of 0.3%. As already seen in Sec. C.2.1), the uncertainties of $|A_0|^2$ seems to be a little overestimated by as much as 6%.

To investigate further the non gaussian nature of the $\cos\delta_\parallel$ pull, we notice that the pull has a smooth but asymmetric distribution so we conclude it might be related to a non perfectly symmetric behaviour of the fitting function in the vicinity of its minimum. Thus we perform the fit of the pseudo-experiments using MINOS errors from MINUIT. We adopt the convention that the pull for a given pseudo-experiment is calculated using the positive (negative) error in the denominator if the fit value is lower (higher) than the input value.

The results of this test are shown in tab. 9 and the pulls plots are in fig. 24. We observe an increase in the number of failing fits (being slightly less than 10% of the total), but we find a great improvement for the $\cos\delta_\parallel$: the shift of the averaged fitted value from the input one is only -0.02 and the distribution of the pull is very close to a gaussian distribution.

Thus we use the version of the fit with MINOS errors for our final fit on data.

7.5.2 Pulls test for randomly generated input parameters

We perform the pulls test with random input parameter for the angular part for each pseudo-experiment while the input parameters of the mass part are kept fixed. We generate 2000 pseudo-experiments of 480 events each. $|A_0|, |A_\parallel|, |A_\perp|$ are randomly chosen in the range between 0 and 1, imposing the constraint $|A_0|^2 + |A_\parallel|^2 + |A_\perp|^2 = 1$; $\cos(\delta_\parallel)$ is generated randomly between -0.98 and 0.98; the background angular shape parameter, B, is varied in the 2σ region around the B fitted value.

The results are illustrated in the fig. 25 and in tab. 10.

7.5.3 Additional tests

A pull test with higher statistics pseudo-experiments has been performed with the other fit version and it it described in C.2. Working with large data samples allows one to decrease the pulls parameters uncertainty and to have a better control on the result, since different complications

Parameter	Input value	Avg Neg. Err	Avg Pos. Err	Mean	Variance	Prob(χ^2) [%]
M	5.364 GeV/c^2	-0.0012 GeV/c^2	0.0012 GeV/c^2	-0.03 ± 0.03	1.04 ± 0.02	91
σ	0.016 GeV/c^2	-0.0010 GeV/c^2	0.0010 GeV/c^2	-0.05 ± 0.03	1.04 ± 0.02	95
f_{b}	0.38	-0.03	0.03	-0.07 ± 0.03	1.04 ± 0.02	62
b	2.7 c^2/GeV	-0.7 c^2/GeV	0.7 c^2/GeV	-0.03 ± 0.03	0.97 ± 0.02	86
$\lvert A_0\rvert^2$	0.35	-0.040	0.040	0.03 ± 0.03	0.93 ± 0.02	62
$\lvert A_\parallel\rvert^2$	0.29	-0.039	0.039	0.06 ± 0.03	0.99 ± 0.02	22
$\cos\delta_\parallel$	-0.90	-0.15	0.18	-0.02 ± 0.03	1.10 ± 0.02	0
B	0.5	-0.27	0.30	0.02 ± 0.03	0.98 ± 0.02	3

Table 9: Pulls mean and variance for $B_s^0 \to \phi\phi$ (480 events per pseudo-experiment, MINOS implementation). In the second column the input parameters of the generation are listed. The third column reports the average negative error in the pseudo-experiments fit, while the fourth column shows the average positive error. The fifth and the sixth columns list the mean value and the variance of the pull distributions, respectively. The seventh column presents the χ^2 probability for a gaussian fit of the pulls distribution with mean and variance 0 and 1, respectively.

Parameter	Input value	Avg Neg. Err	Avg Pos. Err	Mean	Variance	Prob(χ^2) [%]
M	5.364 GeV/c^2	-0.0012 GeV/c^2	0.0012 GeV/c^2	-0.01 ± 0.03	1.03 ± 0.02	0.69
σ	0.016 GeV/c^2	-0.0010 GeV/c^2	0.0010 GeV/c^2	-0.08 ± 0.03	1.00 ± 0.02	0.01
f_{b}	0.38	-0.03	0.03	-0.10 ± 0.03	1.03 ± 0.02	0.23
b	2.7 c^2/GeV	-0.7 c^2/GeV	0.7 c^2/GeV	-0.02 ± 0.02	0.98 ± 0.02	0.17
$\lvert A_0\rvert^2$	see text	-0.037	0.037	0.04 ± 0.02	0.98 ± 0.02	0.22
$\lvert A_\parallel\rvert^2$	see text	-0.037	0.038	0.00 ± 0.02	1.00 ± 0.02	0.23
$\cos\delta_\parallel$	see text	-0.24	0.23	0.01 ± 0.02	0.99 ± 0.02	0.71
B	see text	-0.27	0.30	-0.10 ± 0.03	0.89 ± 0.02	0

Table 10: Pulls mean and variance for $B_s^0 \to \phi\phi$ (480 events per pseudo-experiment, MINOS implementation, randomly generated inputs).

can arise in presence of low statistics. We perform the test with about 200 times the events per experiment that we have in the actual $B_s^0 \to \phi\phi$ data samples, so it is mostly a test of the fitter as a machinery to correctly extract the parameters given in input to generate the toyMC sample. The results of this test are very satisfactory.

In App.C a pull test using four different sets of input values are reported as well. This check allow us to verify that the fitter estimates unbiased parameters independently of the specific value of the input parameters.

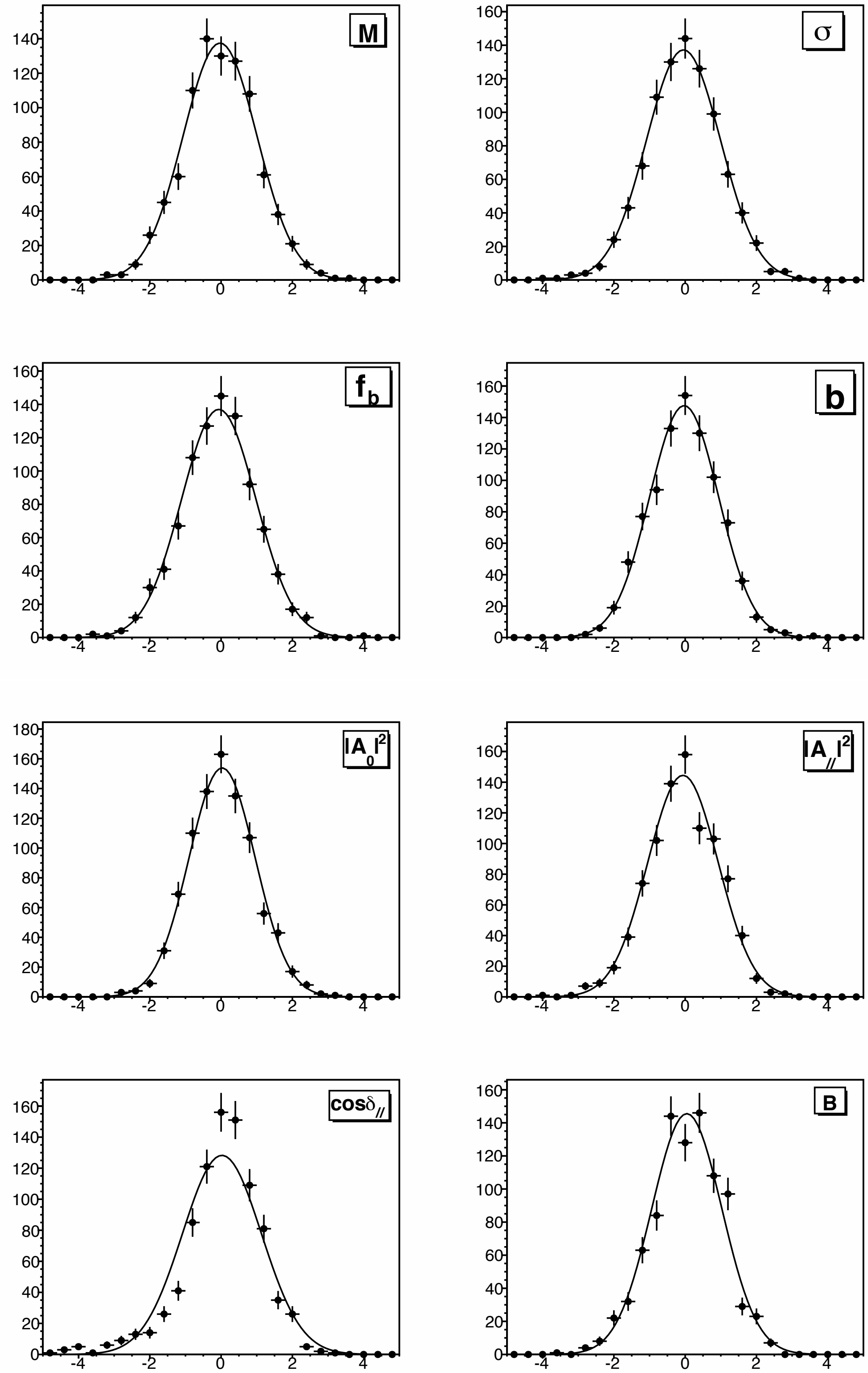

Figure 24: Pulls distributions of fit parameters for $B_s^0 \to \phi\phi$ (480 events per pseudo-experiment, MINOS implementation).

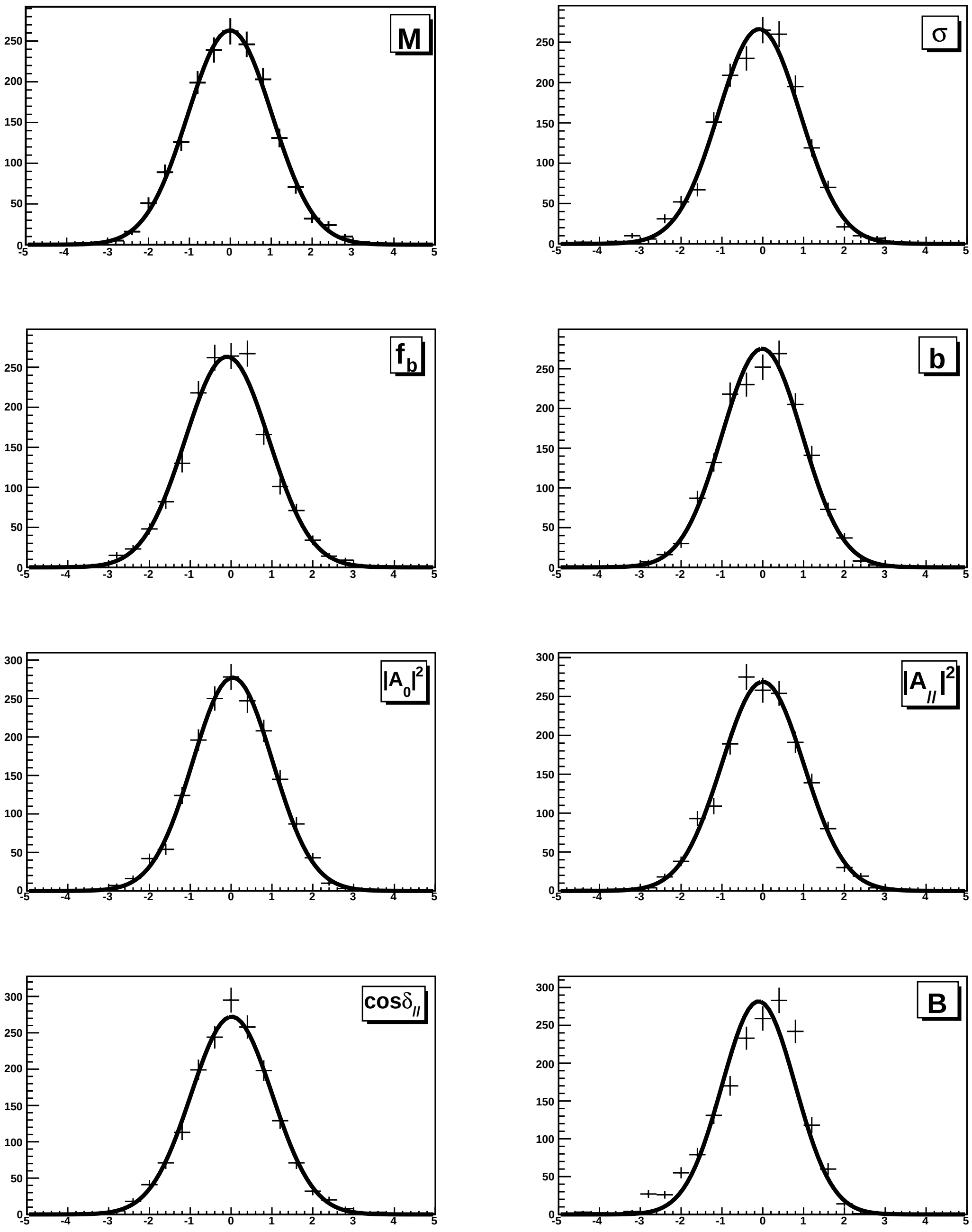

Figure 25: Pulls distributions of fit parameters for $B_s^0 \to \phi\phi$ (480 events per pseudo-experiment, MINOS implementation, randomly generated inputs).

7.6 Fit to the TTT $B_s^0 \to J/\psi\phi$ Sample

The second test is the implementation of the developed framework to fit the $B_s^0 \to J/\psi\phi$ data sample collected with the same TTT selection of the $B_s^0 \to \phi\phi$ decay (see previous Section). We use the $B_s^0 \to J/\psi\phi$ decay mode as a control sample: we compare the results coming from our fit with the ones obtained in the different analysis published in [1], whose events was collected at CDF II by a different trigger selection, the Dimuon trigger. Therefore, the control sample serves the purpose of improving the reliability of the main analysis. In this section, we summarize the procedure and we discuss the results for the $B_s^0 \to J/\psi\phi$, leaving the analysis details in the Appendix D.

For its intrinsic nature of control sample, many of the technical aspects are in common with the $B_s^0 \to \phi\phi$ analysis. The main difference is that the $B_s^0 \to J/\psi\phi$ decay is described making use of the transversity angles $\vec{\Omega} = (\Theta, \Psi, \Phi)$ presented in Sect. A.2.

First, we build the likelihood function for this case. The pdf structure is the same of eq. 15. In particular, the pdf components are described by:

- the equations 18 and 19 for the mass parametrization, since the distribution is similar to the $B_s^0 \to \phi\phi$ one (compare fig. 3 and fig. 2). The parameters of the second gaussian is fixed from the fit to the MC data (see App. D).
- The equation 20 provides the signal angular parametrization, replacing the functions $f_i(\vec{\omega})$ and the phase ϕ_s by $f_i(\vec{\Omega})$ (eq. 12) and by $2\beta_s$, respectively. As in the main analysis:
  - we assume no CP-violation, fixing $\beta_s = 0$;
  - we set Γ_L and Γ_H to the latest PDG values;
  - the angular acceptance is taken from the three-dimensional histogram of the PHSP MC;
  - the angular background term comes from the parametrization of the sidebands events.

Then, the fitter (version in App.C) is subjected to two tests: the pulls distributions and the fit to the real MC data sample. They are reported in the App. D.

7.6.1 Fit Results and Projections

The results of the fit performed on 2.9 fb^{-1} of data for the $B_s^0 \to J/\psi\phi$ are listed in the table 11. The fit projections onto the three transversity angles are shown in fig. 26.

Parameter	Our fit value
$\|A_0\|^2$	0.534 ± 0.019
$\|A_\parallel\|^2$	0.220 ± 0.025
$\delta_\parallel$	3.14 ± 0.45

Table 11: Parameters of angular fit for $B_s^0 \to J/\psi\phi$.

7.6.2 Comparison with the Dimuon Sample Results

We compare the results in tab. 11 with the ones obtained in the analysis published in [1], whose data were collected by the CDF II detector between February 2002 and January 2007, and correspond to an integrated luminosity of 1.7 fb^{-1}. First, we briefly summarize that analysis.

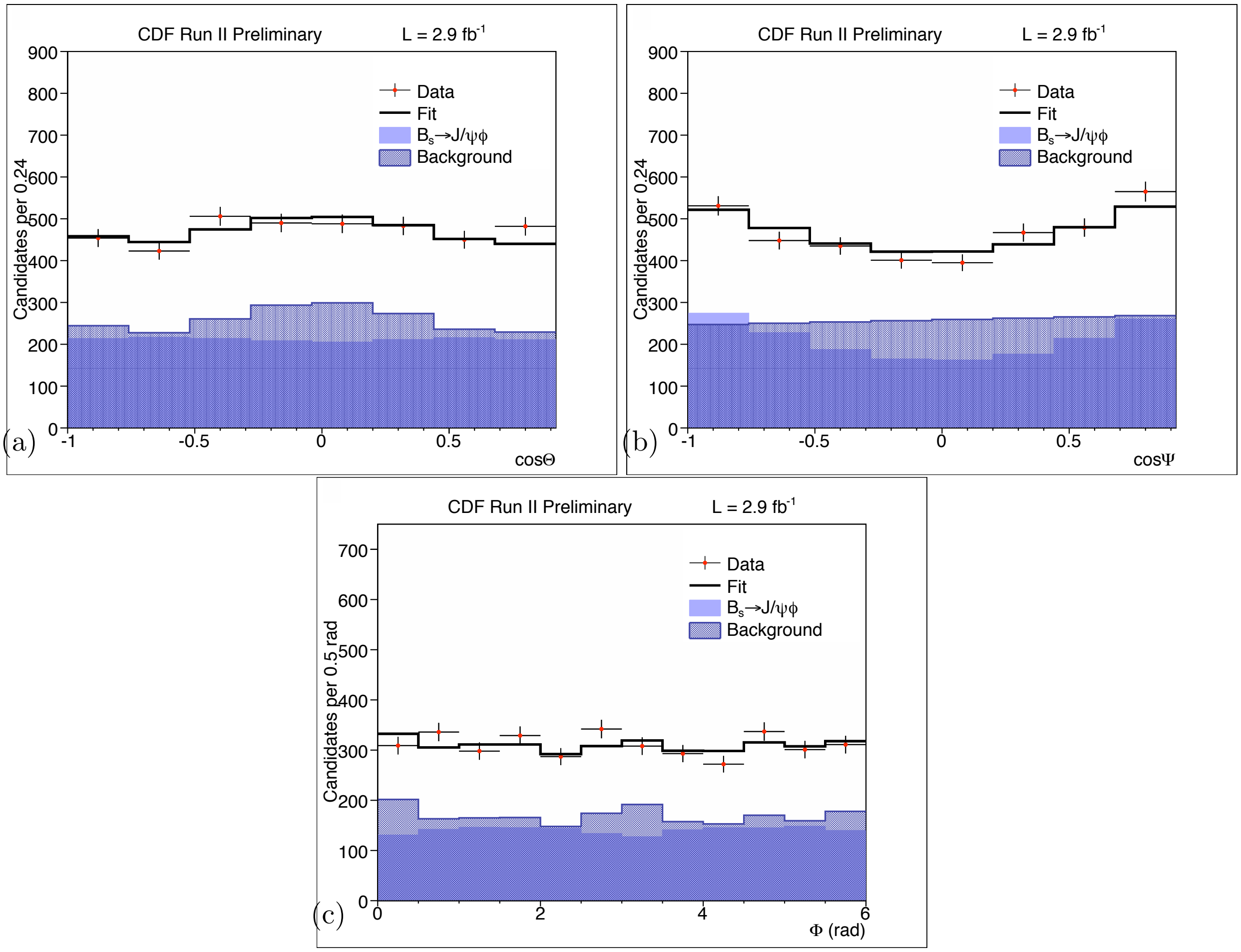

Figure 26: Angular fit projections for $B_s^0 \to J/\psi\phi$: $\cos\Theta$ (a), $\cos\Psi$ (b) and Φ (c). The χ^2 probabilities of the fit projections are 0.37, 0.25 and 0.21 respectively.

The events with $J/\psi \to \mu^+\mu^-$ decays were recorded using a different trigger selection. This is the Dimuon trigger, which requires two oppositely-charged COT tracks matched to muon chamber track segments with a dimuon mass between 2.7 and 4.0 GeV/c^2 .

In the offline analysis, $B_0 \to J/\psi\phi$ decays are reconstructed making use of an artificial neural network (ANN). The ANN is trained to separate B_s^0 decays from the combinatorial background, which is the dominant one. The signal is modeled with simulated events and data from B_s^0 mass sidebands are used to model the combinatorial background. The input variables to the ANN are kinematic quantities, vertex fit quality parameters, and particle-identification information obtained from the muon system, the time-of-flight detector, and the dE/dx measurements. The requirement on the ANN output is selected by maximizing the significance $S/\sqrt{S+B}$ on data where S (B) is the number of signal (background) events in a $\pm 20\text{MeV}/c^2$ window around the B_s^0 mass peak position. The selected sample contains about 2500 $B_s^0 \to J/\psi\phi$ decays. The ratio S/B is about 30%. In our Two Track Trigger sample we have $S = 1766$ and $S/B \simeq 70\%$, thus, even if we collect a low statistic, we can reach the same resolution for the fitted parameters.

To extract the parameters, an unbinned ML fit is performed with pdf depending on mass, lifetime, and transversity angles. For the pdf of the background, empirical models are used with floating fit parameters determined from the data. Because correlations among the three angles are negligible, the angular pdf can be factorized as a product of polynomials in $\cos^2\Theta$, $\cos 2\Phi$ and $\cos\Psi$.

The lifetime-angular distribution without acceptance effects is given by eq. 2. The analysis is time dependent, since it is aimed at the estimation of $\Delta\Gamma_s$. The angular distribution of the B_s^0 decays is modified by the detector acceptance as well as trigger and selection efficiencies. This effect is taken into account with an acceptance function, $\mathcal{A}(\vec{\Omega})$, derived from simulated $B_s^0 \to J/\psi\phi$ decays. The factor $\mathcal{A}(\vec{\Omega})$ is described by a three-dimensional histogram with 20 bins in each of the angles, as we made in the $B_s^0 \to \phi\phi$ analysis. The dominant source of systematic uncertainties on the amplitudes is the angular background model. Under the assumption of CP conservation ($\beta_s = 0$), the result in tab. 12 are obtained. The first uncertainties are statistical, the second ones systematic. They do not quote an estimate of the strong phase because its likelihood profile is non-parabolic and this makes the uncertainty estimate unreliable. The fit projection are shown in fig. 27.

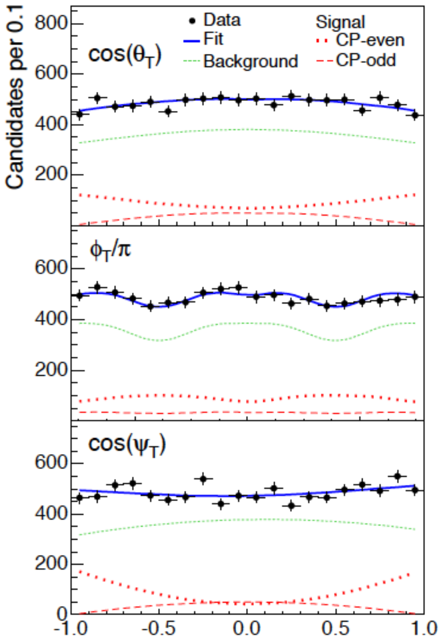

Figure 27: Angular projections for $B_s^0 \to J/\psi\phi$ in [1].

The agreement of our results with the ones published in [1] is very satisfactory: the central values are consistent within the uncertainty ranges. For a better comparison, we report the two analysis results in the same table (12). In conclusion, the two experiments have compatible results among each other and provide us with an important successful check of our framework on the kinematically equivalent data sample $B_s^0 \to J/\psi\phi$: this result contributes to enforce the reliability of our angular analysis implementation.

Parameter	Our fit result	Dimuon sample result
$\lvert A_0\rvert^2$	0.534 ± 0.019(stat)	0.531 ± 0.020(stat) ± 0.007(syst)
$\lvert A_\parallel\rvert^2$	0.220 ± 0.025(stat)	0.239 ± 0.029(stat) ± 0.011(syst)

Table 12: Comparison of our fit results and the ones in [1] for $B_s^0 \to J/\psi\phi$.

7.7 Fit to the Realistic MC

The fit to the realistic MC data sample is the third test that we present. The MC is called "realistic" because it reproduces in order the main physical processes and the processing steps involved in collecting data from real pp̄ interactions, as described in Sect. 6. We use the "SVV HELAMP" model. The used fitter version is described in App.C.

The purpose of the test is to check if the fit is reliable. This means that the fit should return the same set of parameters adopted in the MC generation of the events. We produce and fit three realistic MC samples, with different polarization values in the generation. The results are presented in the following:

(i) a sample of 21000 events (70 times the signal data yield):

Parameter	generated value	fitted value
$\lvert A_0\rvert^2$	0.48	0.4815±0.0042
$\lvert A_\parallel\rvert^2$	0.28	0.2824±0.0041
$\delta_\parallel$ [rad]	0.742	0.735±0.019

The projections of the fits on the three angular distributions are shown in fig. 28.

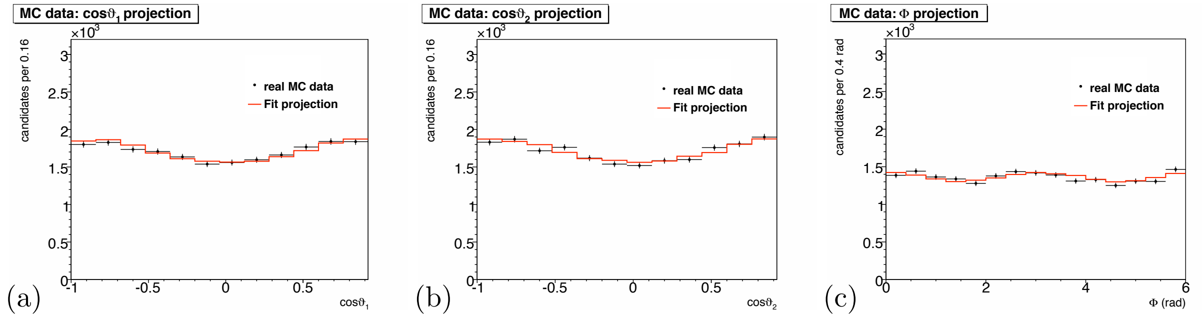

Figure 28: Angular fit projections of realistic MC sample (i): $\cos\vartheta_1$ (a), $\cos\vartheta_2$ (b) and Φ (c). The χ^2 probabilities of the fit projections are 0.69, 0.19 and 0.22 respectively.

(ii) A sample of 12000 events (40 times the signal data yield):

Parameter	generated value	fitted value
$\lvert A_0\rvert^2$	0.81	0.8191±0.0039
$\lvert A_\parallel\rvert^2$	0.15	0.1436±0.0037
$\delta_\parallel$ [rad]	0.442	0.437±0.033

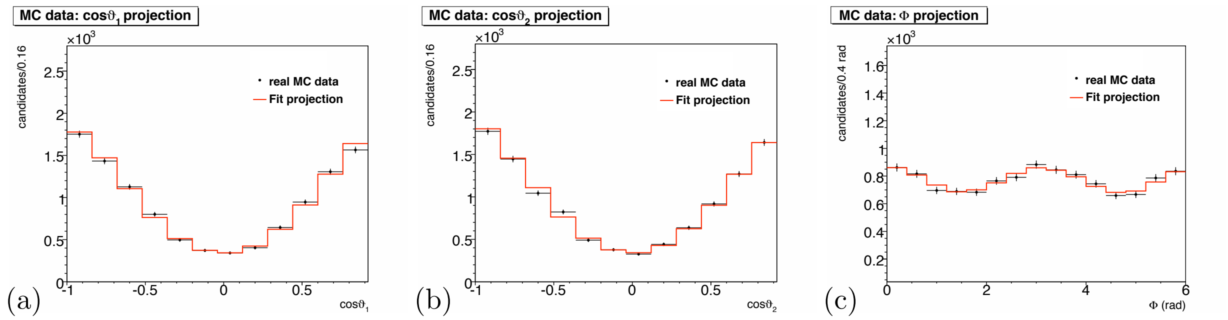

Figure 29: Angular fit projections of realistic MC sample (ii): $\cos\vartheta_1$ (a), $\cos\vartheta_2$ (b) and $\varPhi$ (c). The χ^2 probabilities of the fit projections are 0.41, 0.38 and 0.88 respectively.

The projections of the fits on the three angular distributions are shown in fig. 29.

(iii) A sample of 240000 events (800 times the signal data yield):

Parameter	generated value	fitted value
$\lvert A_0\rvert^2$	0.333	0.3276±0.0013
$\lvert A_\parallel\rvert^2$	0.333	0.3344±0.0014
$\delta_\parallel$ [rad]	1.571	1.5667±0.051

The projections of the fits on the three angular distributions are shown in fig. 30.

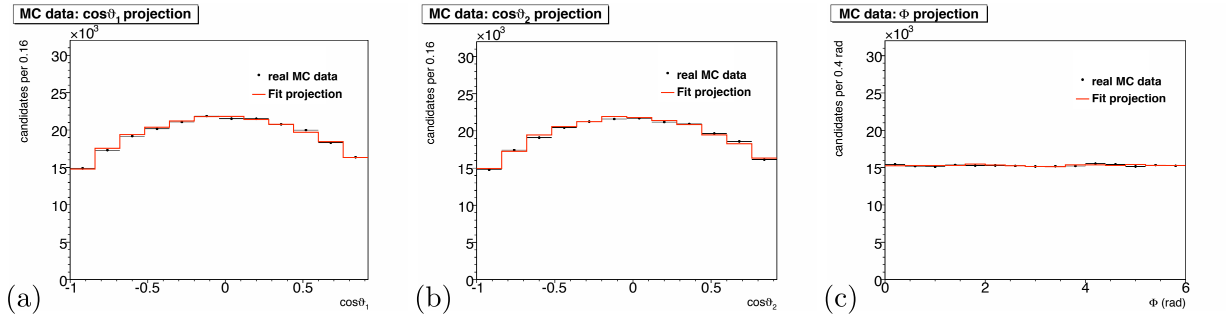

Figure 30: Angular fit projections of realistic MC sample (iii): $\cos\vartheta_1$ (a), $\cos\vartheta_2$ (b) and $\varPhi$ (c). The χ^2 probabilities of the fit projections are 0.04, 0.001 and 0.22 respectively.

The results of this test is very satisfactory, since for each MC samples the fit returns etimates very close to the generating values, and the distributions are very well reproduced by the fitting functions.

7.8 Time-integrated Fit to Real Data

The results of the fit performed on 2.9 fb^{-1} of data for the $B_s^0 \to \phi\phi$ are finally listed in the table 13. We observe that the statistical uncertainties of the polarization amplitudes are of the same order of the ones that we have quoted in Sect. 1 and the obtained estimates are consistent with the previous fit results (table 30 in App. C). The fit estimates for $\cos\delta_\parallel$ is in the physical region and it is in agreement with the estimates of the strong phase reported in App. C, since $\delta_{\|} = \arccos(-0.91) = 2.71$. The correlation coefficients are listed in tab. 14.

We perform a MINOS analysis to get the asymmetric errors, to be consistent with the pulls study results. They are reported in tab. 15. We consider the asymmetic errors only for $\cos\delta_{\|}$ and B estimates.

Parameter	Fit value
M [GeV/c^2]	5.3636 ± 0.0012
σ [GeV/c^2]	0.0165 ± 0.0011
f_{b}	0.381 ± 0.030
b [c^2/GeV]	2.68 ± 0.67
$\lvert A_0\rvert^2$	0.348 ± 0.041
$\lvert A_{\|}\rvert^2$	0.287 ± 0.043
$\cos\delta_{\|}$	$-0.91^{+0.15}_{-0.13}$
B	$0.49^{+0.31}_{-0.26}$

Table 13: Results of the new time-integrated fit for $B_s^0 \to \phi\phi$.

	M	σ	f_{b}	b	$\lvert A_0\rvert^2$	$\lvert A_{\|}\rvert^2$	$\cos\delta_{\|}$	B
M	+1.000	−0.047	+0.049	+0.070	+0.002	−0.008	−0.010	+0.010
σ	−0.047	+1.000	−0.357	−0.022	+0.055	−0.025	+0.110	+0.036
f_{b}	+0.029	−0.357	+1.000	+0.020	−0.064	+0.023	−0.147	−0.034
b	+0.070	−0.022	+0.020	+1.000	−0.005	−0.002	−0.000	+0.003
$\lvert A_0\rvert^2$	+0.002	+0.055	−0.064	−0.005	+1.000	−0.447	+0.133	−0.217
$\lvert A_{\|}\rvert^2$	−0.008	−0.025	+0.023	−0.002	−0.447	+1.000	+0.092	+0.106
$\cos\delta_{\|}$	−0.010	+0.110	−0.147	−0.000	+0.133	+0.092	+1.000	+0.025
B	+0.010	+0.036	−0.034	+0.003	−0.217	+0.106	−0.025	+1.000

Table 14: Correlation coefficients of the new time-integrated fit for $B_s \to \phi\phi$.

Parameter	Negative Error	Positive Error
M [GeV/c^2]	−0.0012	0.0012
σ [GeV/c^2]	−0.0011	0.0012
f_{b}	−0.030	0.030
b [c^2/GeV]	−0.67	0.68
$\lvert A_0\rvert^2$	−0.041	0.041
$\lvert A_{\|}\rvert^2$	−0.042	0.044
$\cos\delta_{\|}$	−0.13	0.15
B	−0.26	0.31

Table 15: Asymmetric errors of the new fit estimates

The time-integrated fit projections onto the three helicity angles are shown in fig. 31: we see that the data distributions are very well reproduced by the fitting functions. The χ^2 probabilities of the fit projections are 0.52 for $\cos\vartheta_1$, 0.57 for $\cos\vartheta_2$ and 0.10 for $\varPhi$.

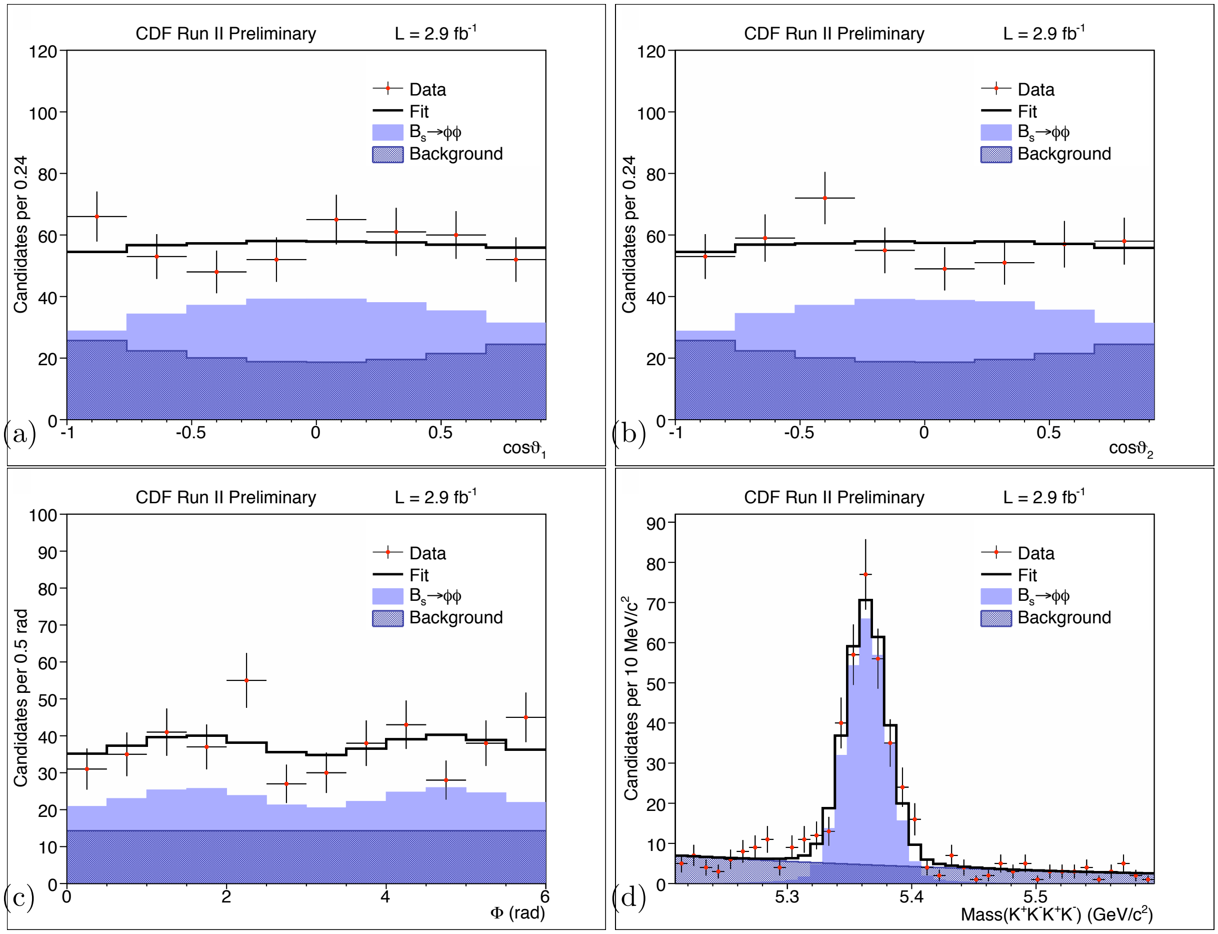

Figure 31: Projections of the time-integrated fit for $B_s^0 \to \phi\phi$: $\cos\vartheta_1$ (a), $\cos\vartheta_2$ (b), Φ (c) and the mass (d). The χ^2 probabilities of the fit projections are 0.46, 0.62, 0.11 and 0.07 respectively.

7.8.1 Likelihood Scan

The results are given in terms of the ML estimates. Therefore the likelihood parabolic behavior for the relevant parameters has to be checked. This can be achieved with the likelihood scans. In a scan, the value of the likelihood function is sampled by varying a certain parameter, leaving all other parameters fixed at the estimated value. The curve resulting from each scan is plotted in order to show the approximate behavior of the likelihood.

In fig. 32 the likelihood scans for the polarization parameters are plotted. The scans of $\cos\delta_{\|}$ shows the expected parabolic behavior mandatory to be able to have a reliable point estimate: the double minima behavior of the likelihood of the previous fit version (App.C) disappears. The scan shows also the asymmetric profile respect to the minimum value (the fit estimate is represented by the dotted blue line).

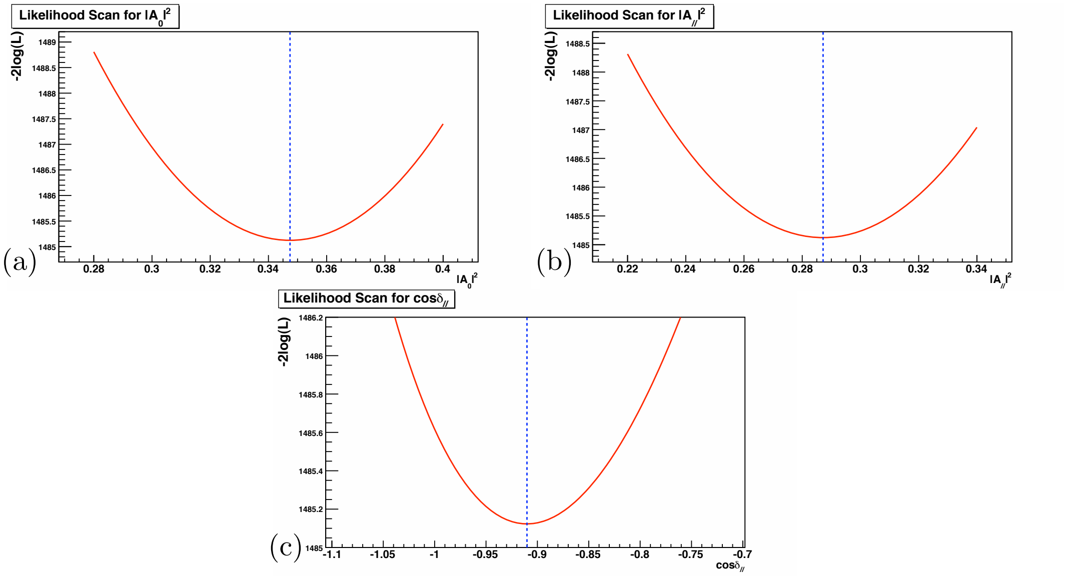

Figure 32: Likelihood scans of the time-integrated fit for $B_s^0 \to \phi\phi$: $|A_0|^2$ (a), $|A_{\|}|^2$ (b) and $\cos\delta_{\|}$ (c). The blue dotted lines represent the fit estimates.

7.8.2 Parameters Contour-Plots

The contour-plots for the three polarization parameters are shown in fig. 33: each of these is a regular ellipse whose center coordinates are the fit estimates (blue dotted line). The contour calculated is dynamic, in the sense that it represents the minimum of the Likelihood function with respect to all the other $n-2$ parameters. In statistical terms, this means that the contour takes account of the correlations between the two parameters being plotted, and all the other variable parameters. These contour-plots provides the actual coordinates of the points around the contour calculated at the level $-\log(\mathcal{L}(\vec{\xi}_{\min}))+0.5$.

The ellipses for the case where $\cos(\delta_{\|})$ was unbounded and the case where the $|\cos(\delta_{\|})| < 1$ condition is applied are compared in fig. 34. No difference can be appreciated. We found no problem with $\cos(\delta_{\|})$ bounded in the physical region for both the 1 sigma and the 68% CL curves.

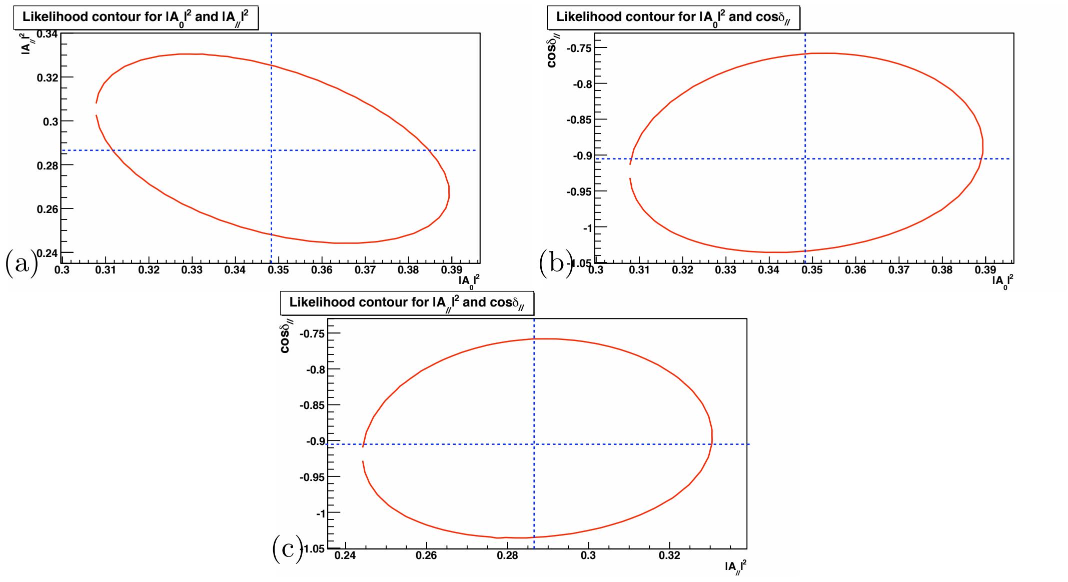

Figure 33: Contour-plots of the time-integrated fit for $B_s^0 \to \phi\phi$: $|A_0|^2$ versus $|A_{\|}|^2$ (a), $|A_0|^2$ versus $\cos\delta_{\|}$ (b) and $|A_{\|}|^2$ versus $\cos\delta_{\|}$ (c). The blue dotted line represents the fit estimates.

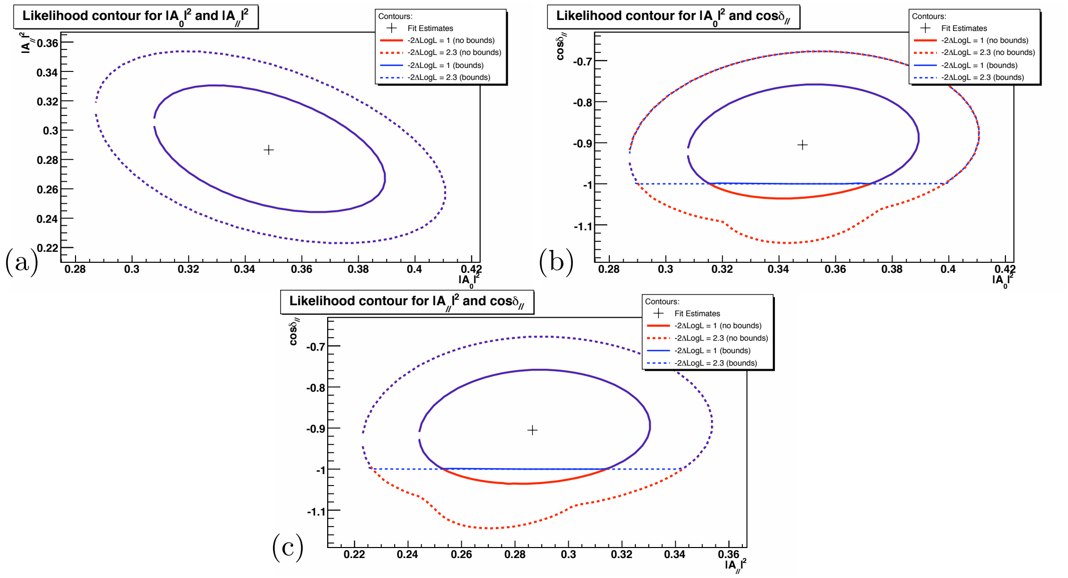

Figure 34: Comparison between contour-plots where $\cos(\delta_{\|})$ was bounded or unbounded. In figure: $|A_0|^2$ versus $|A_{\|}|^2$ (a), $|A_0|^2$ versus $\cos\delta_{\|}$ (b) and $|A_{\|}|^2$ versus $\cos\delta_{\|}$ (c). The 68% CL curves are shown as well.

8 Other studies

8.1 Fit of each trigger-path sample

We separately fit the data set coming from each of the three trigger-paths selection and we compare the fit estimates with the (default) fit on the sample of the sum of the exclusive trigger-paths data sets. The results are reported in tab. 16; the fourth row presents the averaged values of the estimates of the three previous row. All central values are consistent within one sigma. The previous fitter version is used (App.C).

	$\vert A_0\vert^2$	$\vert A_\parallel\vert^2$	$\delta_\parallel$ [rad]
`HIGHPT`	0.391±0.066	0.219±0.065	2.60±0.49
`LOWPT`	0.360±0.064	0.327±0.070	3.14±0.49
`ScA`	0.352±0.088	0.349±0.098	2.33±0.44
averaged value	0.370±0.041	0.284±0.043	2.66±0.27
default fit	0.347±0.041	0.287±0.043	2.71±0.34

Table 16: Results of the fit for each trigger-path sample.

8.2 Fit on samples with different S/B

We change the off-line selections in order to obtain samples with a different S/B ratio and check if the fit every times finds estimates in agreement with the fit on the default sample. The acceptance histograms are computed for each selections set.

The samples are selected with:

1. a tighter selection for $p_{\mathrm{T}}(K)$: from the default requirement $p_{\mathrm{T}}(K)$ >0.7 GeV/c to $p_{\mathrm{T}}(K)$ >1.0 GeV/c. The fit range is [5.28;5.44] GeV/c^2, which is about three sigma around the signal mass peak (the default range is [5.2;5.6] GeV/c^2). The number of events selected becomes 312 respect to 472 (default). The background fraction becomes 0.22 respect to 0.38 (default), thus, we have $S/B = 3.5$, instead of $S/B = 1.62$ (default).
2. We remove the $d_0^{\phi_{\max}}$ selection, and we make the requirement $\chi^2_{xy} < 25$ instead of $\chi^2_{xy} < 17$ (default). The number of events selected becomes 700 and the background fraction becomes 0.59, thus, we have $S/B = 0.69$.

We obtain the result reported in tab. 17. All central values are consistent within one sigma.

S/B	$\vert A_0\vert^2$	$\vert A_\parallel\vert^2$	$\cos\delta_\parallel$ [rad]
3.5	0.353±0.046	0.317±0.048	$-0.90^{+0.15}_{-0.14}$
0.69	0.352±0.043	0.304±0.046	$-0.87^{+0.16}_{-0.15}$
1.62 (default)	0.348±0.041	0.287±0.043	$-0.91^{+0.15}_{-0.13}$

Table 17: Results of the fit for samples with different S/B ratio.

These results show that for different level of background the fitted parameters values are stable and the statistical uncertainty does not improve either by reducing or by increasing the background (and signal) composition. This gives us an indication that having the same signal selection for both the BR and the polarization measurements is acceptable and it is foreseable that no big improvement should come from a more specific selection optimization.

8.3 Fit of different ct-slices of realistic MC

We study if the fit estimates change in five different ct-slices of the realistic MC sample (iii) (see Sect. 7.7). The used fitter version is described in App.C. We proceed as follow:

- we divide the realistic MC sample (iii) in five sets, one for each of the following ct intervals:
    1. "slice 1", for events which have $ct \in [0.0000; 0.0375]$ cm;
    2. "slice 2", for events which have $ct \in]0.0375; 0.0550]$ cm;
    3. "slice 3", for events which have $ct \in]0.0550; 0.0750]$ cm;
    4. "slice 4", for events which have $ct \in]0.0750; 0.0950]$ cm;
    5. "slice 5", for events which have $ct \in]0.0950; 0.5000]$ cm.
- we bin the three-dimensional histogram $H(\vec{\omega})$ in five slices of ct (see fig. 35); thus, we deal with five different acceptance curves, $H_i(\vec{\omega})$ corresponding to the ct-ranges previous defined. The ct segmentation is chosen in order to have, on average, about the same number of events per bin (≈ 50) in each of the $H_i(\vec{\omega})$ histogram, as in case of the initial no-ct-binned angular acceptance; for this reason, since the flat MC is made of about 440000 events, the three-dimensional histograms are built with $12 \times 12 \times 12$ bins.

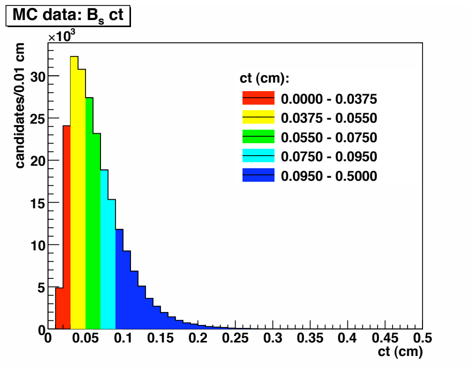

Figure 35: ct distribution of real MC data sample. The five ct slices are represented with different colors: in red 0.0 cm $\leq ct <$ 0.0375 cm, in yellow 0.0375 cm $< ct <$ 0.055 cm, in green 0.055 cm $\leq ct <$ 0.075 cm, in light blue 0.075 cm $\leq ct <$ 0.095 cm, and in blue 0.095 cm $< ct <$ 0.50 cm.

- We fit each set of events, using the proper $H_i(\vec{\omega})$ acceptance in the angular pdf.

The results are listed in tab. 18. The estimates found are in agreement for each sets. The seventh column of the table reports the averaged values of the five fits, and the last one shows the estimates of the fit to the entire samples (Sect. 7.7).

Parameter	slice 1	slice 2	slice 3	slice 4	slice 5	Averaged value	Entire sample
$\|A_0\|^2$	0.3325(26)	0.3269(26)	0.3261(28)	0.3284(35)	0.3227(32)	0.3276(13)	0.3276(13)
$\|A_\parallel\|^2$	0.3304(28)	0.3369(28)	0.3387(30)	0.3311(37)	0.3346(32)	0.3345(14)	0.3344(14)
$\delta_\parallel$ [rad]	1.569(10)	1.555(10)	1.562(11)	1.574(14)	1.580(12)	1.5667(51)	1.5667(51)

Table 18: Fit on five sets of ct ranges of realistic MC.

9 Systematic Uncertainties

In the following we evaluate the main systematic sources. The systematic uncertainty for the ML fit is meant to cover the effects which may have not been properly incorporated in our model and could precisely lead to systematic biases on the estimates. These uncertainties are mostly evaluated using pseudo-experiments technique: we consider the systematic effects by simulating experiments with a different parameterization which simulates the effect we want to account for, while using the default model for fitting (without the "new" effect).

We produce a set of reference pseudo-experiments, with no systematic variations. Then, for each systematic effect, the magnitude of a systematics for a parameter ξ is evaluated from the difference between the averaged shift from the input value for the pseudo-experiments with and without the systematic effect generated:

$$\mathrm{syst}_\xi = \mathrm{shift}_\xi^{(\mathrm{with})} - \mathrm{shift}_\xi^{(\mathrm{without})} \tag{30}$$

where

$$\mathrm{shift}_\xi^{(i)} =< \xi^{(\mathrm{fitted})} > - \xi^{(\mathrm{input})} \tag{31}$$

In the pseudo-experiments, both signal and background components are present and the input parameters are the estimates of the fit on real data. We run 3000 pseudo-experiments made of 480 events for each systematic estimation (and for the reference model too). The reference pseudo-experiments gives the following value

Parameter	Mean	σ	shift
$\lvert A_0\rvert^2$	0.005± 0.019	1.002±0.014	0.0002
$\lvert A_\parallel\rvert^2$	-0.037± 0.020	1.044±0.014	-0.0008
$\cos\delta_\parallel$	-0.002± 0.022	1.140±0.016	-0.030
$\lvert A_\perp\rvert^2$			0.0007

9.1 Residual discrepancy Data-MC

In Sect. 6 we mention the MC validation performed in the branching ratio analysis [3]. We see a small discrepancy between the data and MC $p_{\mathrm{T}}(B)$ distribution in the MC validation. Then, we find a reweighing function (see [3]) and we reweigh the 3D histogram of angular signal acceptance in the final fit (see fig. 36). We want to know how this changes the fit estimates.

We generate the pseudo-experiments using the not-reweighed acceptance histogram, and we fit these pseudo-experiments using the reweighed acceptance histogram. Then we look at the difference between the input value and the averaged fitted value for each polarization parameters.

Parameter	Mean	σ	Systematic
$\lvert A_0\rvert^2$	-0.073± 0.020	1.043±0.014	-0.003
$\lvert A_\parallel\rvert^2$	-0.014± 0.020	1.046±0.014	0.001
$\cos\delta_\parallel$	-0.002± 0.023	1.159±0.016	-0.007
$\lvert A_\perp\rvert^2$			0.002

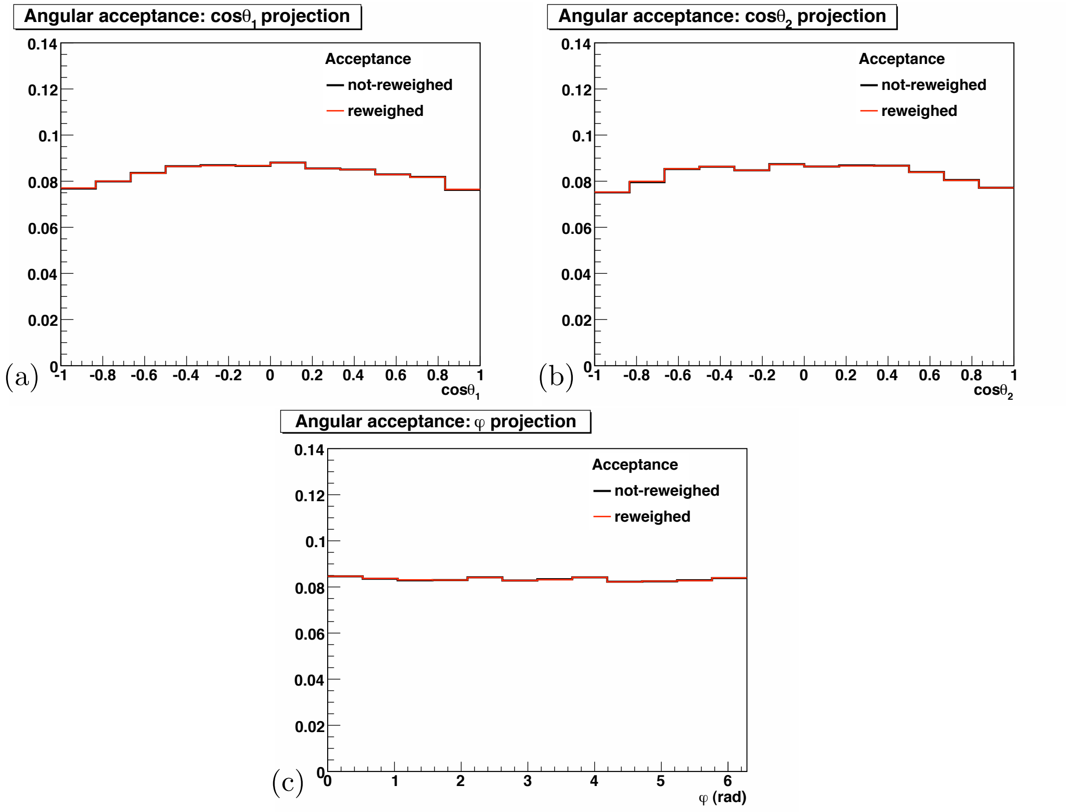

Figure 36: Detector angular acceptance projections: comparison of re-weighted and not re-weighted histograms. $\cos\vartheta_1$ (a), $\cos\vartheta_2$ (b) and Φ (c).

9.2 Binning of angular acceptance histogram

Since the signal angular acceptance is taken from a 3D PHSP MC histogram, we want to know if there is a dependence of the fit estimates on its binning. We generate pseudo-experiments using an acceptance histogram with $20\times20\times20$ ($\cos\vartheta_1\times\Phi\times\cos\vartheta_2$) bins, and we fit these pseudo-experiments using the same acceptance histogram with $31\times7\times31$ bins.

Parameter	Mean	σ	Systematic
$\lvert A_0\rvert^2$	0.028±0.020	1.016±0.014	0.001
$\lvert A_\parallel\rvert^2$	-0.073±0.020	1.050±0.014	-0.001
$\cos\delta_\parallel$	0.28±0.022	1.117±0.015	0.004
$\lvert A_\perp\rvert^2$			0.000

9.3 Angular acceptance model (Trigger-Paths division)

In our fit, we fill the angular acceptance histogram with the events coming from the sum of the three exclusive trigger-paths data set. We want to find if any potential bias is introduced by the trigger differences in the angular acceptance model. Thus, we build the signal angular acceptance taking the sum of the histograms of each trigger-paths samples weighted by the appropriate trigger-paths fractions (see tab. 2). We generate pseudo-experiments with this signal angular acceptance histogram and then we fit these pseudo-experiments using the default signal angular acceptance, which do not take into account the trigger-path re-weight.

Parameter	Mean	σ	Systematic
$\|A_0\|^2$	-0.073±0.020	1.043±0.014	0.005
$\|A_\parallel\|^2$	-0.014 ±0.020	1.046±0.014	-0.002
$\cos\delta_\parallel$	-0.002±0.023	1.159±0.016	0.005
$\|A_\perp\|^2$			-0.003

9.4 Angular background model

We observe a good agreement between the data in the sideband mass regions and the angular background model, but we cannot exactly know if we used a too simple or too complex models. Thus, we will test it fitting pseudo-experiments where the angular background is generated with the angular background events randomly taken from the side-bands region. Then we fit these pseudo-experiments using the default background model.

Parameter	Mean	σ	Systematic
$\|A_0\|^2$	-0.002±0.020	1.016±0.014	-0.001
$\|A_\parallel\|^2$	-0.093 ±0.020	1.053±0.014	-0.001
$\cos\delta_\parallel$	-0.004 ±0.022	1.108±0.015	-0.009
$\|A_\perp\|^2$			0.002

9.5 Reflection background component

In our fit we do not include the $B_d^0 \to \phi K^\star$ reflection component. Anyway, we already know its fraction in our data sample from the branching ratio analysis (see Sect. 5.3). We want to evaluate the impact of such an effect on the polarization estimates. We generate pseudo-experiments with the reflection component in the background model. The mass background events are generated using the usual exponential decreasing distribution plus another asymmetric distribution representing the reflection signal (see [3]); the angular reflection background events are randomly taken from the 3D helicity angular histogram of the $B_d^0 \to \phi K^\star$ MC, whose polarization amplitudes and phases are fixed to the PDG values; in tab. 19 the polarization amplitudes for the $B_d^0 \to \phi K^\star$ are compared with the ones we measure for $B_s^0\to\phi\phi$.

	$\|A_0\|^2$	$\|A_\parallel\|^2$	$\|A_\perp\|^2$	$\cos\delta_\parallel$
$B_d \to \phi K^\star$	0.484 ± 0.033	0.26 ± 0.04	0.26 ± 0.04	-0.69 ± 0.10
$B_s^0\to\phi\phi$	0.348 ± 0.041	0.287 ± 0.043	0.365 ± 0.044	$-0.91\ ^{+0.15}_{-0.13}$

Table 19: $B_d^0 \to \phi K^\star$ polarization parameters.

In fig. 37 there are the helicity angular distributions of the MC histogram used in the generation (red line), which is compared with the distribution of the events generated in the pseudo-experiments. The fraction of reflection component is taken from the BR analysis (about 3% of the signal component). Then we fit these pseudo-experiments using the background model without this

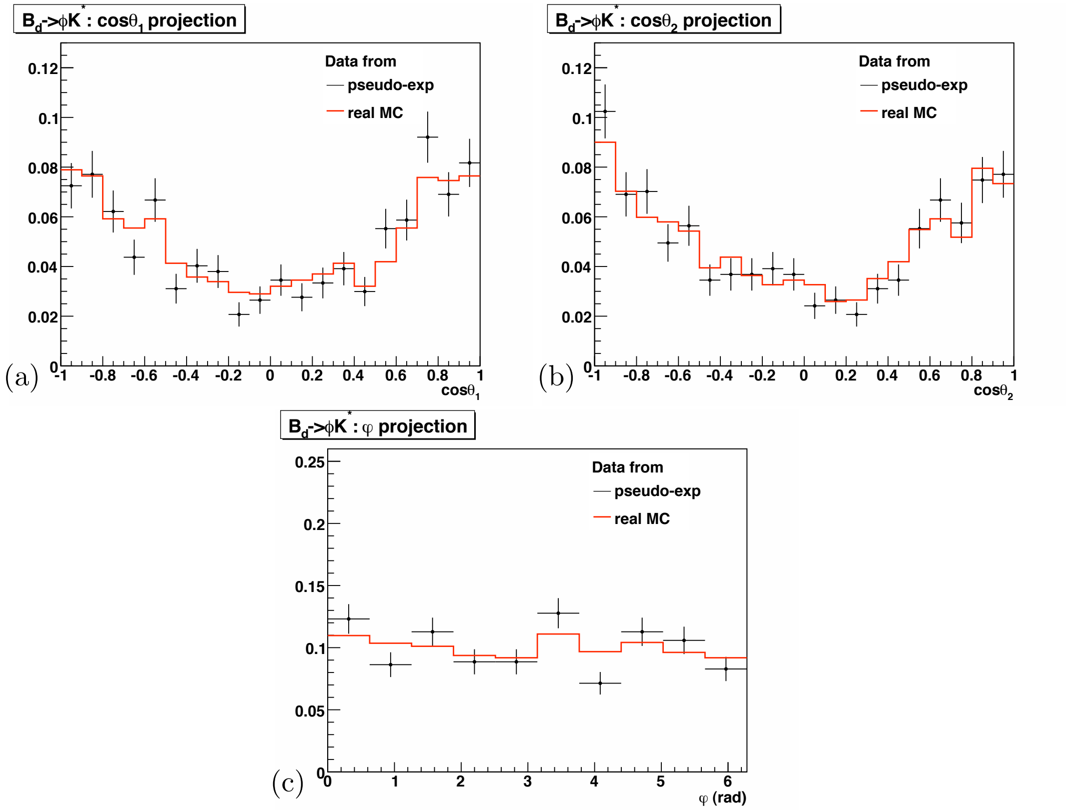

Figure 37: $B_d^0 \rightarrow \phi K^\star$: helicity angular distributions of the MC histogram used in the generation (red line), and the distribution of the events generated in one of the pseudo-experiments. $\cos\vartheta_1$ (a), $\cos\vartheta_2$ (b) and $\varPhi$ (c).

reflection component. We look at the difference between the input value and the averaged fitted value for each polarization parameters.

Parameter	Mean	σ	Systematic
$\lvert A_0\rvert^2$	0.191±0.020	1.037±0.014	0.008
$\lvert A_\parallel\rvert^2$	-0.083±0.020	1.049±0.014	-0.002
$\cos\delta_\parallel$	0.150±0.022	1.101±0.015	0.019
$\lvert A_\perp\rvert^2$			-0.006

9.6 *ct*-dependence of angular acceptance

We want to estimate the impact on the fit estimates of the detector angular acceptance dependence on *ct*. We proceed as follow:

- we generate pseudo-experiments where the angular acceptance is divided in 5 *ct*-slices (for each *ct* bin, the proper 3D angular histogram is built, as we described in Sect. 8.3);
- the *ct* of the event is randomly taken from the corresponding MC histogram distribution;
- given the *ct*, the event helicity angles are selected by the proper angular acceptance.

These pseudo-experiment are fitted using the total angular acceptance (not divided in ct-slices) in the signal model.

Parameter	Mean	σ	Systematic
$\lvert A_0\rvert^2$	0.015±0.020	1.033 ±0.014	0.000
$\lvert A_\parallel\rvert^2$	-0.001±0.020	1.039±0.014	0.001
$\cos\delta_\parallel$	0.037±0.022	1.123±0.015	-0.001
$\lvert A_\perp\rvert^2$			0.004

9.7 Satellite Peak

We want to estimate the effect of potential reflections or other peaking background that might be hiding on the low mass side of the signal peak. In the branching ratio analysis we have shown that the change in the central value for the $B_s^0 \to \phi\phi$ yield by varying the fit range or by introducing a peaking background component of the same shape as the signal and peaked at the B_d mass is the same. Anyway, the little bump on the left side-band of the invariant mass distribution may suggest the presence of some physics background, like the $B_d \to \phi\phi$ decay. Only the limit of the BR for this decay is known, which is $BR < 2 \times 10^{-7}$ (CL=90%). This is a very low value and if we assume the efficiency ratio for the $B_d \to \phi\phi$ to be the same for the B_s, considering the ratio $f_s/f_d \simeq 1/4$, we would expect about ten signal events in our sample.

Thus, we implement a fit where a resonant component at the mass of the B_d is given the same mass shape as the signal and whose polarization are fitted floating the polarization fraction ($|A_0^{(B_d)}|^2$, $|A_\parallel^{(B_d)}|^2$ and $\delta_\parallel^{(B_d)}$) and satellite peak fraction f_{B_d} of events. The results of this fit are shown in table 20 and the projections in fig. 38

Parameter	Fit value
M [GeV/c^2]	5.3636 ± 0.0012
σ [GeV/c^2]	0.0167 ± 0.0011
f_{b}	0.371 ± 0.030
b [c^2/GeV]	2.05 ± 0.77
$\lvert A_0\rvert^2$	0.344 ± 0.041
$\lvert A_\parallel\rvert^2$	0.287 ± 0.043
$\cos\delta_\parallel$	$-0.891^{+0.15}_{-0.13}$
B	$0.85^{+0.46}_{-0.37}$
f_{B_d}	0.79 ± 0.47
$\lvert A_0^{(B_d)}\rvert^2$	0.001 ± 0.066
$\lvert A_0^{(B_d)}\rvert^2$	0.670 ± 0.308
$\delta_\parallel^{(B_d)}$	3.1 ± 4.4

Table 20: Results of the fit with $B_d \to \phi\phi$ component.

The satellite peak contains 15 ± 8 and is not very significant (2.5 sigma statistical only from the difference in the likelihood). The number of signal events increases by 4 events (from 293). We compare result for the standard fit and this one to assign a systematic uncertainty due to a possible resonant contribution below the signal mass peak that we ignore:

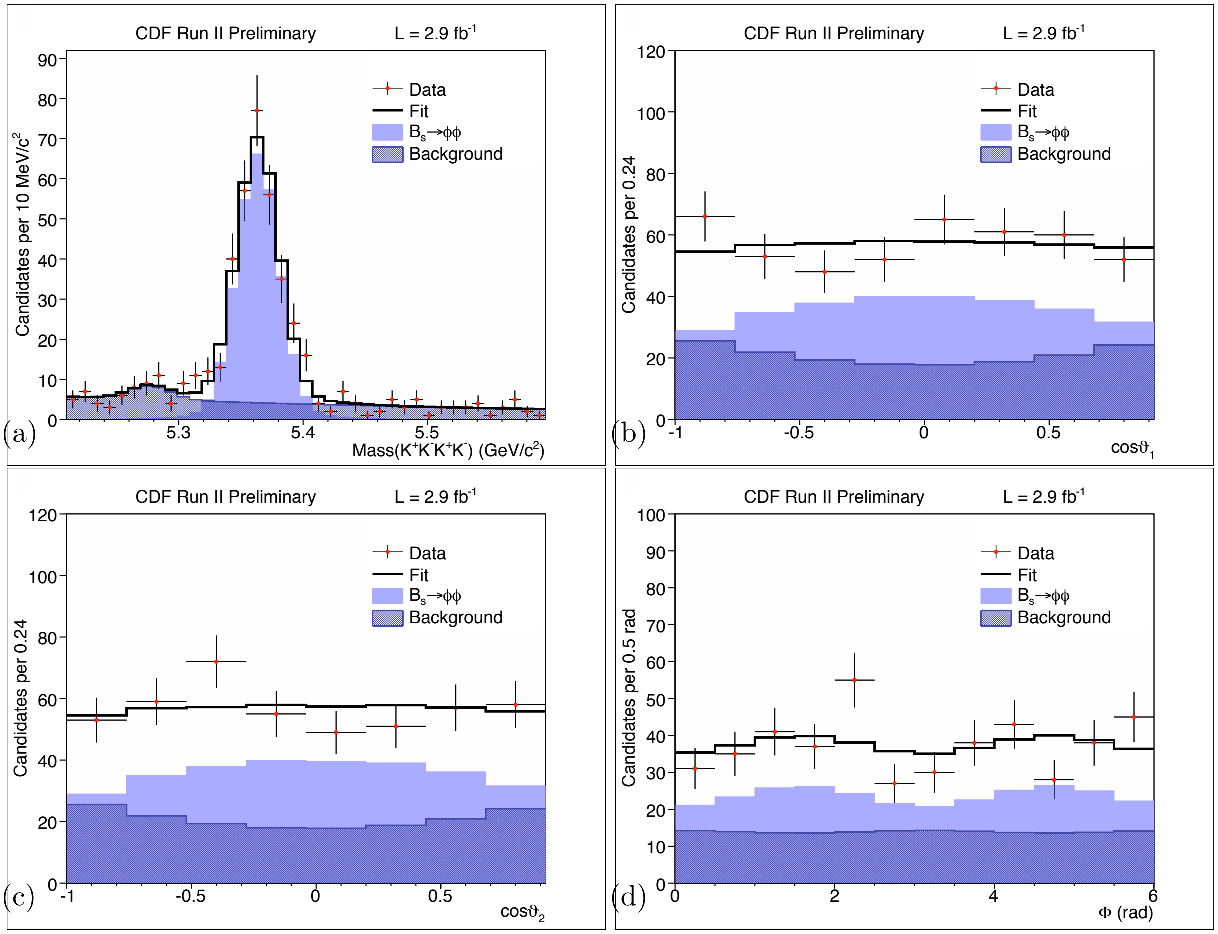

Figure 38: Projections of the time-integrated fit with $B_d \to \phi\phi$ component: mass (a), $\cos\vartheta_1$ (b), $\cos\vartheta_2$ (c), and Φ (d).

	$\lvert A_0\rvert^2$	$\lvert A_\parallel\rvert^2$	$\lvert A_\perp\rvert^2$	$\cos\delta_\parallel$
with $B_d \to \phi\phi$	0.344 ± 0.041	0.287 ± 0.043	0.369 ± 0.044	$-0.89^{+0.15}_{-0.13}$
default	0.348 ± 0.041	0.287 ± 0.043	0.365 ± 0.044	$-0.91^{+0.15}_{-0.13}$
syst	-0.004	0.000	0.004	-0.02

We see that the systematic uncertainty is very tiny since the two “signals” do not really overlap in mass. The previously assigned systematic, obtained by changed the fit B_s mass window (analogous to what done in the BR analysis), was slightly bigger (0.007 and 0.003 respectively for $|A_0|^2$ and $|A_\parallel|^2$)

9.8 Non-resonant contribution

It is possible that there a small S-wave (scalar) contribution to the angular distribution, due to non-resonant components under the ϕ peak signal, or a resonant contribution such as a $f_0\phi$ final state.

To compute this effect, one has first to estimate the fraction of these events in our data sample. Then, one can model with the MC technique the contribution of this scalar component into the angular distribution. Thus, the usually pseudo-experiments procedure allows one to compute the order of the systematic uncertainty of such an effect.

In fig. 39 the mass distribution of the reconstructed ϕ meson after the off-line selection is presented. A fit is performed with the convolution of a Breit-Wigner function (resonance) and a Gaussian function (experimental resolution). The width of the Breit-Wigner function is fixed from the PDG value ($4.26 \pm 4\,\mathrm{MeV}/c^2$). The fit has a very good χ^2 and we thus argue that there is little room for non-resonant signal components under the ϕ peak signal.

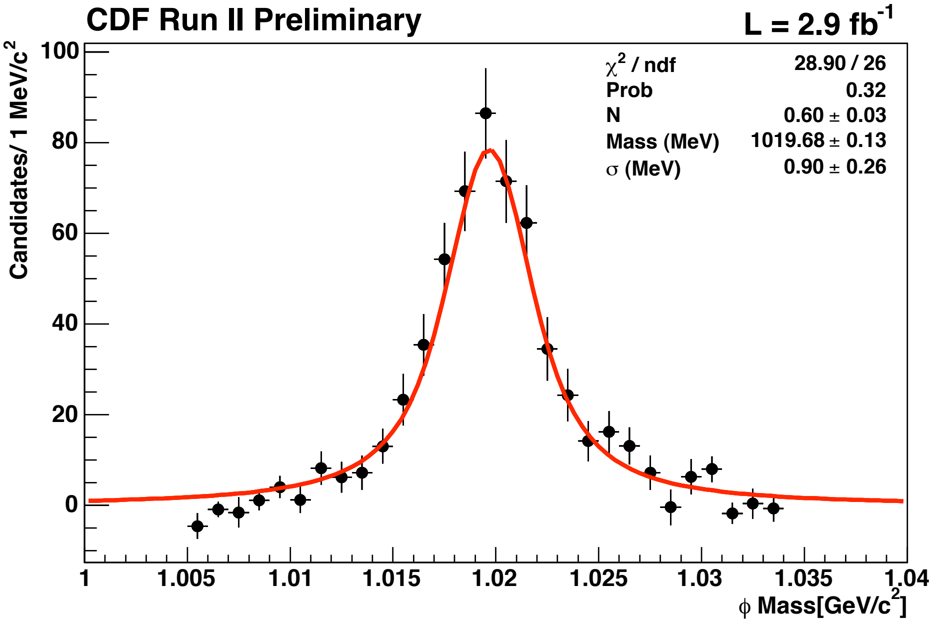

Figure 39: Reconstructed ϕ mass after off-line selection. The black points are side-bands subtracted data; the red line is the fit performed with the convolution of a Breit-Wigner function (resonance) and a Gaussian function (experimental resolution). The σ parameter is the Gaussian resolution width. M is is the central mass value; N is a normalization factor.

Anyway, we decided to generate MC for two possible S-wave contribution that might leak under our signal:

1. B_s to ϕ and a non resonant pair of Kaons ($B_s \to \phi(K^+K^-)$);

2. B_s to ϕ and an f_0 which in turn decays into the K^+K^- channel ($B_s \to \phi f_0$).

The two MC are subject to the standard procedure for MC generation production and analysis. The $B_s \to \phi(K^+K^-)$ is generated according to the phase space decay model, the $B_s \to \phi f_0$ according to the SVS decay model in EvtGen (Scalar to Vector+Scalar, which has no parameters, since the kinematics is fixed by angular momentum conservation); 2×10^6 events were generated for each decay, of these only 36 survive for $B_s \to \phi(K^+K^-)$ and 6371 for the $B_s \to \phi f_0$.

To normalize these contribution to the $B_s^0 \to \phi\phi$ signal we use the following analogy to B_d case:

1. we take the ratio
$$\frac{BR(B_s \to \phi(K^+K^-))}{BR(B_s \to \phi\phi)} = 3 \tag{32}$$
based on PDG2009 estimate of
$$\begin{aligned}\frac{BR(B_d \to K^\star(K^+K^-))}{BR(B_d \to K^\star\phi)} &= \frac{27.5 \pm 2.6}{9.8 \pm 0.6} = 2.8 \pm 0.3\\ \frac{BR(B_d \to K^0(K^+K^-))}{BR(B_d \to K^0\phi)} &= \frac{24.7 \pm 2.3}{8.6 \pm 1.3} = 2.9 \pm 0.5\end{aligned} \tag{33}$$
Notice that this is a conservative choice since the actual non-resonant to resonant ratio is a factor 2 rather than 3.

2. we consider
$$BR(B_s \to \phi f_0)BR(f_0 \to K^+K^-) \simeq BR(B_d \to f_0 K^\star)BR(f_0 \to K^+K^-) \tag{34}$$
From a BaBar analysis (arxiv:0808.3586) we read that they find in a window $0.99 < M(K^+K^-) < 1.05$ GeV/c^2 (thus twice as big as ours) 84 ± 19 eventi consistent with an f_0 in a total 535 eventi of the type $B_d \to \phi K^\star$. Thus,
$$\frac{BR(B_d \to f_0 K^\star)BR(f_0 \to K^+K^-)}{BR(B_d \to \phi K^\star)BR(\phi \to K^+K^-)} = \frac{84 \pm 19}{535} = 0.16 \pm 0.04 \tag{35}$$
and using $BR(\phi \to K^+K^-) = 0.492$,
$$\frac{BR(B_d \to f_0 K^\star)BR(f_0 \to K^+K^-)}{BR(B_d \to \phi K^\star)} = 0.08 \pm 0.02 \tag{36}$$
Notice that this is a conservative estimate since the BaBar mass window is much bigger than what we use in our analysis. This should well cover the uncertainty in the modelization of the f_0 resonance shape in the EvtGen simulation.

Following the above assumption we derive that the possible contribution of these backgrounds in our sample is

- 0.9 % of the signal yield for the $B_s \to \phi(K^+K^-)$;
- 4.6% of the signal yield for the $B_s \to \phi f_0$.

To estimate the effect on our measurement of this background we generate toys where these contributions are added in the above proportion to the standard signal+background pseudo-experiments and fitted without taking into account these contribution. The full difference is quoted as a systematics for "S-wave and non-resonant contributions".

Parameter	Mean	σ	Systematic
$\|A_0\|^2$	0.180±0.020	1.027±0.014	0.013
$\|A_\parallel\|^2$	-0.051±0.020	1.054±0.014	-0.003
$\cos\delta_\parallel$	0.275±0.022	1.077±0.015	0.084
$\|A_\perp\|^2$			-0.010

9.9 Dependence of the Angular Acceptance on $\Delta\Gamma_s$

As shown in Sec. 3.1 (eq. 4) if the B_s mixing phase (ϕ_s) is absent the A_0 and $A_\parallel$ components (and their interference) evolve in time with an exponential with $\Gamma = \Gamma_L$ while the $A_\perp$ compoent evolve with $\Gamma = \Gamma_H$. If the width difference $\Delta\Gamma_s = \Gamma_L - \Gamma_H$ is sizable (as expected and verified experimentally) a significant bias on the polarization at t=0 (the physical observable) is expected when performing a time integrated measurement. Assuming world average value for Γ_H and Γ_L we can compensate to first order the effect coming purely from the normalization of the decay rate (eq. 4). The related experimental uncertainty is propagated to the measured $B_s^0 \to \phi\phi$ polarization and is discussed in the following subsection. What we need to consider further here is the effect induced by a non uniform acceptace with the B_s^0 decay proper time introduced by the two track trigger.

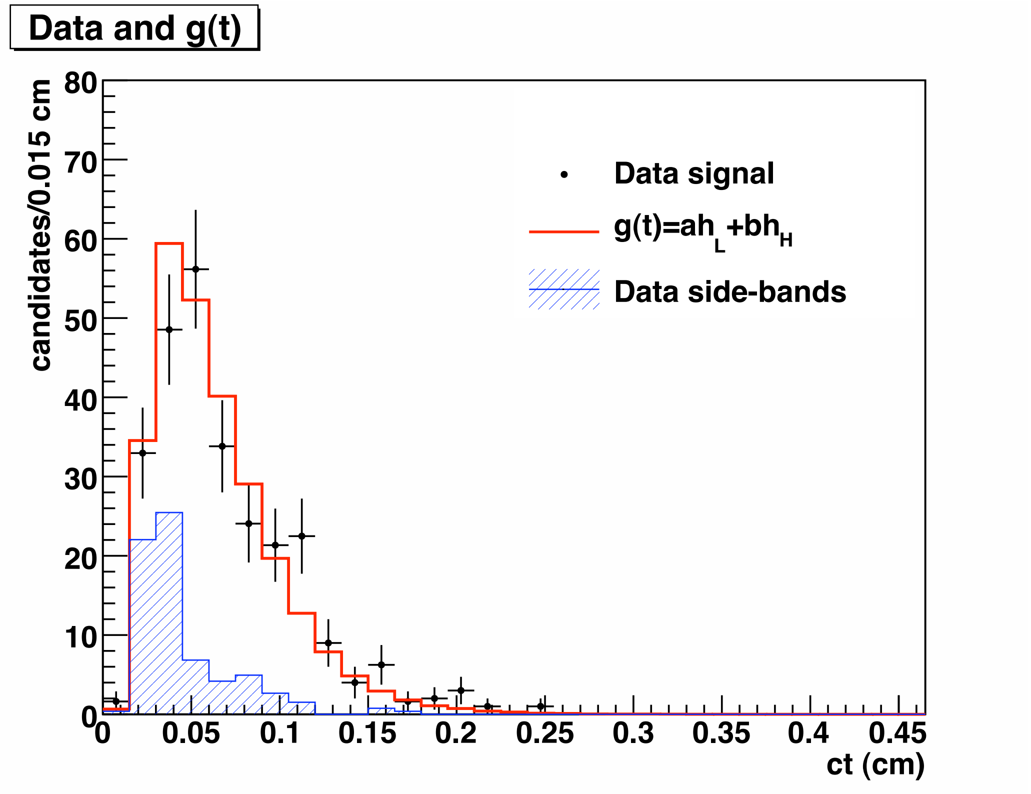

Figure 40: Reconstructed proper time ct for sideband subtracted signal compared with MC expectation

The realistic MC reproduces the ct acceptance of the trigger and selection reasonably well for the purpose we are interested here, see e.g.Fig. 40. We thus generated different samples each with polarization in accordance with fitted values, but different lifetimes for the CP-even and CP-odd components:

1. DG0a: uses `SVV_HELAMP` with the polarization and phase as in the default fit. This sample is generated with a decay file reproduced in Appendix F.
2. DG0b: uses the mechanism described in Sec. 6 and F with independent `SVV_HELAMP` samples

with $2 \cdot 10^6$ and $1.154 \cdot 10^6$ events generated respectively corresponding to the 63.4% CP-even component found in our data. For this sample the same lifetime is used for both components.

3. DG1: as above but uses different lifetimes for the two components. The average B_s^0 width in the default EvtGen tables is 0.686 ps^{-1} (1.458 ps). To the average width we add up or subtract half the world average [48] width difference $\Delta\Gamma_s/2 = 0.062/2 = 0.031$ ps^{-1} to obtain $\Gamma_L = 0.717$ ps^{-1} ($\tau_L = 1.394$ ps) and $\Gamma_H = 0.654$ ps^{-1} ($\tau_L = 1.528$ ps).

4. DG1up: as above but we use a $\Delta\Gamma_s = 0.101$ ps^{-1} corresponding to the world average $\Delta\Gamma_s$+1σ. This translaes in $\Gamma_L = 0.736$ ps^{-1} ($\tau_L = 1.358$ ps) and $\Gamma_H = 0.635$ ps^{-1} ($\tau_L = 1.574$ ps).

	L2 Trigger selection			Final selection		
Sample	Even	Odd	Even Fraction	Even	Odd	Even Fraction
DG0b	94822	59865	61.3 %	21169	13722	60.7 %
DG1	92646	61553	60.1 %	20748	14160	59.4 %
DG1up	90716	62442	59.2 %	20290	14267	58.7 %

Table 21: Number of Monte Carlo events surving trigger and final selection.

Number of events surviving after trigger selection in MC and after reconstruction and selection are collected in Table 21. We first notice that even if generated with 0 lifetime difference the odd and even sample have a significant difference in their respective trigger and selection efficiency. In fact the input CP-even fraction of 63.4% is reduced to only 60.7% after selection. This is a purely kinematic effect induced by the differene in the angular correlation between decay products in the L=1 (CP-odd) state with respect to L=0 and L=2 states. This large difference is completely corrected by the angular acceptance correction in the fit as can be seen comparing the result of fits to the DG0a and DG0b samples in Table 22 with that in the actual data. The effect of $\Delta\Gamma_s = 0.10$ ps^{-1} ($\Delta\Gamma_s/\Gamma_s$ 0.15) is, in comparison minor (further reducing the CP-even fraction by 2% compared to the 3 % of pure angular acceptance. From the fit to the DG1 and DG1up sample we see that we are actually over-compensating the CP-even fraction if we don't perform any further correction besides that related to the normalization. Since for $\Delta\Gamma_s$ within the SM (and experimental) range the effect are of the order 1% on $|A_0|^2$ and 0.5% for $|A_{||}|^2$ we decided to treat this as a systematic rather than to calculate a correction and assign a systematic uncertainty on the polarization observables from the difference in the fit result of the DG1up and DG0b samples.

Sample	$\lvert A_0\rvert^2$	$\lvert A_{\parallel}\rvert^2$	Even Fraction
DATA	0.347 ± 0.041	0.287 ± 0.043	63.4 %
DG0a	0.3491 ± 0.0041	0.2860 ± 0.0041	63.51 %
DG0b	0.3521 ± 0.0032	0.2837 ± 0.0033	63.58 %
DG1	0.3585 ± 0.0033	0.2861 ± 0.0033	64.46 %
DG1up	0.3596 ± 0.0033	0.2917 ± 0.0034	65.13 %

Table 22: Result of fit to MC samples with specific polarization and lifetime differences.

We additionally (and conservatively) add in quadrature the difference in the polarization observables from the input value (DATA) to the one obtained in the DG0b sample covering possible fit bias observed in these mixed MC samples. The systematic uncertainty due to the dependence of the angular acceptance on $\Delta\Gamma_s$ is then: 0.009 for $|A_0|^2$, 0.009 for $|A_\parallel|^2$, 0.016 for $|A_\perp|^2$ and 0.011 for $\cos\delta_\parallel$.

9.10 τ_{L} and τ_{H} uncertainties

With the time-integration of the differential decay rate, actually, the parameters that enters the fit angular model are $\tau_{\mathrm{L}}|A_0|^2$, $\tau_{\mathrm{L}}|A_\parallel|^2$ and $\tau_{\mathrm{H}}|A_\perp|^2$. Then we have to propagate the $\tau_{\mathrm{L(H)}}$ uncertainties to the polarization amplitudes. Since we don't know the correlation among the $\tau_{\mathrm{L(H)}}$ measurements, we compute the four combination

case	$\|A_0\|^2$ syst	$\|A_\parallel\|^2$ syst	$\|A_\perp\|^2$ syst
$\tau_{\mathrm{L}}+\sigma_{\mathrm{L}}$ and $\tau_{\mathrm{H}}+\sigma_{\mathrm{H}}$	±0.0080	±0.0063	±0.0152
$\tau_{\mathrm{L}}-\sigma_{\mathrm{L}}$ and $\tau_{\mathrm{H}}+\sigma_{\mathrm{H}}$	±0.0076	±0.0060	±0.0150
$\tau_{\mathrm{L}}+\sigma_{\mathrm{L}}$ and $\tau_{\mathrm{H}}-\sigma_{\mathrm{H}}$	±0.0080	±0.0063	±0.0166
$\tau_{\mathrm{L}}-\sigma_{\mathrm{L}}$ and $\tau_{\mathrm{H}}-\sigma_{\mathrm{H}}$	±0.0076	±0.0060	±0.0164

and we consider as the systematic the worst case ($\tau_{\mathrm{L}}+\sigma_{\mathrm{L}}$ and $\tau_{\mathrm{H}}-\sigma_{\mathrm{H}}$).

9.11 CP-violation dependence

In our fit we assume to be in the SM, thus, we fix the CP-violation $\phi_{\mathrm{s}}=0$. One may want to know how this assumptions affect the fit estimates. Thus, we make some sets of pseudo-experiments fixing $\phi_{\mathrm{s}}\neq 0$. We introduce in the angular model the terms regarding CP-violation, which involve the strong phase $\delta_\perp$ too. Then, we fit with the default model with $\phi_{\mathrm{s}}=0$.

ϕ_{s}	$\delta_\perp$	$\|A_0\|^2$ syst	$\|A_\parallel\|^2$ syst	$\|A_\perp\|^2$ syst	$\cos\delta_\parallel$ syst
-0.44	0	0.001	0.001	-0.002	-0.004
-0.44	1.57	0.001	0.000	-0.001	0.007
-0.44	2.47	0.000	-0.001	0.001	0.001
-0.68	2.47	0.002	0.001	0.003	-0.009

We consider as the systematic the worst case ($\phi_{\mathrm{s}}=-0.68$ and $\delta_\perp=2.47$).

9.12 Systematic Summary

We summarize the systematic uncertainties in the following table

	$\lvert A_0\rvert^2$ syst	$\lvert A_\parallel\rvert^2$ syst	$\lvert A_\perp\rvert^2$ syst	$\cos\delta_\parallel$ syst
MC reweight	±0.003	±0.001	±0.002	±0.007
Acceptance binning	±0.001	±0.001	±0.000	±0.004
Acceptance Model	±0.005	±0.002	±0.003	±0.005
Background Model	±0.001	±0.001	±0.002	±0.009
Acceptance *ct*-dependence	±0.000	±0.001	±0.001	±0.004
Reflection component	±0.008	±0.002	±0.006	±0.019
Non-resonant contribution	±0.013	±0.003	±0.010	±0.084
Satellite peak	±0.004	±0.000	±0.004	±0.020
Acceptance $\Delta\Gamma$-dependence	±0.009	±0.009	±0.016	±0.011
$\tau_{\mathrm{L(H)}}$ uncertainties	±0.008	±0.006	±0.017	
total	±0.021	±0.011	±0.027	±0.089

If we want to consider also the CP-violation effects, we obtain

	$\lvert A_0\rvert^2$ syst	$\lvert A_\parallel\rvert^2$ syst	$\lvert A_\parallel\rvert^2$ syst	$\cos\delta_\parallel$ syst
CP-violation	±0.002	±0.001	±0.003	±0.009
total	±0.021	±0.011	±0.027	±0.090

10 Conclusions

We have presented the first measurement of the polarization amplitudes for the charmless $B_s^0 \to \phi\phi \to [K^+K^-][K^+K^-]$ decay of the B_s^0 meson. The result is achieved using an unbinned Maximum Likelihood fit to the data collected by the CDFII detector, in a period starting from March 2001 till April 2008, which corresponds to an integrated luminosity of 2.9 fb^{-1}.

In the analysis we don't distinguish between B_s^0 and $\bar{B}_s^0$ at the production time (*untagged* analysis) and we assume the B_s^0 mixing phase $\phi_\mathrm{s} = 0$ because in the SM its value is very small. The final fit takes into account the time evolution of the angular decay rate in terms of the B_s^0 Light and Heavy mass eigenstates evolutions, but their two mean time lives, τ_L and τ_H, are taken as external parameters and they are fixed to the latest PDG values.

The fit results for the polarization amplitudes and their systematics uncertainties are:

$$\begin{array}{ll}
|A_0|^2 & = 0.348 \pm 0.041(\mathrm{stat}) \pm 0.021(\mathrm{syst}) \\
|A_\parallel|^2 & = 0.287 \pm 0.043(\mathrm{stat}) \pm 0.011(\mathrm{syst}) \\
|A_\perp|^2 & = 0.365 \pm 0.044(\mathrm{stat}) \pm 0.027(\mathrm{syst}) \\
\cos\delta_\parallel & = -0.91^{+0.15(\mathrm{stat})+0.09(\mathrm{syst})}_{-0.13(\mathrm{stat})-0.09(\mathrm{syst})}
\end{array}$$

and the resulting polarization fractions are:

longitudinal (f_L)	transverse (f_T)
$0.348 \pm 0.041(\mathrm{stat}) \pm 0.021(\mathrm{syst})$	$0.652 \pm 0.041(\mathrm{stat}) \pm 0.021(\mathrm{syst})$

10.1 Perspectives

As of this writing, 7 fb^{-1} of data is already delivered, and at the end of the next year an integrated luminosity of about 10 fb^{-1} is expected. Thus, it is possible to extend the analysis to a greater data sample in order to minimize the statistical uncertainties. A rough calculation, which doesn't take into account the prescaling of the different triggers with the instantaneous luminosity, shows that the reachable resolutions σ on the polarization amplitudes is:

$$\sigma = 0.04\sqrt{\frac{2.9}{10}} \approx 0.02 \tag{37}$$

Hence, we could expect a factor 1/2 of the current statistical uncertainty for the analysis in 10 fb^{-1} of data.

Moreover, the extension of the analysis beyond 2.9 fb^{-1} of data would allows us to measure the two mean live times τ_L and τ_H. Actually, not much more statistics with respect to the ones in ours sample are probably needed to perform a time-dependent fit aimed at the Γ_L and Γ_H estimation.

10.2 Theoretical Considerations on the Results

From our measurement we can draw the following considerations:

1. the amplitude hierarchy $|A_0| \gg |A_\parallel| \simeq |A_\perp|$ of the SM is not satisfied in the $B_s \to \phi\phi$ decay, being $|A_0| \simeq |A_\perp| \gtrsim |A_\parallel|$;

2. the longitudinal polarization fraction is less than the transverse one, in contrast with
   - the SM expectation, that predicts a dominant longitudinal fraction with the transversely-polarized amplitudes suppressed by a factor m_ϕ/m_{B_s};
   - the decay amplitudes for $B \to \phi K^\star$, a $\bar{b} \to \bar{s}$ penguin transition like the $B_s \to \phi\phi$, measured by the BaBar and the Belle experiments [19, 40, 41], which result in a transverse polarization about equal to the longitudinal one, being $f_{\rm L} = 0.50 \pm 0.05$ for the $B^+ \to \phi K^{\star +}$ decay, and $f_{\rm L} = 0.484 \pm 0.033$ for the $B^0 \to \phi K^{\star 0}$ decay.

We compare our results with the theoretical predictions of the various approaches adopted in the calculation of the polarization amplitudes. They are reported in tab. 23. We find that our central values are consistent within the uncertainty ranges with the expectations of the QCD factorization 1.a. and 1.b in [24], while they are not with the expectation of perturbative QCD [32]. The approach adopted in [24] justifies the violation of the amplitudes hierarchy and the large transverse polarization fraction with the penguin weak-annihilation effects, because the penguin annihilation plays a more significant role for the transverse polarization amplitudes than for the longitudinal polarization ones.

	$f_{\rm L}$ [%]	$f_{\rm T}$ [%]
Our experimental result	$0.348 \pm 0.041({\rm stat}) \pm 0.021({\rm syst})$	$0.652 \pm 0.041({\rm stat}) \pm 0.021({\rm syst})$
QCD factorization 1.a	43^{+0+61}_{-0-34}	57^{+0+61}_{-0-34}
QCD factorization 1.b	48^{+0+26}_{-0-27}	52^{+0+26}_{-0-27}
QCD factorization 2	86.6	13.4
Naive factorization	88.3	11.7
NLO EWP 1	86.3	13.7
NLO EWP 2	86.3	13.7
perturbative QCD	$61.9^{+3.6+2.5+0.0}_{-3.2-3.3-0.0}$	$38.1^{+3.6+2.5+0.0}_{-3.2-3.3-0.0}$

Table 23: Comparison of our experimental results with the theoretical predictions. The references are: [24] for QCD factorization 1.a and 1.b, [30] for QCD factorization 2 and Naive factorization, [31] for NLO EWP 1 and 2, [32] for perturbative QCD.

In fact, in this model the penguin weak annihilation:

- gives small contribution to the longitudinal penguin amplitude;
- can (but do not need to) give large contribution to the transverse polarisation in penguin-dominated decays;
- doesn't give such an enhancement to the tree amplitudes, hence tree-dominated decays should be predominantly longitudinally polarized, as it was observed for the tree-level $b \to u$ transition, such as $B^0 \to \rho^+\rho^-$ [35, 36], $B^+ \to \rho^0\rho^+$ [37], and $B^+ \to \omega\rho^+$ [38];

Anyway, the penguin annihilation amplitude is phenomenologically indistinguishable from the QCD penguin amplitude. and no polarization observables can be calculated reliably from the theory alone, and this is the cause of the large uncertainties in the predictions.

Even thought the model in [24] seems to account for the experimental results obtained in this note, further theoretical investigations are needed. We can finally state that the measurement presented in this note gives important inputs to the theoretical frameworks of the penguin dominated B_s decay, which should help to improve the predictive power of the current theoretical tools and challenge the SM explanation of the polarization puzzle.

Appendix

A The Helicity and Transversity Formalisms

The decay amplitude would involve three complex terms proportional to the independent amplitudes, a, b and c, corresponding to the probability that the B_s^0 meson decays in a state with one of the three possible relative angular momenta: $L = 0, 1, 2$.

The most general covariant amplitude for a B meson with four-momentum p decaying into a pair of vector mesons V_1 and V_2 (with four-momentum k and q respectively) takes the form

$$\Lambda(B_s \to V_1(k)V_2(q)) = \lambda_1^{\star\mu}\lambda_2^{\star\nu}\left(ag_{\mu\nu} + \frac{b}{m_1 m_2}p_\mu p_\nu + i\frac{c}{m_1 m_2}\varepsilon^{\mu\nu\alpha\beta}k_\alpha q_\beta\right) \tag{38}$$

where, λ_1, λ_2 and m_1, m_2 represent the polarization vectors and masses of the vector mesons, respectively. Now we have to understand how these invariant amplitudes are related with the observables that we can measure. Some calculations are necessary: they are described in the following.

The starting point to obtain our observables is the definition of an appropriate reference frame. In this frame the variables necessary to the description of the process are identified as the kinematics degrees of freedom of the system. Let's refer to the B meson as the parent (or as the initial state) and to the two vector mesons as daughter particles (V_1 and V_2), and to their decay products as final state particles (P_1, P_2 from V_1, and P_3, P_4 from V_2).[6]

Each of the four final state particles has four kinematic degrees of freedom (the four components of the particle four-momentum). There are seven particles of well defined mass in the decay, which provide seven constraints from the relation between the four momentum and the invariant mass. In addition, since the entire system is translation and rotation invariant, the vector momentum of the parent B meson is irrelevant to the decay process, as well as the orientation of the decay with respect to the laboratory frame is. The former removes three degrees of freedom in the form of the vector momentum components of the B meson, while the latter removes three more in the form of Euler rotation angles of the decay frame with respect to the laboratory one. This leaves us with $16 - 7 - 3 - 3 = 3$ degrees of freedom in the decay. These remaining degrees of freedom are the angles at which the final state particles are produced. There are two standard choices we can make to define the three decay angles we wish to measure: the helicity and the transversity formalisms. They are described in the following subsections.

A.1 Helicity Basis

In the helicity basis, the three decay angles form the vector

$$\vec{\omega} = (\vartheta_1, \vartheta_2, \Phi). \tag{39}$$

We define ϑ_1 (ϑ_2) and Φ_1 (Φ_2) as the polar and azimuthal angles of the $P_1(P_3)$ three-momentum vector defined in the rest frame of their mother $V_1(V_2)$; the $z'(z")$ axis is defined as the direction of the $V_1(V_2)$ momentum in the rest frame of the B_s; the $x'(x")$ axis is an arbitrarily chosen direction in the plane normal to the $z'(z")$ axis and the and $x'(x")$ axes are defined to be opposite in direction to each other; then the y' and $y"$ axes are fixed uniquely. The Φ angle is the angle between the decay planes of the two daughter particles, given by $\Phi = \Phi_1 + \Phi_2$. These angles are shown in fig. 41.

---

[6] Fix the following convention: if the final states are charged particles, P_1 and P_3 are the positive charged ones.

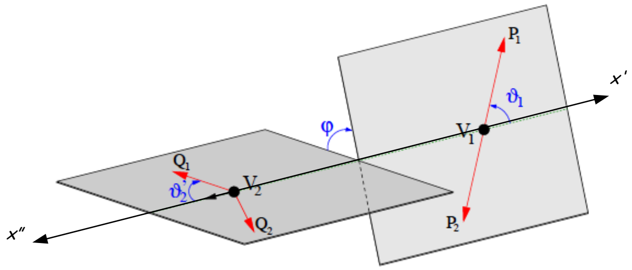

Figure 41: Definitions of the helicity angles $\vec{\omega} = (\vartheta_1, \vartheta_2, \Phi)$ for a general $P \to V_1V_2$ decay. We identify $B_s \to \phi\phi \to [K^+K^-][K^+K^-]$ with $P \to V_1V_2 \to [P_1P_2][Q_1Q_2]$.

With these definitions, it is customary to express the angular distributions in terms of the *helicity amplitudes*

$$H_\lambda = \langle V_1(\lambda)V_2(\lambda)|\,\mathcal{H}^{\text{eff}}\,|B_s\rangle \tag{40}$$

for $\lambda = 0, \pm 1$ (in the B rest frame $\lambda_1 = \lambda_2 = \lambda$). $\mathcal{H}^{\text{eff}}$ is the effective Hamiltonian which describes the transition. Note that $|H_0|^2 + |H_+|^2 + |H_-|^2 = 1$. The relations between the helicity and the invariant amplitudes are

$$H_0 = -au - b(u^2-1) \tag{41a}$$

$$H_\pm = -a \pm \sqrt{u^2-1}c \tag{41b}$$

where $u = p_1p_2/m_1m_2$.

In general, the explicit form of the angular distribution depends on the spin of the decay products of the two vector mesons. If the decay has pseudoscalar mesons in the final state, the normalized angular distribution is:

$$\begin{aligned}\frac{1}{\Gamma}\frac{d^3\Lambda}{d\vec{\omega}} = \frac{9}{8\pi}\Bigg[&\frac{1}{4}\frac{\Gamma_{\text{T}}}{\Gamma}\sin^2\vartheta_1\sin^2\vartheta_2 + \frac{\Gamma_{\text{L}}}{\Gamma}\cos^2\vartheta_1\cos^2\vartheta_2 + \\ &+\frac{1}{4}\sin 2\vartheta_1\sin 2\vartheta_2(\alpha_1\cos\Phi - \beta_1\sin\Phi) + \\ &+\frac{1}{2}\sin^2\vartheta_1\sin^2\vartheta_2(\alpha_2\cos 2\Phi - \beta_2\sin 2\Phi)\Bigg]\end{aligned} \tag{42}$$

where

$$\begin{aligned}
\frac{\Gamma_{\mathrm{T}}}{\Gamma} &= \frac{|H_+|^2 + |H_-|^2}{|H_0|^2 + |H_+|^2 + |H_-|^2} \\
\frac{\Gamma_{\mathrm{L}}}{\Gamma} &= \frac{|H_0|^2}{|H_0|^2 + |H_+|^2 + |H_-|^2} \\
\alpha_1 &= \frac{\Re(H_+ H_o^\star + H_- H_0^\star)}{|H_0|^2 + |H_+|^2 + |H_-|^2} \\
\beta_1 &= \frac{\Im(H_+ H_o^\star + H_- H_0^\star)}{|H_0|^2 + |H_+|^2 + |H_-|^2} \\
\alpha_2 &= \frac{\Re(H_+ H_-^\star)}{|H_0|^2 + |H_+|^2 + |H_-|^2} \\
\beta_2 &= \frac{\Im(H_+ H_-^\star)}{|H_0|^2 + |H_+|^2 + |H_-|^2}
\end{aligned} \tag{43}$$

A.2 Transversity Basis

To obtain the advantage of more easily extracting the CP-odd and CP-even components, the angular distribution is often written in the *linear polarization* basis, which is defined in the following form

$$\Lambda(B_s \to V_1 V_2) = A_0 \frac{\lambda_1^{\star L} \lambda_2^{\star L}}{u} - A_\parallel \frac{\lambda_1^{\star T} \cdot \lambda_2^{\star T}}{\sqrt{2}} - i A_\perp \frac{(\lambda_1^\star \times \lambda_2^\star) \cdot \hat{p}_2}{\sqrt{2}} \tag{44}$$

where u has been previously defined and $\hat{p}_2$ is the unit vector along the V_2 motion direction in the V_1 rest frame. The symbols λ_i^L represent the longitudinal components of the polarization vectors ($\lambda_1^L = \lambda_1 \cdot \vec{k}/|\vec{k}|$, $\lambda_2^L = \lambda_2 \cdot \vec{q}/|\vec{q}|$), while λ_i^T are the transverse component, $\lambda_i^T = \lambda_i - \lambda_i^L$. The transversity amplitudes A_0, $A_\parallel$ and $A_\perp$ are related to the helicity ones by

$$A_0 = H_0, \tag{45a}$$

$$A_\parallel = \frac{H_+ + H_-}{\sqrt{2}} \tag{45b}$$

$$A_\perp = \frac{H_+ - H_-}{\sqrt{2}} \tag{45c}$$

and the unitarity relation $|A_0|^2 + |A_\parallel|^2 + |A_\perp|^2 = 1$ is still valid. These amplitudes are often referred to as *polarization amplitudes.*

In the rest frame of V_1, V_2 moves in the x direction, and the z axis is perpendicular to the decay plane of $V_2 \to P_3 P_4$ and we assume that the y-component of the P_3 three-momentum is non-negative. (Θ, Φ) are the angular coordinates of P_1 and Ψ is that of P_2, both in the rest frame of V_1 (see fig. 42). Then, the three transversity angles form the angles vector:

$$\vec{\Omega} = (\Theta, \Psi, \Phi). \tag{46}$$

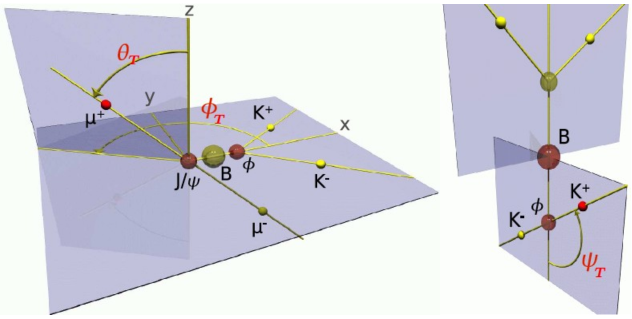

Figure 42: Definitions of the transversity angles.

The normalized differential decay rate in terms of the transversity amplitudes is given by

$$\begin{aligned}\frac{1}{\Gamma}\frac{d^3\Lambda}{d\vec{\Omega}} = \frac{9}{8\pi}\Bigg[&\frac{\Gamma_{\mathrm{L}}}{\Gamma}\cos^2\Psi\sin^2\Theta\cos^2\Phi + \frac{\Gamma_\perp}{2\Gamma}\sin^2\Psi\sin^2\Theta\sin^2\Phi + \\ &+\frac{\Gamma_\parallel}{2\Gamma}\sin^2\Psi\sin^2\Theta - \frac{\zeta}{2\sqrt{2}}\sin 2\Psi\sin^2\Theta\sin 2\Phi - \\ &-\frac{\xi_1}{2}\sin^2\Psi\sin 2\Theta\sin\Phi + \frac{\xi_2}{2\sqrt{2}}\sin 2\Psi\sin 2\Theta\cos\Phi\Bigg],\end{aligned} \tag{47}$$

where

$$\begin{aligned}\frac{\Gamma_{\mathrm{L}}}{\Gamma} &= \frac{|A_0|^2}{|A_0|^2+|A_\parallel|^2+|A_\perp|^2}\\ \frac{\Gamma_\perp}{\Gamma} &= \frac{|A_\perp|^2}{|A_0|^2+|A_\parallel|^2+|A_\perp|^2}\\ \frac{\Gamma_\parallel}{\Gamma} &= \frac{|A_\parallel|^2}{|A_0|^2+|A_\parallel|^2+|A_\perp|^2}\\ \zeta &= \frac{\Re(A_\parallel A_0^\star)}{|A_0|^2+|A_\parallel|^2+|A_\perp|^2}\\ \xi_1 &= \frac{\Im(A_\perp A_\parallel^\star)}{|A_0|^2+|A_\parallel|^2+|A_\perp|^2}\\ \xi_2 &= \frac{\Im(A_\perp A_0^\star)}{|A_0|^2+|A_\parallel|^2+|A_\perp|^2}\end{aligned} \tag{48}$$

B Normalization of the Angular Distributions

In the final likelihood formulation, the signal angular pdf is expressed as the product of a function of the three helicity angles, $f(\vec{\omega}) = \sum_{i=1}^{6} K_i f_i(\vec{\omega})$, (eq. 20), and a three-dimensional histogram, $H(\vec{\omega})$, that models the detector angular acceptance $\mathcal{A}(\vec{\omega})$.[7]

In this appendix we are going to discuss the numerical technique used for the normalization $\mathcal{N}$ of such pdf:

$$g_{\mathrm{s}}(\vec{\omega}) = \frac{1}{\mathcal{N}} H(\vec{\omega}) f(\vec{\omega}) \tag{49}$$

Naively, we have to evaluate the integral of a mathematical function multiplied by a function represented by a histogram. We cannot anymore compute it analytically, but we need a numerical computation. In order to simplify the problem, let's start with the one-dimensional case.

Given an integrable function $f(x)$ ($\int f(x)\,dx = F(x)$), a histogram $\gamma(x)$ normalized to one and a number of bins N along the x axis, the numerical computation of the normalization factor $\mathcal{N}$

$$\mathcal{N} = \int_{x_{\mathrm{min}}}^{x_{\mathrm{max}}} f(x)\gamma(x)\,dx \tag{50}$$

can be approximated by the following sum:

$$\mathcal{N} \simeq \sum_{j}^{N} \mathcal{I}_j^f \mathcal{I}_j^\gamma \tag{51}$$

where

$$\mathcal{I}_j^f = \int_{x^j_{\mathrm{min}}}^{x^j_{\mathrm{max}}} f(x)\,dx \tag{52a}$$

$$\mathcal{I}_j^\gamma = \gamma(x_j)\Delta_j \tag{52b}$$

and x_j is the central point of the j-th bin $\Delta_j = x^j_{\mathrm{max}} - x^j_{\mathrm{min}}$ (see fig. 43). If the bin width is constant for each j ($\Delta_j = \Delta$), then we can write

$$\mathcal{N} = M\Delta \tag{53}$$

where

$$\begin{aligned} M &= \sum_{j}^{N} \mathcal{I}_j^f \gamma(x_j) = \\ &= \Big[F(x^1_{\mathrm{max}}) - F(x^1_{\mathrm{min}})\Big]\gamma(x_1) + \cdots + \Big[F(x^N_{\mathrm{max}}) - F(x^N_{\mathrm{min}})\Big]\gamma(x_N) \end{aligned} \tag{54}$$

---

[7] For the moment, we can consider the pdf to be a function only of the angles without loss of generality, although the pdf of the time-dependent fit has also the B meson proper decay time. For the transversity variables, one has exactly the same situation, considering $\vec{\Omega}$ instead of $\vec{\omega}$.

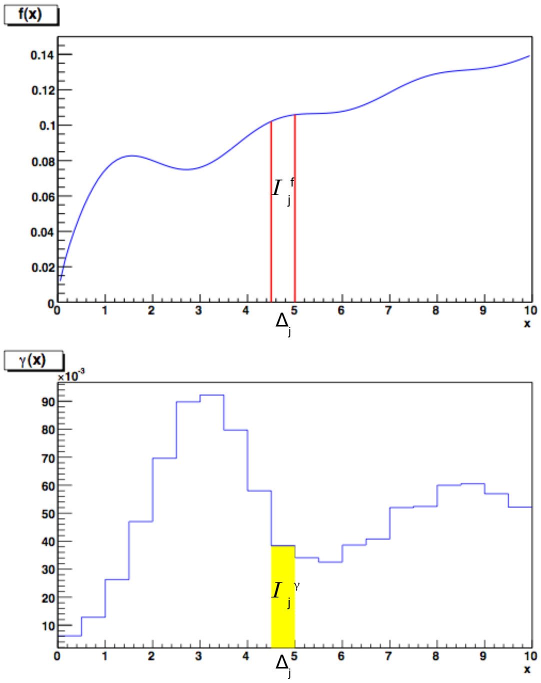

Figure 43: Graphical example of the $\mathcal{I}_j^f$ and the $\mathcal{I}_j^\gamma$ terms.

If $F(x)$ is a linear combination of two (or more) functions of x, $F(x) = K_1F_1(x) + K_2F_2(x)$, M can be easily evaluated:

$$\begin{aligned}
M &= \big(F(x^1_{\text{max}}) - F(x^1_{\text{min}})\big)\gamma(x_1) + \cdots + \big(F(x^N_{\text{max}}) - F(x^N_{\text{min}})\big)\gamma(x_N) = \\
&= K_1\Big[\big(F_1(x^1_{\text{max}}) - F_1(x^1_{\text{min}})\big)\gamma(x_1) + \cdots + \big(F_1(x^N_{\text{max}}) - F_1(x^N_{\text{min}})\big)\gamma(x_N)\Big] + \\
&+ K_2\Big[\big(F_2(x^1_{\text{max}}) - F_2(x^1_{\text{min}})\big)\gamma(x_1) + \cdots + \big(F_2(x^N_{\text{max}}) - F_2(x^N_{\text{min}})\big)\gamma(x_N)\Big] = \\
&= K_1w_1 + K_2w_2
\end{aligned} \tag{55}$$

where in the last line we define the weights $w_i = \big(F_i(x^1_{\text{max}}) - F_i(x^1_{\text{min}})\big)\gamma(x_1) + \cdots + \big(F_i(x^N_{\text{max}}) - F_i(x^N_{\text{min}})\big)\gamma(x_N)$.

The extension to our three-dimensional case is then straightforward, replacing:

$$
\begin{aligned}
f(x) &\rightarrow f(\vec{\omega}) = \sum_{i=1}^{6} K_i f_i(\vec{\omega}) \\
\int f(x)dx = F(x) &\rightarrow \int f(\vec{\omega})\, d\vec{\omega} = F(\vec{\omega}) = \sum_{i=1}^{6} K_i F_i(\vec{\omega}) \\
\gamma(x) &\rightarrow H(\vec{\omega})
\end{aligned}
\tag{56}
$$

and the bin width becomes a bin volume: $\Delta \rightarrow V$. The function $f(\omega)$ is normalized by the following integral over the total solid angle:

$$
\int_{-1}^{1}\int_{-1}^{1}\int_{0}^{2\pi} f(\vec{\omega})\, d\cos\vartheta_1\, d\cos\vartheta_2\, d\Phi = \frac{32\pi}{9(K_1+K_2+K_3)} = \frac{1}{\eta(K_1,K_2,K_3)}. \tag{57}
$$

Then, the normalized pdf is

$$
g_{\mathrm{s}}(\vec{\omega}) = \frac{\eta(K_1,K_2,K_3)\sum_{i=1}^{6} K_i f_i(\vec{\omega})}{\sum_{i=1}^{6} K_i w_i}\frac{H(\vec{\omega})}{\mathcal{V}} \tag{58}
$$

The parameters we want to estimate within the fit are all contained in the K_i coefficients. Thus, the weights w_i can be computed once, before starting the maximization procedure, since they are constant and don't depend on the parameters. Moreover, assuming no CP-violation and summing over B_s and $\bar{B}_s$ terms, we have only K_1, K_2, K_3 and K_5, as we described in Sect. 3.1.

In the case of the time-integrated fit:

$$
\begin{aligned}
K_1 &= |A_0|^2/\Gamma_{\mathrm{L}} \\
K_2 &= |A_{\parallel}|^2/\Gamma_{\mathrm{L}} \\
K_3 &= |A_{\perp}|^2/\Gamma_{\mathrm{H}} \\
K_5 &= |A_0||A_{\parallel}|\cos\delta_{\parallel}/\Gamma_{\mathrm{L}}
\end{aligned}
\tag{59}
$$

then, the $\eta(K_1,K_2,K_3)$ becomes:

$$
\eta(K_1,K_2,K_3) = \frac{9}{32\pi}\frac{1}{\frac{|A_0|^2+|A_{\parallel}|^2}{\Gamma_{\mathrm{L}}} + \frac{|A_{\perp}|^2}{\Gamma_{\mathrm{H}}}} \tag{60}
$$

where one recognizes that the second fraction is the term $1/\tilde{W}$ of eq. 20 in the Sect. 7.4.

C Fit with different parameters set

Here we report the results and tests of a previous version of the fit. It differs from the one described in Sec. 7 by the use of a different background parametrization and of $\cos\delta_\parallel$ instead of $\delta_\parallel$ as a fitting parameter.

C.1 Fit functions parametrizations

Only the parts which differ from Sec. 7 are reported in this section.

C.1.1 Background Parametrization

The angular background pdf is:

$$g_\mathrm{b} = g_\mathrm{b}^{(\omega_1)} g_\mathrm{b}^{(\omega_2)} g_\mathrm{b}^{(\omega_3)} \tag{61}$$

where for the $B_s^0 \to \phi\phi$ decay the parametrizations adopted are:

$$g_\mathrm{b}^{(\omega_1)} = \frac{1}{2(1+\frac{B_1}{3})}\left(1 + B_1\cos^2\vartheta_1\right), \tag{62a}$$

$$g_\mathrm{b}^{(\omega_2)} = \frac{1}{2(1+\frac{B_2}{3})}\left(1 + B_2\cos^2\vartheta_2\right), \tag{62b}$$

$$g_\mathrm{b}^{(\omega_3)} = \frac{1}{2\pi(1+B_3\pi)}\left(1 + B_3\cos\varPhi\right),, \tag{62c}$$

We perform a binned fit to the sideband angular distributions using the above equations. Though this is a simple description, we find that it is adequate to describe the angular distributions in the sidebands (see Figure 44).

Parameter	Binned fit value
B_1	-14 ± 10
B_2	-11 ± 10
B_3	0.02 ± 0.03

Table 24: Parameters of the binned sidebands fit for $B_s^0 \to \phi\phi$ fit.

C.1.2 Parameters Summary

Let us summarize all the parameters that enter the complete Likelihood in the final fit. The input variables are the mass m and the helicity angles $\vec{\omega} = (\vartheta_1, \vartheta_2, \varPhi)$ for each reconstructed candidate that passed the off-line selection. The ten fit parameters are reported in tab. 25.

	Signal	Background
Mass	M, σ	f_b, b
Angular	$\lvert A_0\rvert^2$, $\lvert A_\parallel\rvert^2$, $\delta_\parallel$	B_1, B_2, B_3

Table 25: Parameters summary of the time-integrated $B_s^0 \to \phi\phi$ fit.

The following quantities are fixed in the final fit:

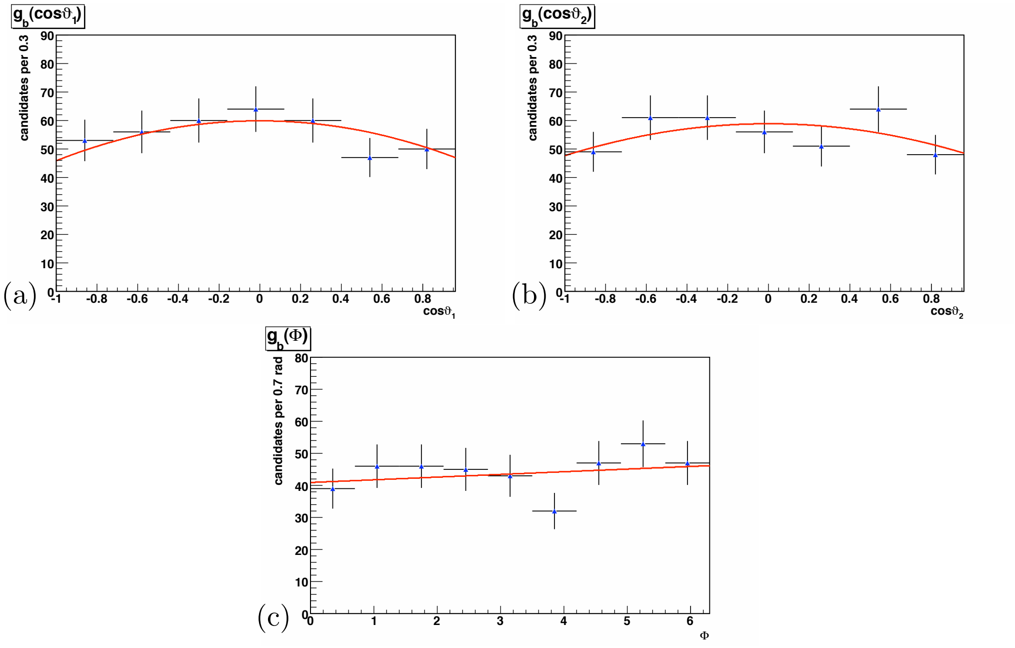

Figure 44: Side-bands data fit to determine the background parametrizations for the $B_s^0 \to \phi\phi$ decay: $\cos\vartheta_1$ (a), $\cos\vartheta_2$ (b) and Φ (c). Black points are side-bands data; red lines are the fitting functions described in the text.

- k and h, from the MC fit;
- τ_{L} and τ_{L}, the two mean life-time of the B_s^0 mass eigenstates, are taken from the last PDG values (eq. (6a));

Before carrying out the fit over the data sample, we perform several tests. The aim is to validate the correctness of the implementation, to investigate the likelihood behavior as function of the parameters, to look at their resolutions and to detect any potential fit biases. The tests that we perform are:

1. the pulls distributions;
2. the fit of $B_s^0 \to J/\psi\phi$, used as a control sample;
3. the fit of the realistic MC;

They are described in the following sections.

C.2 Pulls Distributions

At first stage, we perform the fit on 1000 pseudo-experiments of 100000 events each: it's about 200 times the events per experiment that we have in the actual $B_s^0 \to \phi\phi$ data samples, so it is mostly a test of the fitter as a machinery to correctly extract the parameters given in input to generate the toyMC sample. The fraction of signal to background is fixed to reproduce the real data sample. We generate the events using as input parameters the results of the final fit performed on the actual $B_s^0 \to \phi\phi$ sample, which are described in the last subsection of this Section. The results of this test are very satisfactory; they are presented in tab. 26. The pull distributions are reported in fig. 45.

Parameter	Input value	Mean	Variance	Prob(χ^2) [%]
M	5.364 GeV/c^2	-0.01 ± 0.03	0.96 ± 0.02	34
σ	0.016 GeV/c^2	-0.06 ± 0.03	0.98 ± 0.02	28
f_{b}	0.38	0.03 ± 0.03	1.02 ± 0.02	31
b	2.7 c^2/GeV	-0.04 ± 0.03	1.03 ± 0.02	6
$\|A_0\|^2$	0.35	0.02 ± 0.03	1.01 ± 0.02	98
$\|A_{\|\|}\|^2$	0.29	0.00 ± 0.03	1.00 ± 0.02	86
$\delta_{\|\|}$	2.74 rad	0.05 ± 0.03	1.02 ± 0.02	28
B_1	0.3	0.04 ± 0.03	0.98 ± 0.02	68
B_2	0.8	0.02 ± 0.03	1.00 ± 0.02	75
$B_3 i$	0.03	0.00 ± 0.03	1.05 ± 0.02	6

Table 26: Pulls mean and variance for $B_s^0 \to \phi\phi$ (100000 events per pseudo-experiment). The fifth column presents the χ^2 probability for a gaussian fit of the pulls distribution with mean and variance 0 and 1, respectively.

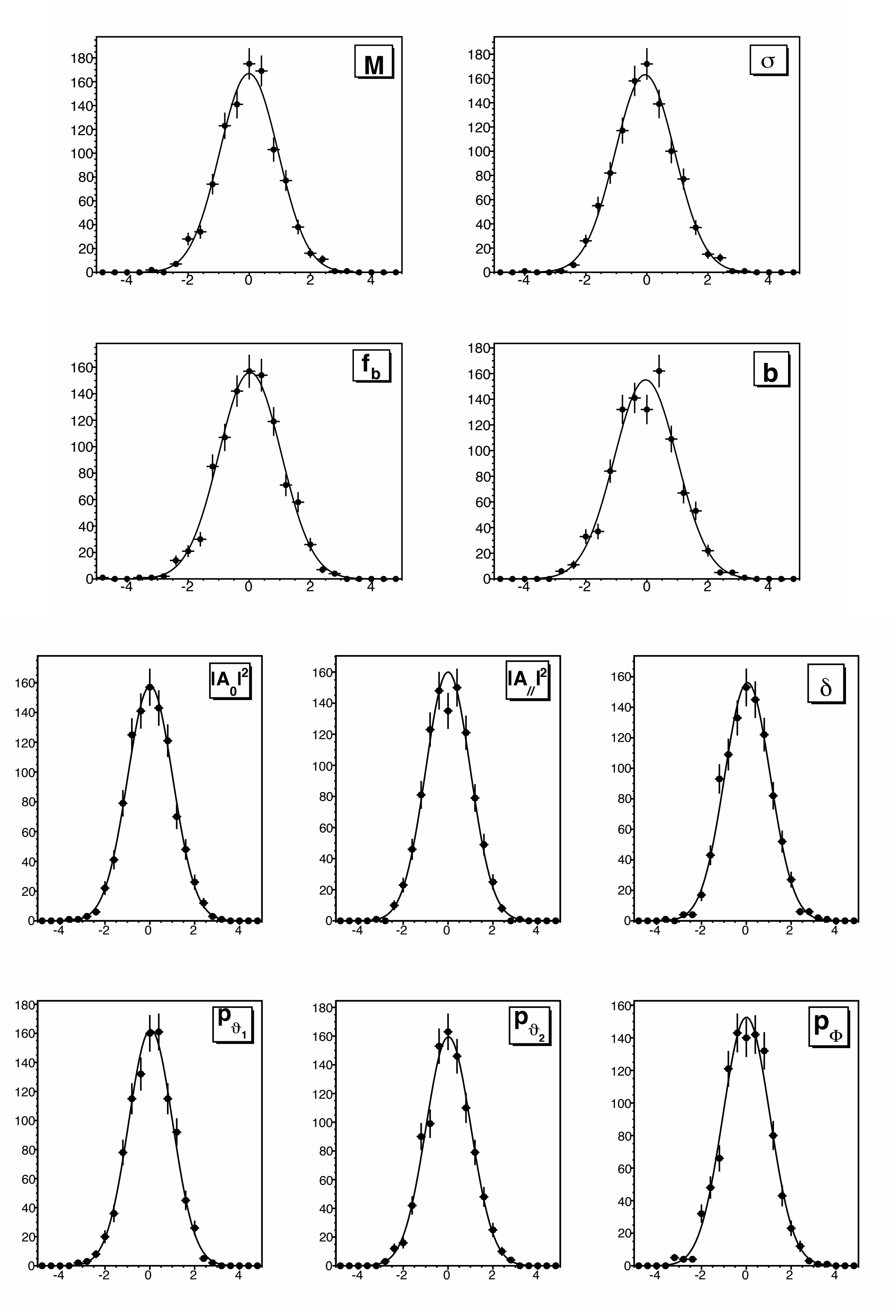

Figure 45: Pulls distributions of fit parameters for $B_s^0 \to \phi\phi$ (100000 events per pseudo-experiment).

C.2.1 Expected Resolution on the Polarization Observables

We repeat the previous test fitting samples with 480 events for each pseudo-experiments, which is the statistics we have in the actual B_s^0 sample. In this way, we can check if there is any significant change in the fitter behavior that might be caused by the lower statistic. Again, the generation of pseudo-experiments is done using as input parameters the results of the final fit performed on the actual $B_s^0 \to \phi\phi$ sample. The results of this test are reported in tab. 27, and the pulls distributions are shown in fig. 46. The resolution (third column of the table) of the polarization amplitudes are consistent with the one expected in Sect. 1 (4%).

Parameter	Input value	Average fit error	Mean	Variance	Prob(χ^2) [%]
M	5.364 GeV/c^2	0.0011 GeV/c^2	-0.05 ± 0.03	1.04 ± 0.02	21
σ	0.016 GeV/c^2	0.0010 GeV/c^2	-0.07 ± 0.03	1.03 ± 0.02	19
f_{b}	0.38	0.03	-0.04 ± 0.03	1.03 ± 0.02	36
b	2.7 c^2/GeV	0.7 c^2/GeV	-0.01 ± 0.03	0.96 ± 0.02	14
$\|A_0\|^2$	0.35	0.039	0.00 ± 0.03	0.94 ± 0.02	99
$\|A_{\|\|}\|^2$	0.29	0.039	0.01 ± 0.03	0.96 ± 0.02	89
$\delta_{\|\|}$	2.74 rad	0.44 rad	0.12 ± 0.03	0.95 ± 0.02	0
B_1	0.3	0.3	0.09 ± 0.03	1.01 ± 0.02	0
B_2	0.8	0.5	0.07 ± 0.03	1.02 ± 0.02	0
B_3	0.03	0.06	0.21 ± 0.03	1.03 ± 0.02	0

Table 27: Pulls mean and variance for $B_s^0 \to \phi\phi$ (480 events per pseudo-experiment). In the second column the input parameters of the generation are listed. The third column reports the average error in the pseudo-experiments fit (resolution). The fourth and the fifth columns list the mean value and the variance of the pull distributions, respectively. The sixth column presents the χ^2 probability for a gaussian fit of the pulls distribution with mean and variance 0 and 1, respectively.

We find that the fitter returns unbiased estimates for all parameters except for $\delta_{||}$ and the background parameters B_i. The uncertainties of the polarizations amplitudes seem to be a little overestimated, with a bias of order of 6%. The strong phase $\delta_{||}$ seems to be affected by a different problem, since the distribution is not gaussian. These complications arise in presence of low statistic: the fit on the data sample might returns a biased estimates for these parameters. The behavior of the $\delta_{||}$ pull distribution requires further examination that it is performed in subsection C.2.3.

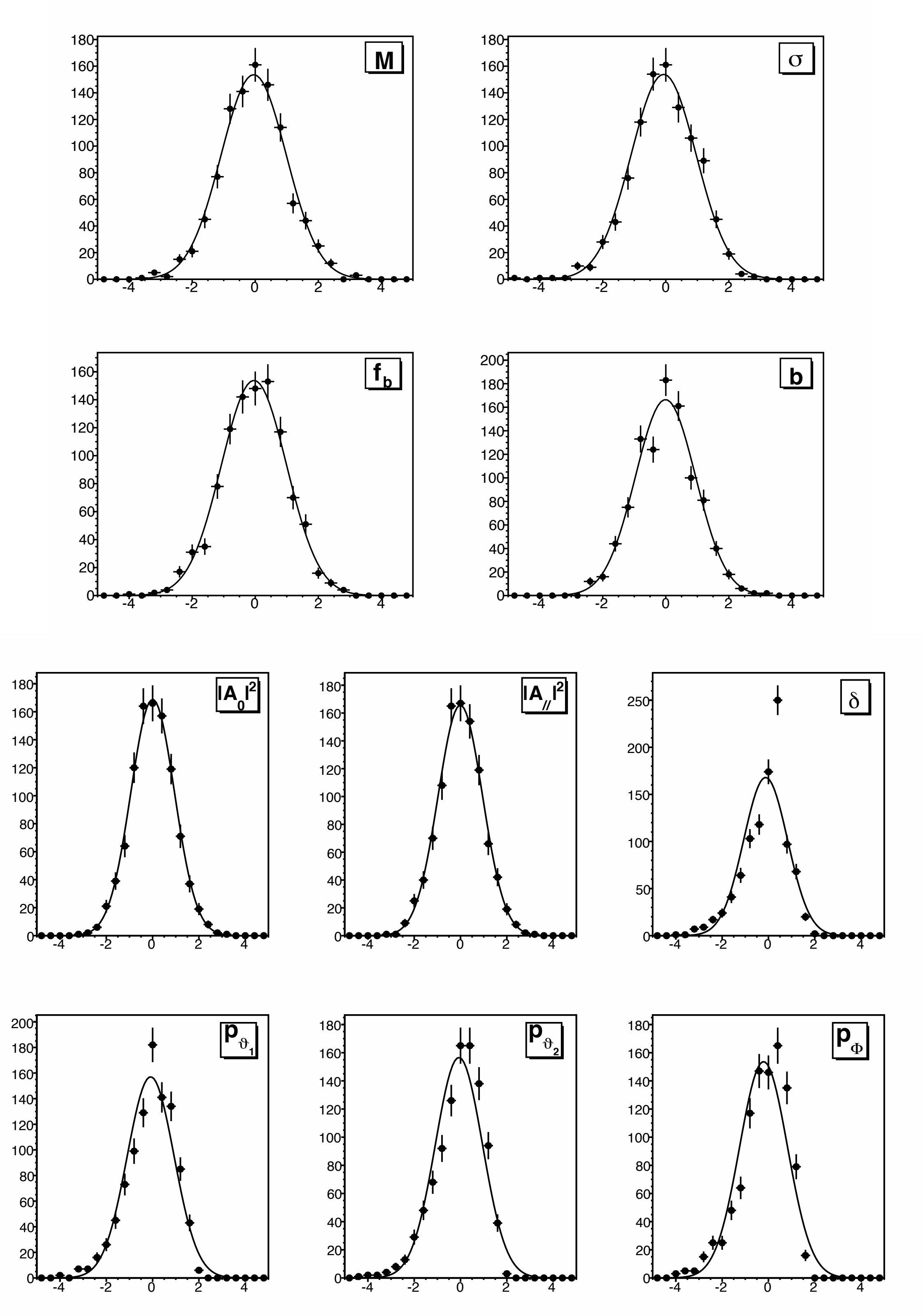

Figure 46: Pulls distributions of fit parameters for $B_s^0 \to \phi\phi$ (480 events per pseudo-experiment).

C.2.2 Pulls for different sets of Input Parameters

The fitter must estimate unbiased parameters independently of the specif value of the parameters. Naively, since in principle there is no criteria to prefer some values with respect to others, we don't want that the fitter results depend on the parameters value. Thus, in order to check if this condition is satisfied, we perform a pulls distributions test by changing one by one the input parameters for the generation of the pseudo-experiments variables.

In tab. 28, we report the result of the test; four different sets of input values are given. Since we are interest in the polarization amplitudes, we fixed the mass parameters and we vary the values of the signal angular parameters. Because of its problematic nature shown in the previous section, the strong phase $\delta_{\|}$ is discussed separately.

Parameter	Input value	Average fit error	Mean	Variance	Prob(χ^2) [%]
$\|A_0\|^2$	0.2	0.03	-0.12 ± 0.03	0.99 ± 0.02	20
$\|A_{\|}\|^2$	0.4	0.03	0.03 ± 0.03	1.03 ± 0.02	16
δ	1.57 rad	0.1 rad	0.05 ± 0.03	1.01 ± 0.02	26
$\|A_0\|^2$	0.7	0.02	0.03 ± 0.03	1.03 ± 0.02	2
$\|A_{\|}\|^2$	0.1	0.02	-0.04 ± 0.03	0.98 ± 0.02	61
δ	1.57 rad	0.1 rad	-0.01 ± 0.03	0.98 ± 0.02	47
$\|A_0\|^2$	0.2	0.02	-0.05 ± 0.05	1.02 ± 0.03	4
$\|A_{\|}\|^2$	0.7	0.02	0.06 ± 0.05	1.02 ± 0.03	8
δ	1.57 rad	0.1 rad	-0.04 ± 0.05	1.04 ± 0.03	65
$\|A_0\|^2$	0.1	0.03	-0.08 ± 0.05	1.03 ± 0.03	81
$\|A_{\|}\|^2$	0.2	0.03	0.04 ± 0.04	1.02 ± 0.03	2
δ	1.57 rad	0.2 rad	0.05 ± 0.04	0.94 ± 0.03	11

Table 28: Pulls test for different sets of input parameters.

On average we are satisfied with the results obtained. The resolution for each parameter doesn't appreciably change for each set.[8] One could just argue about the result for $|A_0|^2$ pull mean in the first set of values in tab. 28. since thi is just a little bias, for the moment we disregard this issue and we'll check it better in the case the fit results on actual data presents a similar set of parameters. The other parameters pulls that are not shown in tab. 28 are all gaussian, with mean value and variance consistent with 0 and 1, respectively.

C.2.3 The Measurement of the Phase

We want to better understand the behavior of the $\delta_{\|}$ pulls distributions. First, from the previous tests, we learned that this complication:

- arises only in presence of low statistic;
- vanishes for $\delta \simeq \pi/2$ rad, as one can see in table 28.

We perform a set of pseudo-experiments changing the input value of the strong phase to span the interval $[0, 2\pi]$ rad. We don't change all other parameters (also the polarization amplitudes, $|A_0|^2$ and $|A_{\|}|^2$). We report the results of the $\delta_{\|}$ pulls distributions in tab. 29. This study puts in

---

[8] The tests are performed using 1000 events per pseudo-experiments.

$\delta_{\parallel}$ Input value [rad]	Mean	Variance	Prob(χ^2) [%]
0.0	//	//	//
$\pi/16$	0.15 ± 0.06	0.84 ± 0.05	0
$\pi/8$	0.21 ± 0.04	0.93 ± 0.03	0
$\pi/4$	0.11 ± 0.04	0.92 ± 0.03	6
$\pi/2$	0.01 ± 0.05	1.04 ± 0.03	89
$3\pi/4$	0.05 ± 0.04	0.97 ± 0.03	0
$7\pi/8$	-0.12 ± 0.04	0.97 ± 0.03	0
π	//	//	//
$9\pi/8$	0.15 ± 0.06	0.89 ± 0.04	0
$3\pi/2$	-0.02 ± 0.05	1.04 ± 0.03	74
$15\pi/8$	-0.22 ± 0.04	0.93 ± 0.03	0

Table 29: Pulls test to study the behavior of the strong phase pulls.

evidence a periodic behavior of the pull distributions: if the input value is near either to $\delta_{\parallel} \simeq 0$ rad or to $\delta_{\parallel} \simeq \pi$ rad, the pulls are not gaussian and the fitter returns a biased estimate. The biases are greater as $\delta_{\parallel}$ is closer to those two values, referred to as critic points. Although, when the input value is $\delta_{\parallel} \simeq \pi/2$ rad or $\delta_{\parallel} \simeq 3\pi/2$ rad the pulls are gaussian.

Furthermore, if we look to the distributions of the fitted value in the pseudo-experiments, we found a strange behavior, that is the origin of the pulls distribution issue. When the input phase is close to the critic points, *e. g.*, $\pi/16$ rad ($9\pi/8$ rad), the fitter fails the parameter estimation and it often returns the value of the closest critic point, *i. e.*, 0 rad (π rad). The distribution presents a peak centered on the specific critic point value, as one can see in some representative distributions in fig. 47. Thus, the $\delta_{\parallel}$ pulls issue is due to those pseudo-experiments in which the fit returns a certain critic point as parameter value. This is as less probable as farther to a critic points the input value is, or as larger the statistic is.

We can explain its periodic behavior in the range $[0, 2\pi]$ rad: since the strong phase $\delta_{\parallel}$ enters the fit as the argument of the cosine function, there is an ambiguity on its definition, because, naively speaking, $\cos(\delta_{\parallel}) = \cos(-\delta_{\parallel})$. This implies that the likelihood function has two equivalent maxima in the $\delta_{\parallel}$ space. They can be seen in fig. 50 of Sec. C.3. If we make the likelihood scan of one of the pseudo-experiments (generated with the input value $\delta_{\parallel} = 0.43$ rad, thus, near the critic point 0) where the fits estimates $\delta_{\parallel} = 0$, we can see that the likelihood profile doesn't present the expected double minima, which seem to collapse in a single minimum point (see fig. 48).[9] Moreover, the likelihood profile seems not to have the costumary parabolic shape. The same thing happens for the pseudo-experiments generated with some values of $\delta_{\parallel}$ next to π, when the fit estimate is $\delta_{\parallel} = \pi$.

C.3 Time-integrated Fit to Real Data

The results of the fit performed on 2.9 fb^{-1} of data for the $B_s^0 \to \phi\phi$ are finally listed in the table 30. We observe that the statistical uncertainties of the polarization amplitudes are of the same order of the ones that we have quoted in Sect. 1. The correlation coefficients are listed in tab. 31

The time-integrated fit projections onto the three helicity angles are shown in fig. 49: we see

---

[9] This scan of the likelihood function is done by varying the parameter, leaving all other parameters fixed at the value of the minimum.

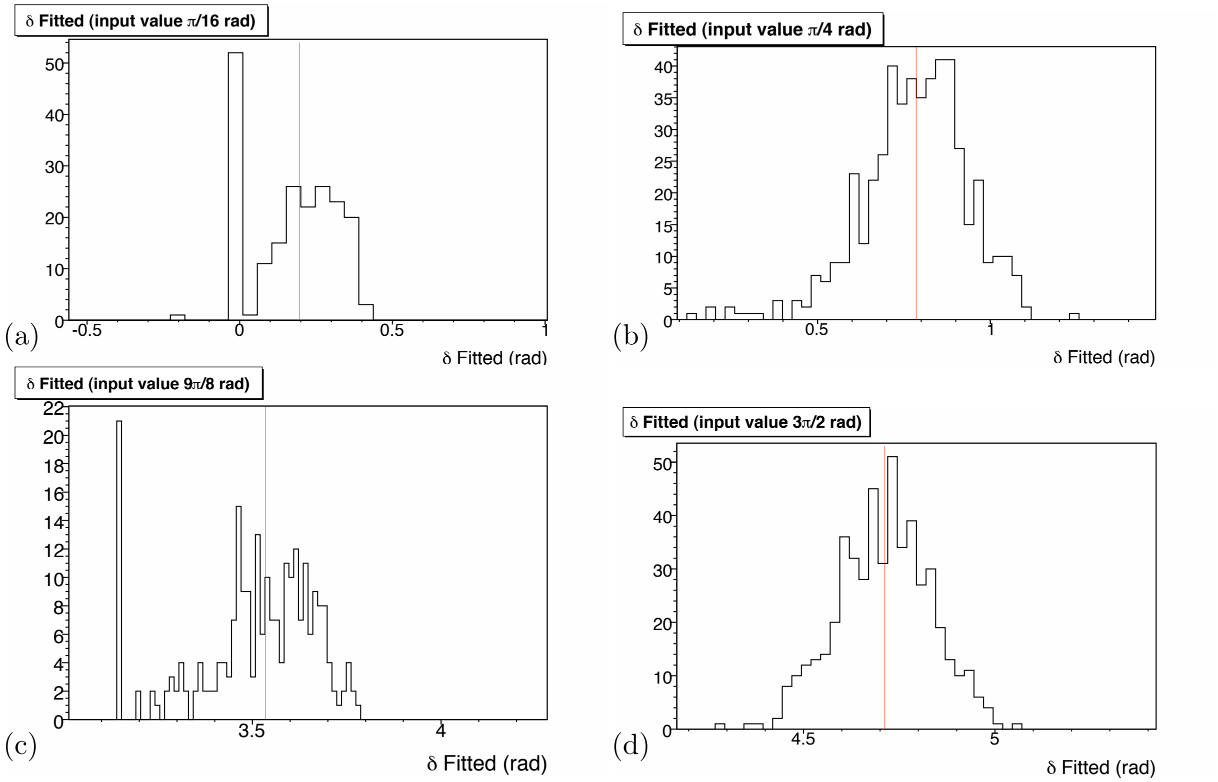

Figure 47: Distribution of the $\delta_{\|}$ fitted values in the pseudo-experiments for four different input values: $\delta_{\|} = \pi/16$ (a), $\delta_{\|} = \pi/4$ (b), $\delta_{\|} = 9\pi/8$ (c) and $\delta_{\|} = 3\pi/2$ (d). The red lines represent the value of the input parameter.

Parameter	Fit value
M [GeV/c^2]	5.3635 ± 0.0012
σ [GeV/c^2]	0.0164 ± 0.0011
f_{b}	0.383 ± 0.030
b [c^2/GeV]	2.68 ± 0.67
$\lvert A_0\rvert^2$	0.347 ± 0.041
$\lvert A_{\|}\rvert^2$	0.287 ± 0.043
$\delta_{\|}$ [rad]	2.71 ± 0.36
B_1	0.26 ± 0.33
B_2	0.79 ± 0.47
B_3	0.03 ± 0.06

Table 30: Results of the time-integrated fit for $B_s^0 \rightarrow \phi\phi$.

that the data distributions are very well reproduced by the fitting functions. The χ^2 probabilities of the fit projections are 0.46 for $\cos\vartheta_1$, 0.62 for $\cos\vartheta_2$ and 0.11 for Φ.

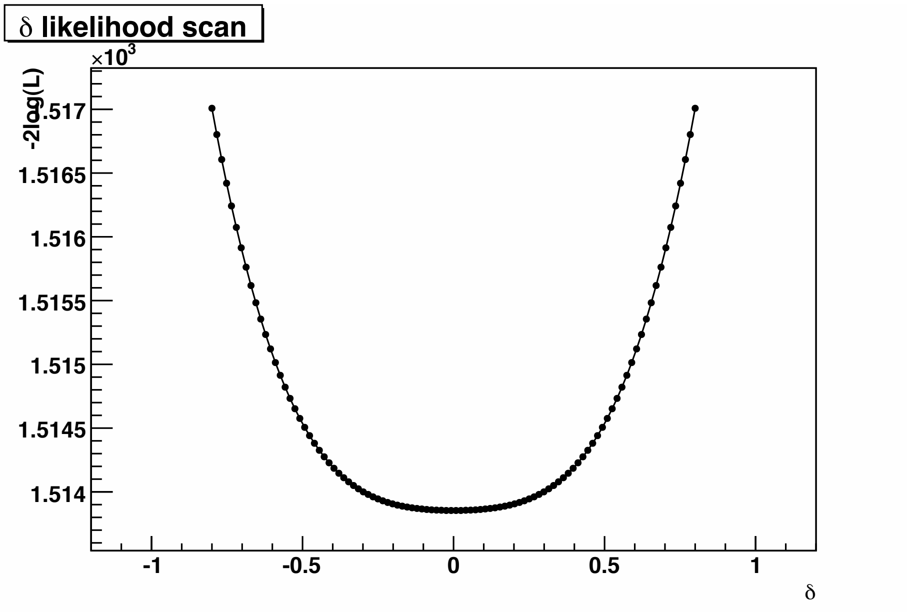

Figure 48: Likelihood scan of a pseudo-experiment with $\delta_\parallel = 0$ fitted.

	M	σ	f_b	b	$\lvert A_0\rvert^2$	$\lvert A_\parallel\rvert^2$	$\delta_\parallel$	B_1	B_2	B_3
M	$+1.000$	-0.032	$+0.018$	$+0.068$	$+0.001$	-0.011	-0.014	$+0.004$	$+0.009$	$+0.005$
σ	-0.032	$+1.000$	-0.358	-0.019	$+0.053$	-0.024	$+0.110$	$+0.048$	-0.010	$+0.021$
f_b	$+0.018$	-0.358	$+1.000$	$+0.017$	-0.062	$+0.020$	-0.152	-0.032	-0.020	$+0.026$
b	$+0.068$	-0.019	$+0.017$	$+1.000$	-0.003	-0.003	-0.000	$+0.001$	$+0.004$	$+0.003$
$\lvert A_0\rvert^2$	$+0.001$	$+0.053$	-0.062	-0.003	$+1.000$	-0.447	$+0.132$	-0.153	-0.158	-0.017
$\lvert A_\parallel\rvert^2$	-0.011	-0.024	$+0.020$	-0.003	-0.447	$+1.000$	$+0.101$	$+0.068$	$+0.085$	$+0.001$
$\delta_\parallel$	-0.014	$+0.110$	-0.152	-0.000	$+0.132$	$+0.101$	$+1.000$	$+0.003$	-0.033	-0.010
B_1	$+0.004$	$+0.048$	-0.032	$+0.001$	-0.153	$+0.068$	$+0.003$	$+1.000$	$+0.078$	$+0.031$
B_2	$+0.009$	-0.010	-0.020	$+0.004$	-0.158	$+0.0985$	-0.033	$+0.078$	$+1.000$	$+0.009$
B_3	$+0.005$	$+0.021$	$+0.026$	$+0.003$	-0.017	$+0.001$	-0.010	$+0.031$	$+0.009$	$+1.000$

Table 31: Correlation coefficients of the time-integrated fit for $B_s \to \phi\phi$.

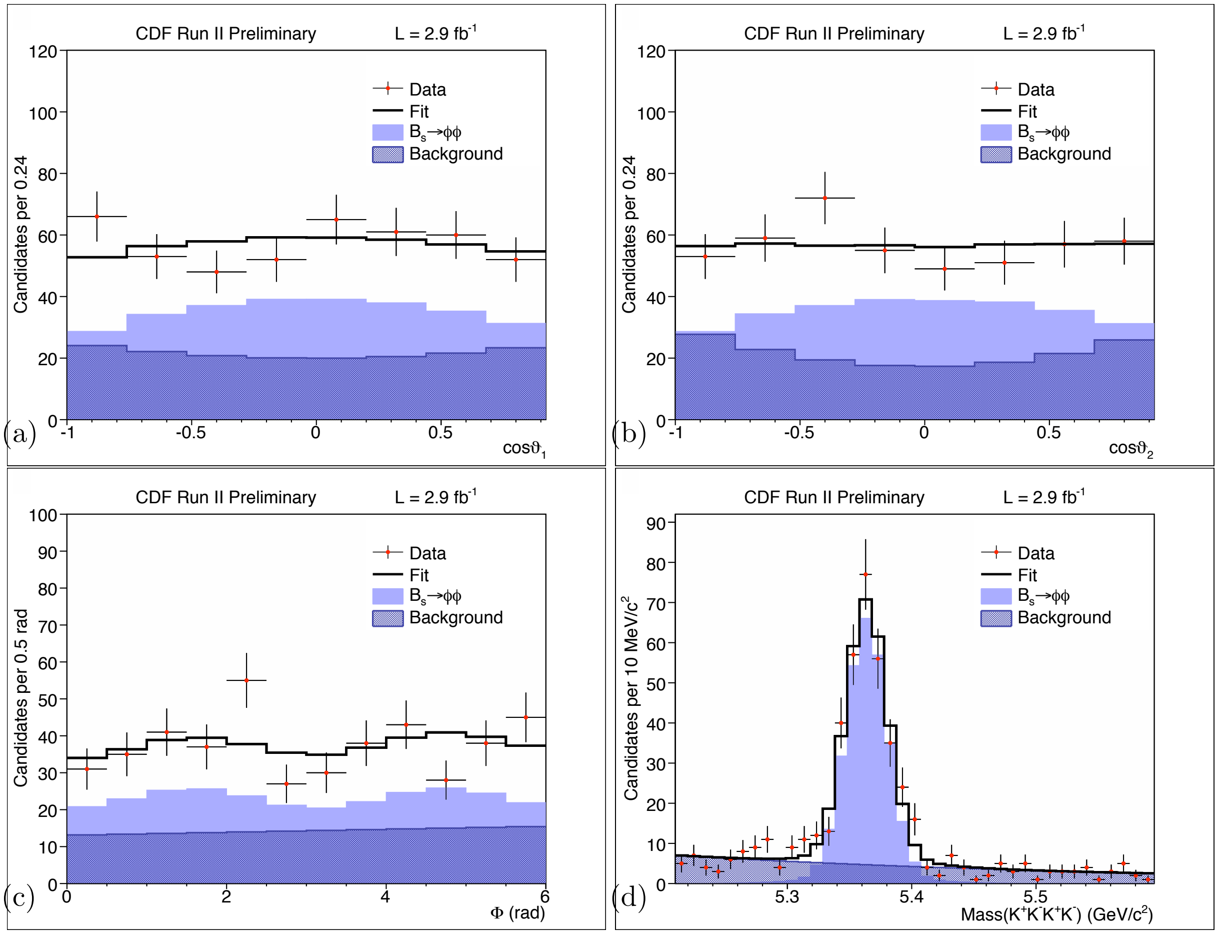

Figure 49: Projections of the time-integrated fit for $B_s^0 \to \phi\phi$: $\cos\vartheta_1$ (a), $\cos\vartheta_2$ (b), $\varPhi$ (c) and the mass (d). The χ^2 probabilities of the fit projections are 0.46, 0.62, 0.11 and 0.07 respectively.

C.3.1 Likelihood scan

The likelihood scans for the polarization amplitudes and the strong phases are reported in fig. 50. The scans for the polarization amplitudes shows the expected parabolic behavior mandatory to be able to have a reliable point estimate. This is not the case for the strong phase: the definition ambiguity can be seen in the likelihood profile, which has two minima ($\delta_{\parallel}$ and $-\delta_{\parallel}$). Since the likelihood scan for $\delta_{\parallel}$ has a non-parabolic shape and because of its biases put in evidence in Sect. C.2.3, we don't consider the point estimate for this quantity when using this fitter version.

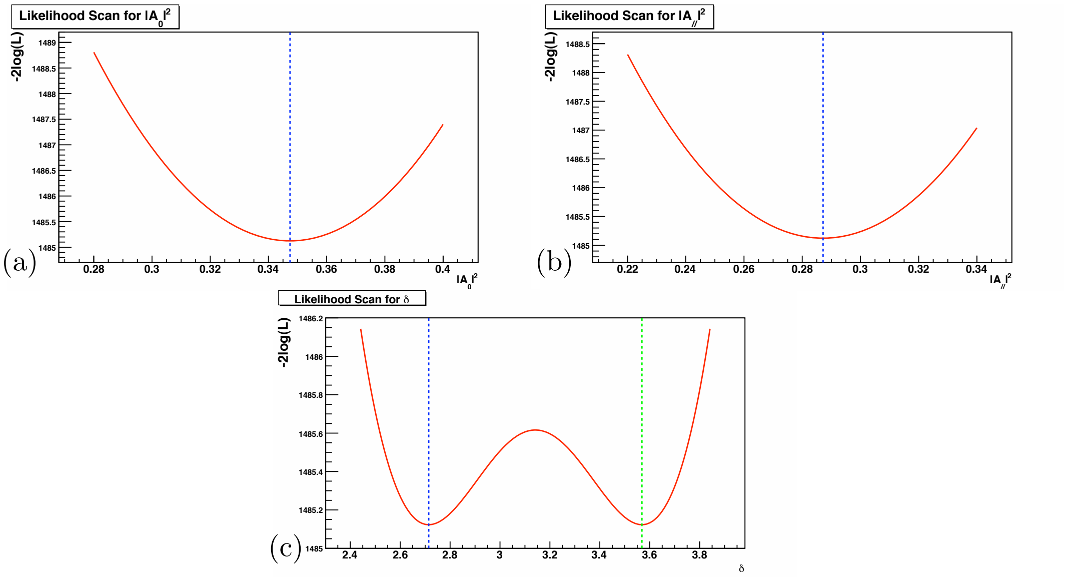

Figure 50: Likelihood scans of the time-integrated fit for $B_s^0 \to \phi\phi$: $|A_0|^2$ (a), $|A_{\parallel}|^2$ (b) and $\delta_{\parallel}$ (c). The blue dotted lines represent the fit estimates; the green dotted line is the point $\pi + \delta_{\parallel}$.

C.3.2 Parameters contour-plots

In fig. 51 we present the contour-plots for the polarization parameters. The plots (a) for $|A_0|^2$ versus $|A_{\parallel}|^2$ is a regular ellipse whose center coordinates are the fit estimates, while the distance of the minimum and maximum points from the center for each axis represents one sigma errors. The plots (b) and (c) present a strange shapes due to the double minima of the likelihood in the $\delta_{\parallel}$ direction.

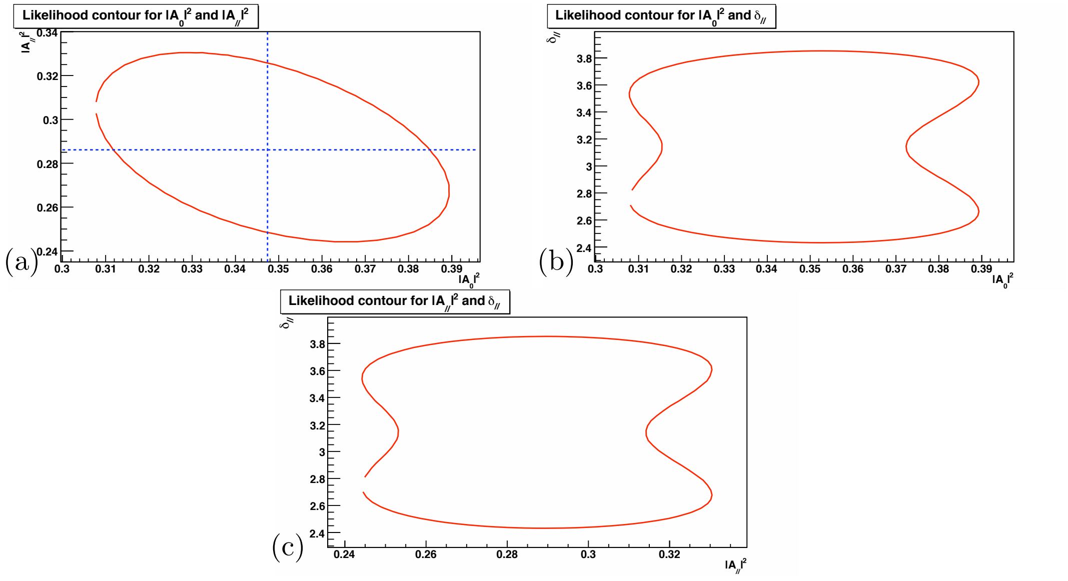

Figure 51: Contour-plots of the time-integrated fit for $B_s^0 \rightarrow \phi\phi$: $|A_0|^2$ versus $|A_{\|}|^2$ (a), $|A_0|^2$ versus $\delta_{\|}$ (b) and $|A_{\|}|^2$ versus $\delta_{\|}$ (c).

D The $B_s^0 \to J/\psi\phi$ analysis details

In this appendix we report the analysis details of the $B_s^0 \to J/\psi\phi$ data sample collected with the TTT. Since most of the technical details are in common with the main analysis, here the presentation is quite schematic, following the same scheme of the main text. The results are reported and commented in Sect. 7.6.

D.1 Mass Model

The signal function has a width of around 10 MeV (see fig. 3). It is parameterized with two gaussian functions having the same mean value M but different resolutions, σ and $k\sigma$:

$$g_{\mathrm{s}}^{(m)} = h\frac{1}{\sqrt{2\pi}\sigma}e^{-\frac{(m-M)^2}{2\sigma^2}} + (1-h)\frac{1}{\sqrt{2\pi}k\sigma}e^{-\frac{(m-M)^2}{2k^2\sigma^2}} \tag{63}$$

where h is the fraction of one gaussian component with respect to the other. Fitting the Monte Carlo events of fig. 52 we obtained the parameters summarized in tab. 32 . In the final fit the multiplicative factor k and the fraction h are fixed, while the other parameters are left free.

Parameter	MC fit value
M [GeV/c^2]	5.36899 ± 0.00002
σ [GeV/c^2]	0.00845 ± 0.00002
k	3.00 ± 0.03
h	0.942 ± 0.002

Table 32: Parameters of MC data mass fit for $B_s^0 \to J/\psi\phi$.

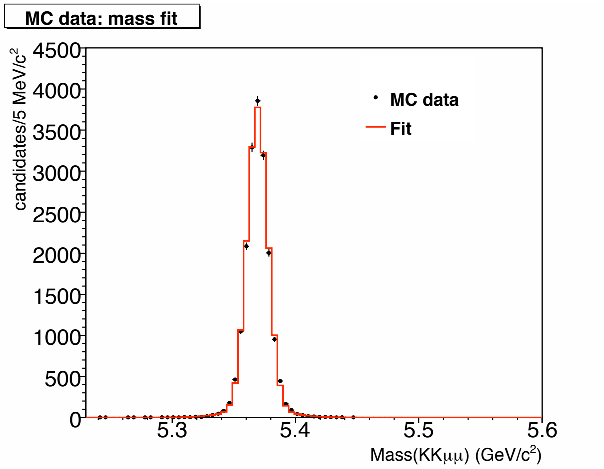

Figure 52: Mass fit of MC data for $B_s^0 \to J/\psi\phi$. The black points are the MC data; the red line is the resulting fit distribution.

The mass background follows an exponentially decreasing behavior:

$$g_{\mathrm{b}}^{(m)} = \frac{b}{e^{-bm_{\mathrm{min}}} - e^{-bm_{\mathrm{max}}}}e^{-bm} \tag{64}$$

where b is the slope of the exponential function, and m spans the interval $[m_{\rm min} = 5.2, m_{\rm max} = 5.6]$ GeV$/c$.

We compare the results of this unbinned maximum likelihood fit of the reconstructed B mass to the others of the binned fit performed in the branching ratio analysis [3]. The data sample is the same for the two fits. Table 33 reports the two fit's results and the mass distributions with the fit function overlaid are shown in fig. 53. The binned fit takes into account for the reflections. We obtain a good agreement in the central values and in the uncertainties for parameters.

Parameter	Unbinned fit	Binned fit
M [GeV/c^2]	5.3656 ± 0.0003	5.3660 ± 0.0003
σ [GeV/c^2]	0.0096 ± 0.0003	0.0094 ± 0.0003
$f_{\rm b}$	0.55 ± 0.01	0.57 ± 0.01
b	-1.1 ± 0.2	-1.2 ± 0.2

Table 33: Comparison of the mass fit results with the branching ratio analysis' ones [3].

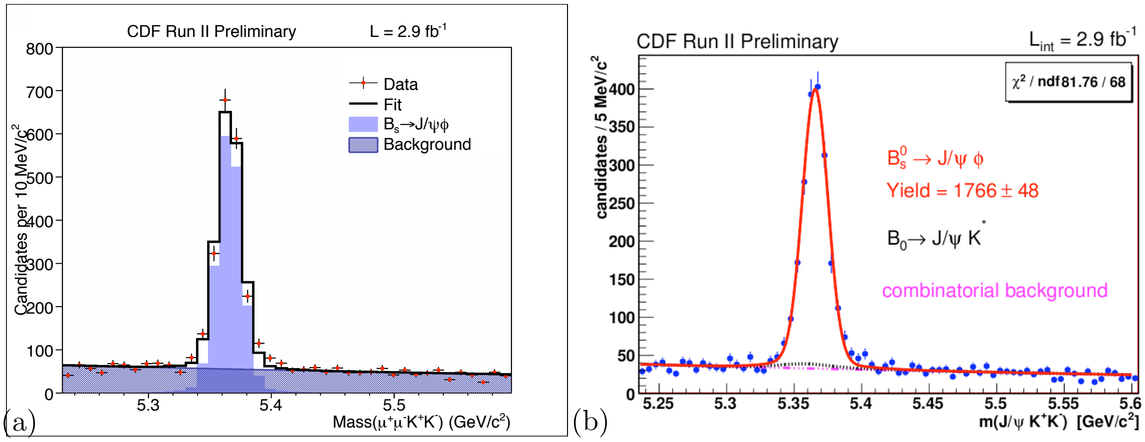

Figure 53: Comparison of our fit result (a) with the one from the branching ratio analysis (b).

D.2 Angular Model

The equation 20 provides the signal angular parameterization, replacing the functions $f_i(\vec{\omega})$ and the phase $\phi_{\rm s}$ by $f_i(\vec{\Omega})$ (eq. 12) and by $2\beta_s$, respectively.

We evaluate the three-dimensional acceptance curve $\mathcal{A}(\vec{\omega})$, which accounts for the angular detector acceptance, constructing the three-dimensional histogram $H(\vec{\omega})$ (about 170000 events of PHSP MC), as we do for the main analysis. The projections of $H(\vec{\omega})$ onto the three axes of the transversity angles basis are shown in fig. 54.

D.2.1 Effect of different trigger path on angular detector angular acceptance

There is the possibility that the acceptance curve is different for the three trigger path selections. We want to check if this is the case: we look at the projections of $H(\vec{\omega})$ for the different trigger paths. They are shown in fig. 55: we can conclude that $H(\vec{\omega})$ is similar for each trigger selections.

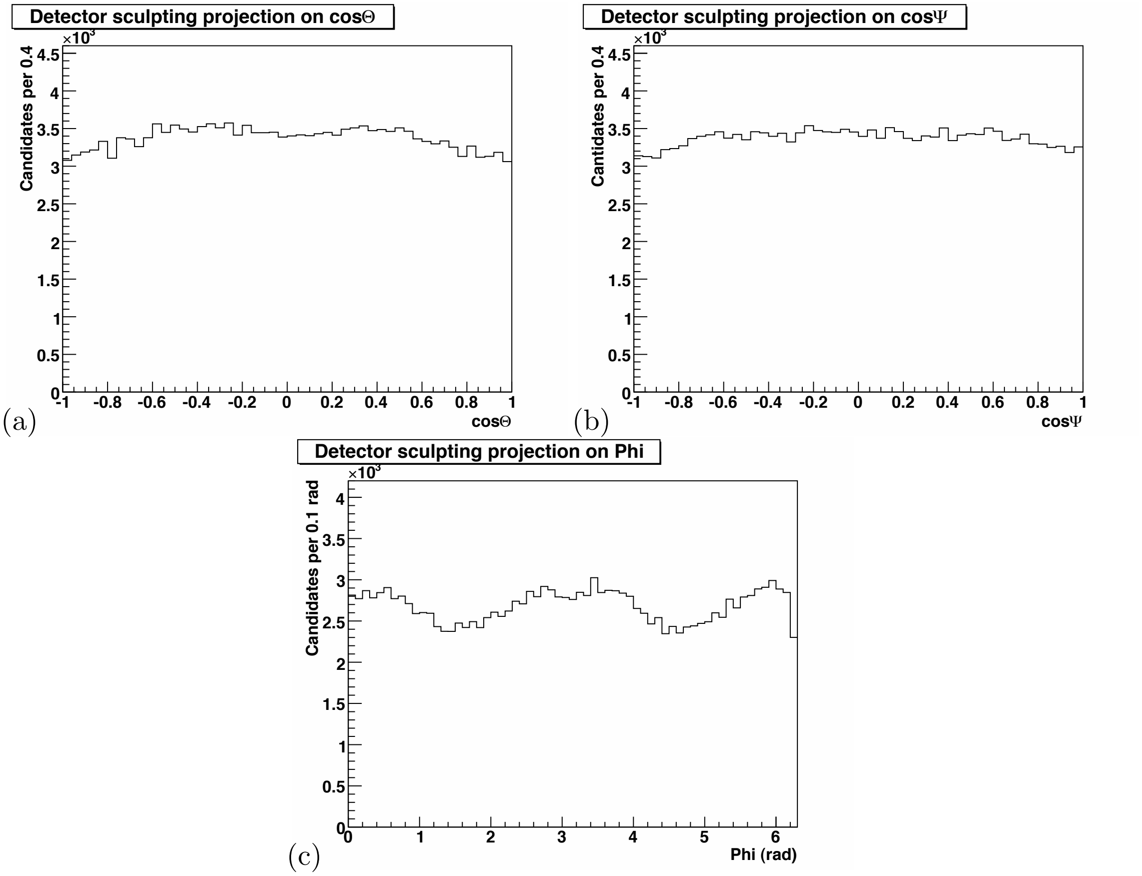

Figure 54: Detector angular acceptance projections: $\cos\Theta$ (a), $\cos\Psi$ (b) and Φ (c).

This test also guarantees no dependencies on the integrated luminosity collected with the three different trigger paths. These allows us to easily combine of all exclusive data sets.

D.2.2 Dependence of the Angular Acceptance on the B Proper Decay Time

We check if there are some dependences of the angular acceptance on the ct of the B, by dividing the MC data sample in three sets (see fig. 17):

- set_1: events which have $ct \in [0.00; 0.05]$ cm;
- set_2: events which have $ct \in]0.05; 0.10]$ cm;
- set_3: events which have $ct \in]0.10; 0.50]$ cm.

For each set, we built the corresponding ct-slice of the angular acceptance. Thus, we compare the three different slices in ct for each $H_i(\vec{\omega})$ projection. They are shown in fig. 56. From these plots there are no evident dependences of the angular acceptance on ct for all angular variables; the tab. 34 presents the the Kolmogorov test on these projections.

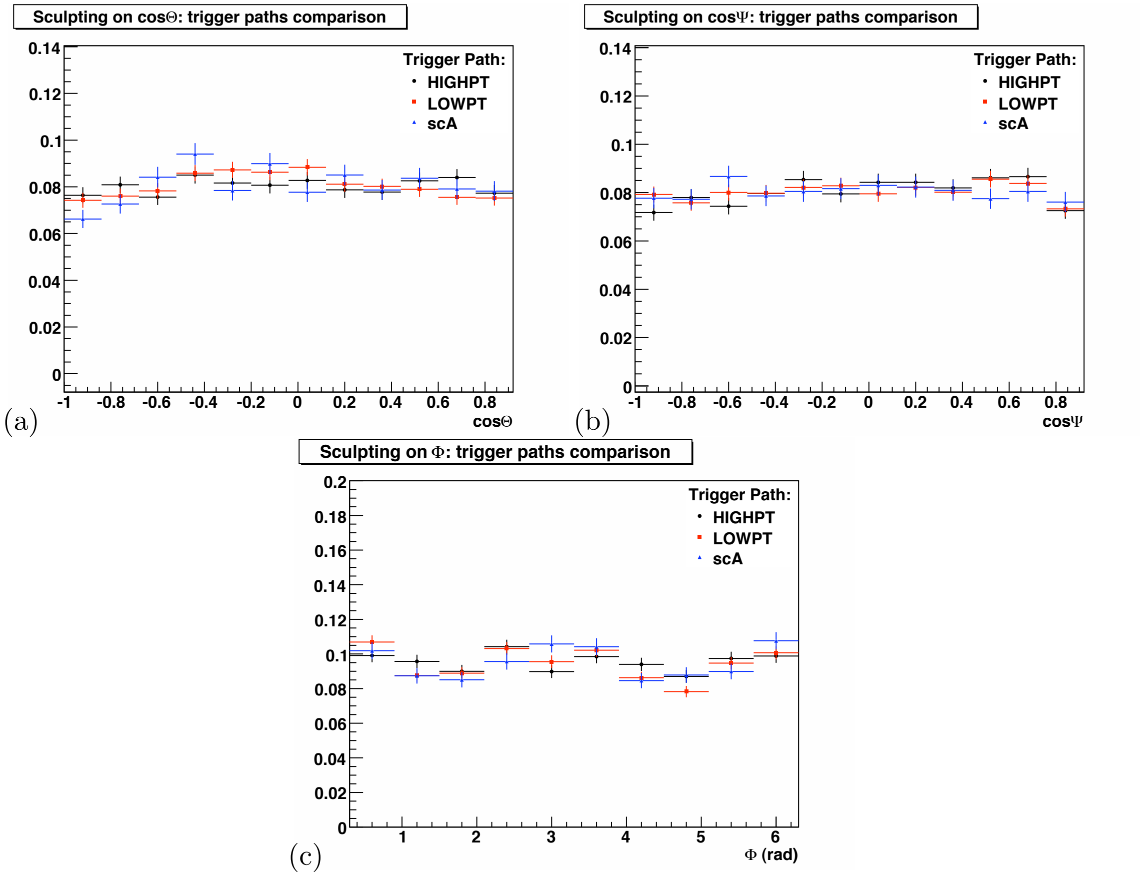

Figure 55: Effect of different trigger path on angular detector angular acceptance: $\cos\Theta$ (a), $\cos\Psi$ (b) and Φ (c).

Variable		Kolmogorov Probability
$\cos\Theta$	set_1 Vs set_2	0.01
	set_2 Vs set_3	0.51
	set_1 Vs set_3	0.95
$\cos\Psi$	set_1 Vs set_2	0.60
	set_2 Vs set_3	0.02
	set_1 Vs set_3	0.26
Φ	set_1 Vs set_2	0.51
	set_2 Vs set_3	0.98
	set_1 Vs set_3	0.71

Table 34: Comparison between three different slices of ct of the angular acceptance for $B_s^0 \to J/\psi\phi$.

D.2.3 Study on the $c\tau$ Dependence of the Angular Acceptance in the Helicity Base

The enhanced $c\tau$ dependence of the angular acceptance in the $B_s^0 \to \phi\phi$ decay is probably due to the particular decay topology and of the specific selection procedure adopted to select the signal. On the other hand, one may argue that the effect of the $c\tau$-dependence is relevant only in the helicity

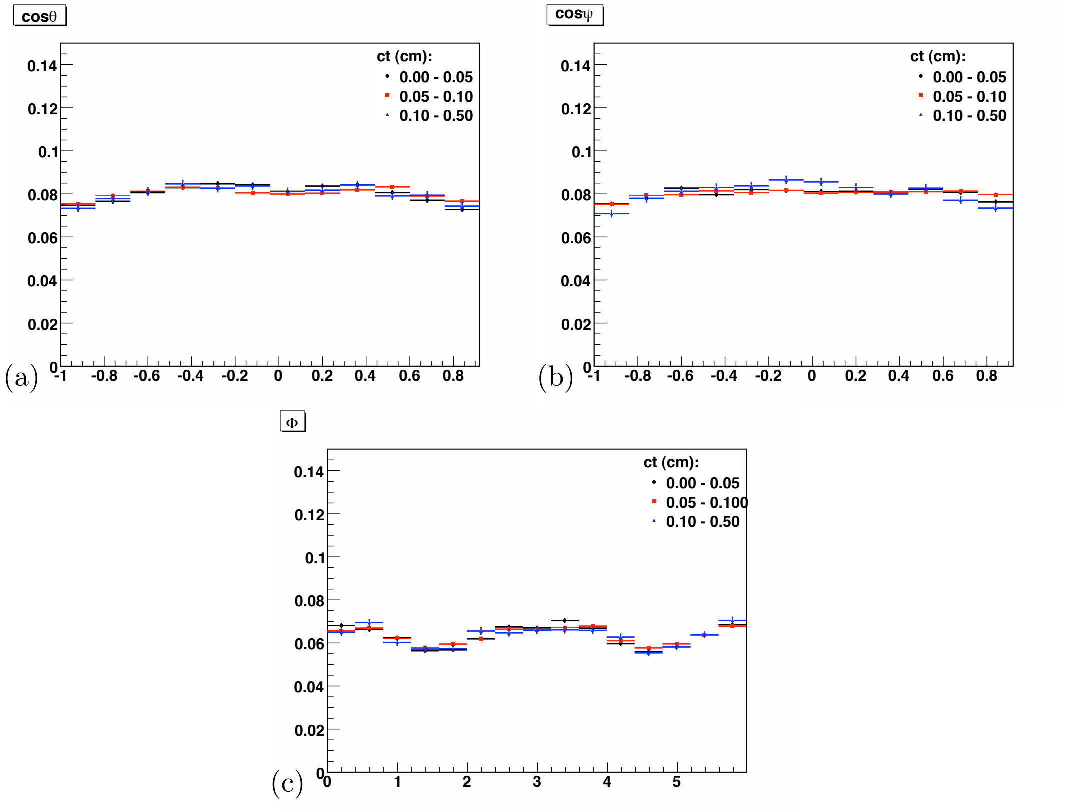

Figure 56: Dependence of detector angular acceptance projections on ct for $B_s^0 \rightarrow J/\psi\phi$: $\cos\Theta$ (a), $\cos\Psi$ (b) and Φ (c).

basis. To better understand this issue, we use the phase space $B_s^0 \rightarrow J/\psi\phi$ MC and we build the angular acceptance histogram and the three ct-slices in the case of the helicity angles. They are shown in fig. 57. We note that $\cos\vartheta_2 = \cos\Psi$. We see that there is no $c\tau$-dependence in the $\cos\vartheta_1$ and ϕ distributions. The situation is analogous to the one in the transversity basis.

If we further impose a selection on the impact parameter of the reconstructed ϕ, mimicking what we have in the $B_s^0 \rightarrow \phi\phi$ analysis, we see that the $c\tau$ dependence increases. This effect supports the hypothesis that the $c\tau$ dependence of the angular acceptance is related to the selection cuts. In fig. 58, we show the plots where the cut $|d_0(\phi)| > 100\,\mu$m is imposed.

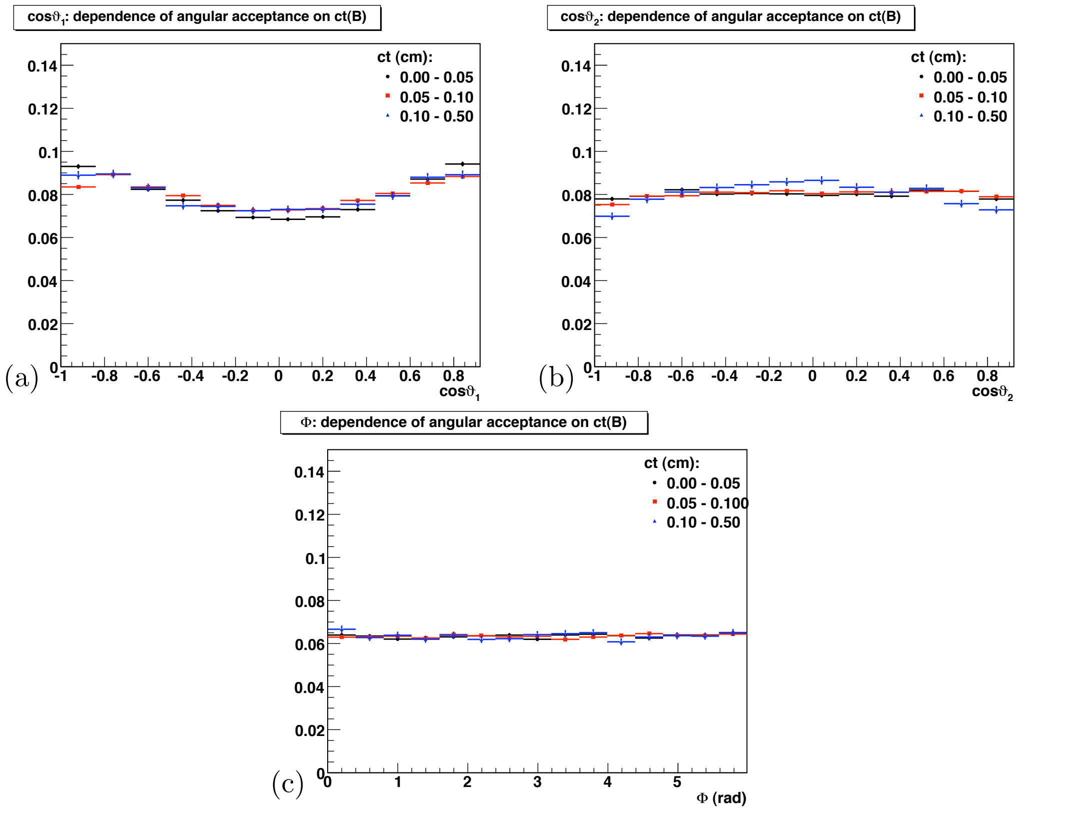

Figure 57: Dependence of detector angular acceptance projections on ct for $B_s^0 \to J/\psi\phi$in the helicity base: $\cos\vartheta_1$ (a), $\cos\vartheta_2$ (b) and ϕ (c).

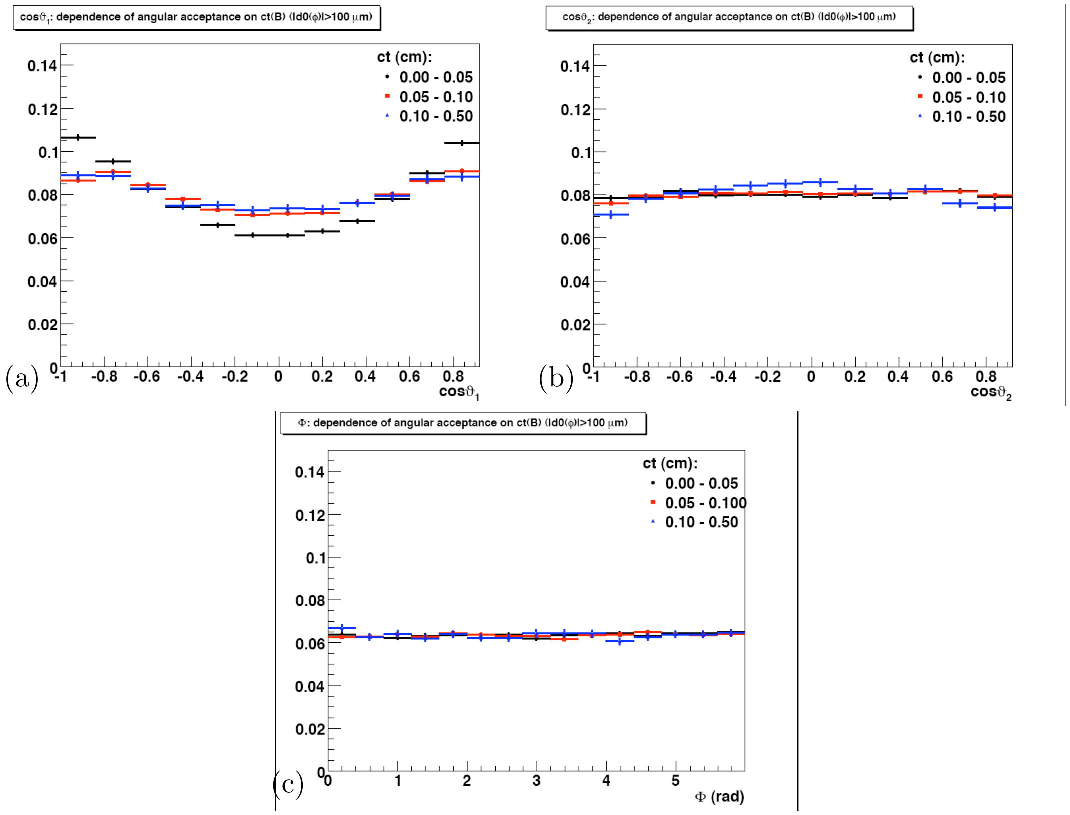

Figure 58: Dependence of detector angular acceptance projections on ct for $B_s^0\to J/\psi\phi$ in the helicity base with $|d_0(\phi)| > 100\,\mu\text{m}$ selection: $\cos\vartheta_1$ (a), $\cos\vartheta_2$ (b) and ϕ (c).

D.2.4 Angular Background parameterization

It is reasonable to suppose that the transversity angles do not have any intrinsic meaning for the combinatorial background. Thus, we use a purely empirical model derived by analysing the angular distributions in the mass sidebands to model the background. Looking at the scatter plots in fig. 59, we see that the angular variables are not correlated in the sideband regions; then the angular part of the background pdf factorizes in the product of three terms:

$$g_{\mathrm{b}}^{(\omega)} = g_{\mathrm{b}}^{(\omega_1)} g_{\mathrm{b}}^{(\omega_2)} g_{\mathrm{b}}^{(\omega_3)} \tag{65}$$

where for the $B_s^0 \to J/\psi\phi$ decay the parameterization adopted are:

$$g_{\mathrm{b}}^{(\omega_1)} = \frac{1}{2(1 + \frac{p_{\Theta}^{(1)}}{3} + \frac{p_{\Theta}^{(2)}}{5})}\left(1 + p_{\Theta}^{(1)} \cos^2\Theta + p_{\Theta}^{(2)} \cos^4\Theta\right), \tag{66a}$$

$$g_{\mathrm{b}}^{(\omega_2)} = \frac{1}{2}\left(1 + p_{\Psi} \cos\Psi\right), \tag{66b}$$

$$g_{\mathrm{b}}^{(\omega_3)} = \frac{1}{5\pi}\left(1 + \frac{1 + p_{\Phi}^{(1)} \cos\Phi}{2} + \frac{1 + p_{\Phi}^{(2)} \cos 2\Phi}{2} + \frac{1 + p_{\Phi}^{(3)} \cos 4\Phi}{2}\right), \tag{66c}$$

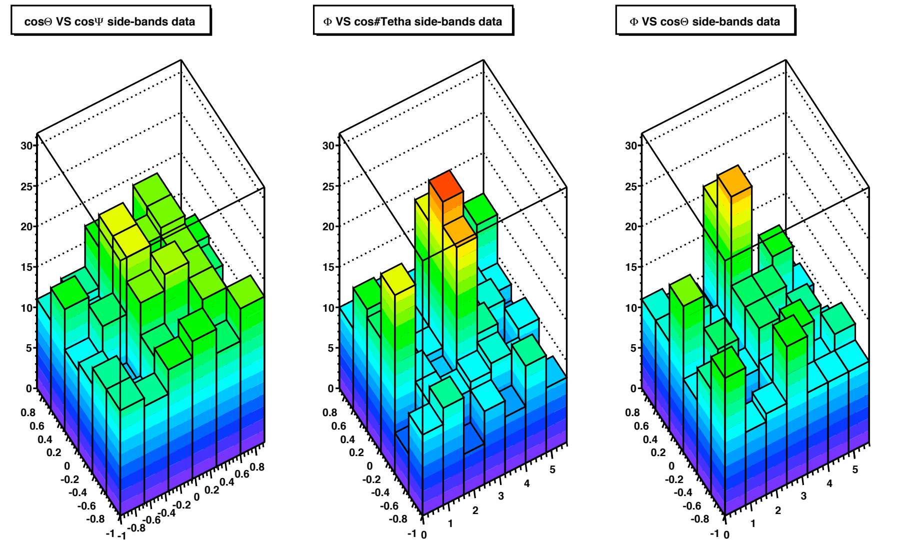

Figure 59: Scatter plots to check for angular variables correlations in the side-band regions. On the right, $\cos\Theta$ versus $\cos\Psi$. In the middle, $\cos\Theta$ versus Φ. On the left, $\cos\Psi$ versus Φ.

We perform a binned fit to the sideband angular distributions using the above equations. Figure 60 shows a binned fit to the sideband angular distributions using the above equations 66.

The parameters $p_j^{(i)}$ are floating in the unbinned fit as background angular parameters; their fitted value are listed in tab. 35.

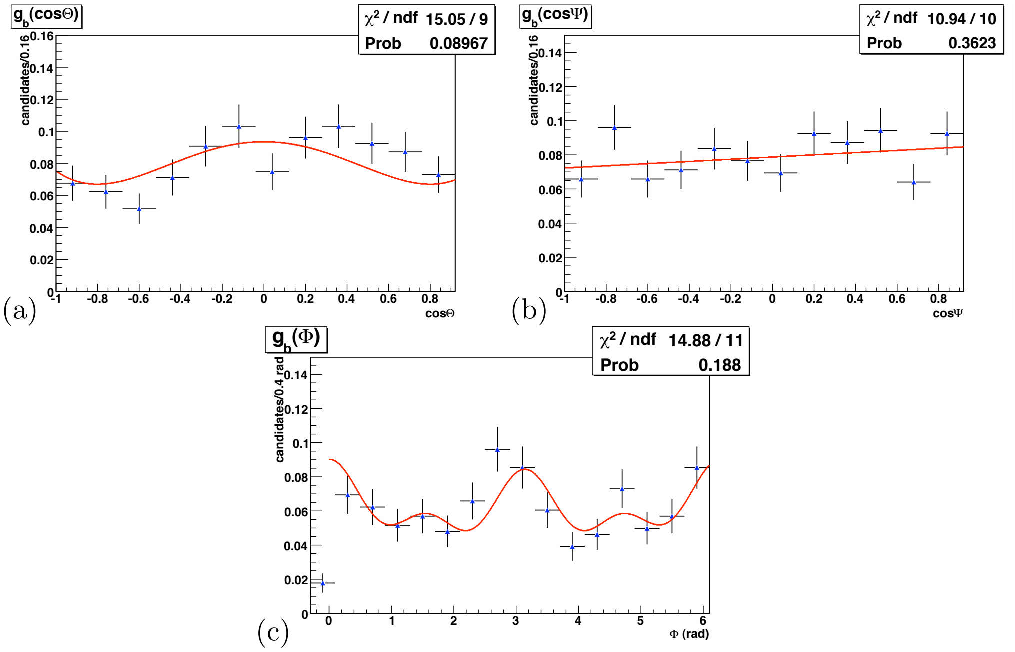

Figure 60: Side-bands data angular fit for background parameterization for the $B_s^0 \to J/\psi\phi$ decay: $\cos\Theta$ (a), $\cos\Psi$ (b) and Φ (c). Black points are side-bands data; red lines are the fitting functions described in the text.

Parameter	fitted value
$p_\Theta^{(1)}$	-0.88 ± 0.21
$p_\Theta^{(2)}$	0.60 ± 0.24
p_Ψ	0.14 ± 0.18
$p_\Phi^{(1)}$	0.88 ± 0.17
$p_\Phi^{(2)}$	0.37 ± 0.17
$p_\Phi^{(3)}$	0.04 ± 0.04

Table 35: Angular background parameters estimated in the unbinned fit for $B_s^0 \to J/\psi\phi$.

D.3 Pulls distributions

We perform the complete fit on 5000 pseudo-experiments of 1000 events each, which is of the same order of the statistic that we have in 2.9 $\text{fb}^{-1}$of data. The results of this test are reported in tab. 36, and the pulls distributions are shown in fig. 61.

We find that the fitter returns unbiased estimates and consistent uncertainties for all parameters except for $\delta_{\|}$, which presents the same strange shape as in the case of the $B_s^0 \to \phi\phi$ analysis.

D.4 Fit to the Realistic MC

The fit to the realistic MC is the second test for the $B_s^0 \to J/\psi\phi$ analysis: we check if the fit returns values consistent with the inputs given in the MC generation (“SVV HELAMP” model).

The results of the fit are satisfactory, since they are very close to the expected values. They are

Parameter	Mean	Variance	Prob(χ^2) [%]
M	0.00 ± 0.03	1.01 ± 0.02	15
σ	0.01 ± 0.03	1.01 ± 0.02	42
f_{b}	-0.02 ± 0.03	0.96 ± 0.02	73
b	-0.06 ± 0.03	0.98 ± 0.02	99
$\|A_0\|^2$	-0.02 ± 0.03	1.03 ± 0.02	17
$\|A_\parallel\|^2$	-0.02 ± 0.03	1.01 ± 0.02	34
$\delta_\parallel$	-0.58 ± 0.03	0.78 ± 0.02	0
$p_\Theta^{(1)}$	-0.02 ± 0.03	1.00 ± 0.02	27
$p_\Theta^{(2)}$	0.01 ± 0.03	1.01 ± 0.02	16
p_Ψ	0.06 ± 0.03	0.97 ± 0.02	33
$p_\Phi^{(1)}$	-0.01 ± 0.03	1.02 ± 0.02	2
$p_\Phi^{(2)}$	0.03 ± 0.03	0.98 ± 0.02	51
$p_\Phi^{(3)}$	0.00 ± 0.03	1.01 ± 0.02	61

Table 36: Pulls mean and variance for $B_s^0 \to J/\psi\phi$ (5000 events per pseudo-experiment). The fourth column presents the χ^2 probability for a gaussian fit of the pulls distribution with mean and variance 0 and 1, respectively.

listed in table 37. The fit projections on the three transversity angles distributions are reported in fig. 62. The distributions are very well reproduced by the fitting functions.

Parameter	generated value	fitted value
$\|A_0\|^2$	0.520	0.5258 ± 0.0053
$\|A_\parallel\|^2$	0.134	0.1380 ± 0.0078
$\delta_\parallel$ [rad]	0.40	0.41 ± 0.13

Table 37: Parameters of realistic MC angular fit for $B_s^0 \to J/\psi\phi$

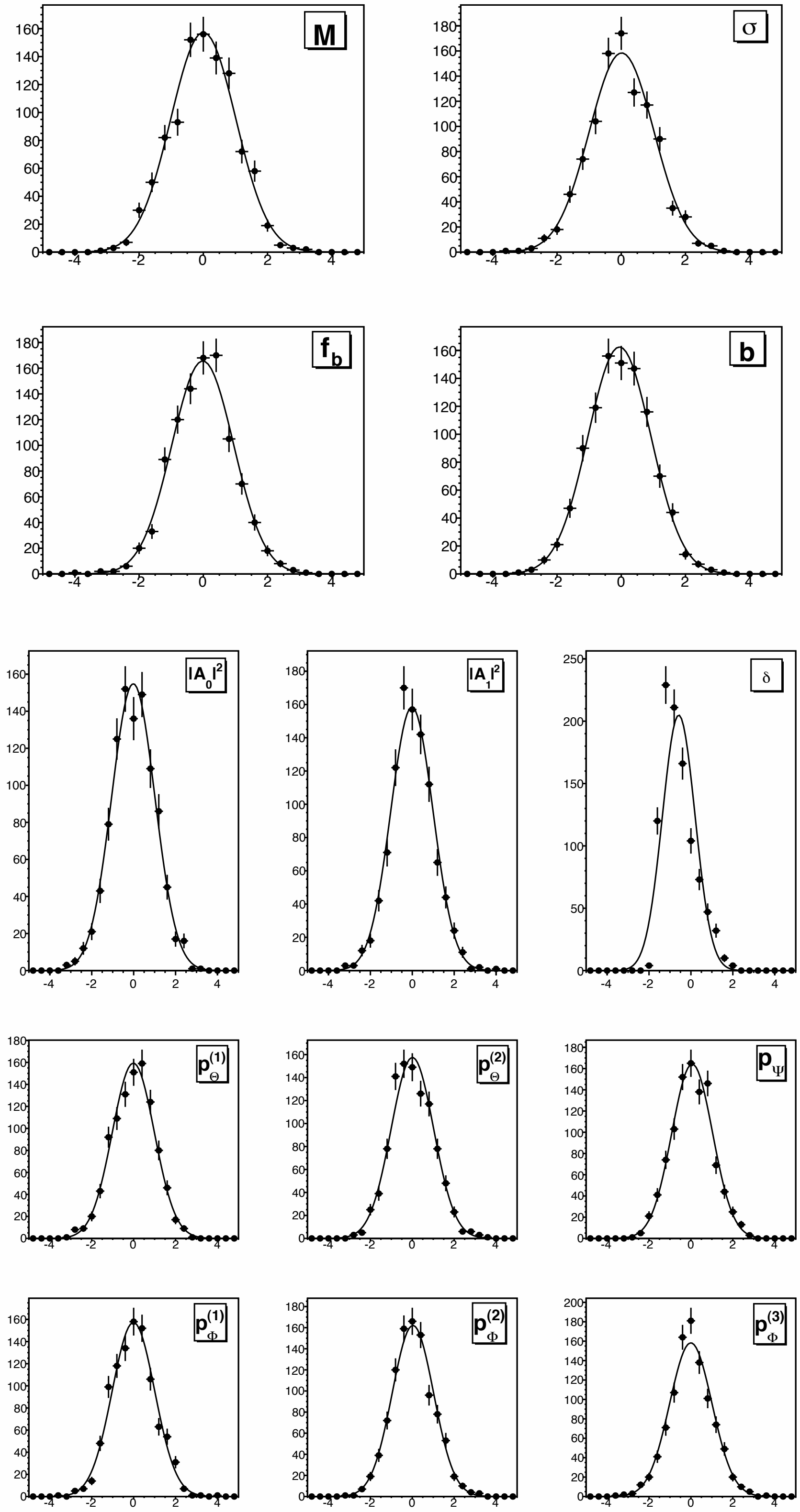

Figure 61: Pulls distributions of the parameters for $B_s^0 \to J/\psi\phi$ (5000 events per pseudo-experiment).

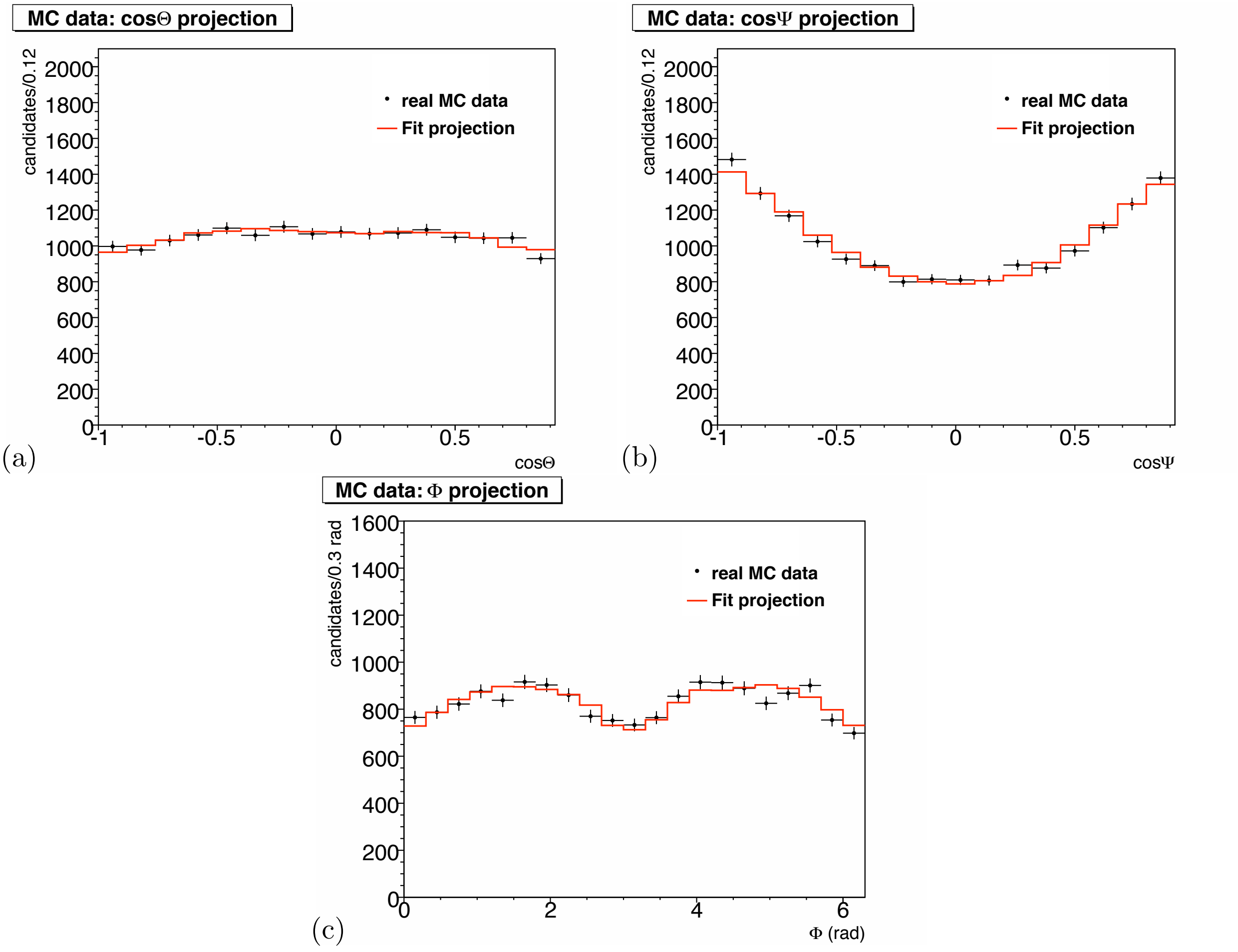

Figure 62: Angular fit projections of realistic MC for $B_s^0 \to J/\psi\phi$: $\cos\Theta$ (a), $\cos\Psi$ (b) and Φ (c). The χ^2 probabilities of the fit projections are 0.81, 0.40 and 0.08 respectively.

E Note on the Test of Goodness of Fit

There is no direct method for testing the goodness-of-fit of an unbinned ML fit. In order to have a feasible estimation of the goodness of our fit, we compare the distributions of data with the joint pdf corresponding to the Likelihood function evaluated with the set of parameters $\vec{\xi} = \hat{\xi}$. We can define the *fit projection* onto the observable x_i as the following one-dimensional function:

$$\mathscr{P}(x_i, \hat{\xi}) = \int g(\vec{x}, \hat{\xi})\, dx_1 \dots dx_{i-1} dx_{i+1} \dots dx_n \tag{67}$$

which is the predicted distribution for x_i under the assumed values for the fit parameters, and it can be overlaid to the experimental data. This allows us to detect possible discrepancies between the observed distributions and our model.

Then, we perform the comparison of the fit projection onto x_i with its data distribution making a χ^2 test. To simplify the notation, x_i is called z. Then:

- we construct the z distribution, filling an histogram of M bins of (constant) width Δ. Each bin is identified by the point (z_j, w_j), where z_j and w_j are the central value and the content of the j-th bin, respectively;
- we build an equivalent M-bins-histogram, evaluating the expected content $w_j^{(e)}$ of each bin with the projection $\mathscr{P}(z, \hat{\xi})$. This is defined by:

  $$w_j^{(e)} = \big(\mathscr{P}(z_j, \hat{\xi})\Delta\big)N; \tag{68}$$

  where N is the total number of events.[10]
- the χ^2 is

  $$\chi^2 = \sum_j^M \frac{\big(w_j - w_j^{(e)}\big)^2}{w_j}; \tag{69}$$
- we evaluate the probability of the given χ^2, whose degrees of freedom are $M-1$, since the normalization is fixed by the number of events N.

Thus, when a χ^2 probability for the unbinned ML fit is reported, it refers to the one computed with the above procedure. The test returns a rough evaluation of the goodness-of-fit, since it doesn't take into account for the correlations among the variables: it has to be considered only as a qualitative indicator.

---

[10] If there is only one observable per event, then $N = n$. In general, for each event i corresponds a vector of observables $\vec{x_i} = (x_1^{(i)}, \dots, x_l^{(i)})$.

F EvtGen decay files

Example decay files for the realistic $B_s^0 \rightarrow J/\psi\phi$ MC sample are reported here:

```
Decay anti-B_s0
1.000000 J/psi phi SVV_HELAMP 0.665057 2.948 0.728011 0.0 0.166429 0.237;
Enddecay
Decay B_s0
1.000000 J/psi phi SVV_HELAMP 0.166429 0.237 0.728011 0.0 0.665057 2.948;
Enddecay
Decay J/psi
1.000000 mu+ mu- PHOTOS VLL;
Enddecay
Decay phi
1.0000 K+ K- VSS;
Enddecay
End
```

For the $B_s^0 \rightarrow \phi\phi$ case many different polarization have been used. The sample with similar polarization (sample DG0a described in 9.9) as in our default fit has the following decay file:

```
Decay anti-B_s0
1.000000 phi phi SVV_HELAMP 0.787961 2.939104 0.589067 0.0 0.179215 1.08481;
Enddecay
Decay B_s0
1.000000 phi phi SVV_HELAMP 0.179215 1.08481 0.589067 0.0 0.787961 2.939104 ;
Enddecay
Decay phi
1.0000 K+ K- VSS;
Enddecay
End
```

When dealing with effects induced by $\Delta\Gamma_s$ we generated a sample completely CP-even (in the limit of no CP violation) by taking only longitudinal and tranverse parallel polarization and add, with relative proportion fixed by the amount of transverse perpendicular polarization, a sample completely CP-even. Examples of the former is:

```
Decay anti-B_s0
1.000000 phi phi SVV_HELAMP 0.475753 2.71 0.73981 0.0 0.475753 2.71;
Enddecay
Decay B_s0
1.000000 phi phi SVV_HELAMP 0.475753 2.71 0.73981 0.0 0.475753 2.71;
Enddecay
Decay phi
1.0000 K+ K- VSS;
Enddecay
End
```

while an example of the completely CP-odd is given below:

```
Decay anti-B_s0
1.000000 phi phi SVV_HELAMP 0.707107 3.141593 0.0 0.0 0.707107 0.0;
Enddecay
Decay B_s0
1.000000 phi phi SVV_HELAMP 0.707107 0.0 0.0 0.0 0.707107 3.141593;
Enddecay
Decay phi
1.0000 K+ K- VSS;
Enddecay
End
```

References

[1] CDF Collaboration: T. Aaltonen. Measurement of Lifetime and Decay-Width Difference in $B_s^0 \to J/\psi\phi$ Decays. *Physical Review Letters*, 100:121803, 2008.

[2] CDF Collaboration and D. Acosta. First Evidence for $B_s^0 \to \phi\phi$ Decay and Measurements of Branching Ratio and A_{CP} for $B^+ \to \phi K^+$. *Physical Review Letters*, 95:031801, 2005.

[3] Benedetto Di Ruzza, Lorenzo Ortolan, Giacomo Artoni, Mirco Dorigo, Marco Rescigno, and Anna Maria Zanetti. Study of the $B_s \to \phi\phi$ decay and measurement of its Branching Ratio. *CDF Internal Note*, 9743, 2009. unpublished.

[4] Gianluca De Lorenzo and Marco Rescigno. Polarization amplitudes in $B_d \to J/\psi K^\star$ and $B_d \to \phi K^\star$ using the Two Track Trigger. *CDF Internal Note*, 8501, 2006.

[5] The Belle Collaboration: K. F. Chen. Time-Dependent CP-Violating Asymmetries in $b \to s\bar{q}q$ Transitions. *Physical Review D*, 72:012004, 2005.

[6] The BABAR Collaboration and B. Aubert. Measurement of the Branching Fraction and the CP-Violating Asymmetry for the Decay $B_0 \to K_S^0\pi^0$. *Physical Review D*, 71:111102, 2005.

[7] The BABAR Collaboration: B. Aubert. Measurement of CP Asymmetries in $B0 \to \phi K^0$ and $B_0 \to K^+K^-K_S^0$ Decays. *Physical Review D*, 71:091102, 2005.

[8] The BABAR Collaboration and B. Aubert. Measurements of Branching Fractions and Time-Dependent CP-Violating Asymmetries in $B \to \eta K$ Decays. *Physical Review Letters*, 94:191802, 2005.

[9] Alakabha Datta and David London. Triple-Product Correlations in $B \to V_1V_2$ Decays and New Physics. *International Journal of Modern Physics A*, 19:2505, 2004.

[10] The BABAR Collaboration and B. Aubert . Measurement of the $B \to \phi K^\star$ Decay Amplitudes. *Phys. Rev. Lett.*, 93(23):231804, Dec 2004.

[11] Katsumi Senyo and for the Belle Collaboration. Search for new physics in $B \to VV$ decays and other hot topics from Belle, 2005.

[12] Y. Chao, P. Chang, and for the Belle Collaboration. Improved Measurements of Partial Rate Asymmetry in $B \to hh$ Decays. *Physical Review D*, 71:031502, 2005.

[13] K. Abe and for the Belle Collaboration. New Measurements of Time-Dependent CP-Violating Asymmetries in $b \to s$ Transitions at Belle, 2004.

[14] The BABAR Collaboration and B. Aubert. Measurements of the Branching Fraction and CP-Violating Asymmetries of $B_0 \to K_S^0\pi^0$ Decays, 2004.

[15] B. Aubert and BABAR Collaboration. Measurements of Branching Fractions and CP-Violating Asymmetries in B-Meson Decays to the Charmless Two-Body States $K^0\pi^+$, $\bar{K}^0K^+$, and $K^0\bar{K}^0$, 2004.

[16] The BABAR Collaboration and B. Aubert. Study of $B_0 \to \pi^0\pi^0$, $B^+ \to \pi^+\pi^0$ and $B^+ \to K^+\pi^0$ decays, 2004.

[17] Xiao-Gang He and Bruce McKellar. Hadron decay amplitudes from $B \to K\pi$ and $B \to \pi\pi$ decays, 2004.

[18] Baek, Seungwon and Hamel, Philippe and London, David and Datta, Alakabha and Suprun, Denis A. $B \to \pi K$ puzzle and new physics. *Phys. Rev. D*, 71(5):057502, Mar 2005.

[19] The BABAR Collaboration and B. Aubert. Vector-Tensor and Vector-Vector Decay Amplitude Analysis of $B^0 \to \phi K^\star$. *Physical Review Letters*, 98:051801, 2007.

[20] The BABAR Collaboration and B. Aubert. Measurements of Branching Fractions, Polarizations, and Direct CP-Violation Asymmetries in $B \to \rho K^\star$ and $B \to f^0(980)K^\star$ Decays. *Physical Review Letters*, 97(20):201801, 2006.

[21] K. F. Chen and for the Belle Collaboration. Measurement of Polarization and Triple-Product Correlations in $B \to \phi K^\star$ Decays. *Physical Review Letters*, 94:221804, 2005.

[22] Ezequiel Alvarez, Luis N. Epele, Daniel Gomez Dumm, and Alejandro Szynkman. Right handed currents and FSI phases in $B^0 \to \phi K^{\star 0}$. *Physical Review D*, 70:115014, 2004.

[23] C. S. Kim and Ya-Dong Yang. Polarization Anomaly in $B \to \phi K^{\star 0}$ and Probe of Tensor Interactions, 2004.

[24] Martin Beneke and Johannes Rohrer and Deshan Yang. Branching fractions, polarisation and asymmetries of $B \to VV$ decays. *Nuclear Physics B*, 774(1-3):64 – 101, 2007.

[25] A. Ali, G. Kramer, Y. Li, C.-D. Lü, Y.-L. Shen, W. Wang, and Y.-M. Wang. Charmless nonleptonic B_s decays to PP, PV, and VV final states in the perturbative QCD approach. *Physical Review D*, 76(7):074018–+, October 2007.

[26] CDF Collaboration: T. Aaltonen. First Flavor-Tagged Determination of Bounds on Mixing-Induced CP Violation in $B_s \to J/\psi\phi$ Decays. *Physical Review Letters*, 100:161802, 2008.

[27] V. M. Abazov et al. Measurement of B_s^0 mixing parameters from the flavor-tagged decay $B_s^0 \to J/\psi\phi$. *Phys. Rev. Lett.*, 101:241801, 2008.

[28] I.I. Bigi and A.I. Sanda. CP *violation*. Cambridge University Press, Cambridge, 2009.

[29] S Amato, J McCarron, F Muheim, B Souza de Paula, and Y Xie. LHCb's sensitivity to New CP-violating Phases in the Decay $B_s \to \phi\phi$. Technical Report LHCb-2007-047. CERN-LHCb-2007-047, CERN, Geneva, May 2007.

[30] Xinqiang Li, Gongru Lu, and Yadong Yang. Charmless $\bar{B}_s \to VV$ Decays in QCD Factorization. *ERRATUM-IBID.D*, 71:019902, 2005.

[31] D. Du and L. Guo. *J. Phys. G: Nucl. Part. Phys.*, 23:525, 1997.

[32] Ahmed Ali, Gustav Kramer, Ying Li, Cai-Dian Lu, Yue long Shen, Wei Wang, and Yu-Ming Wang. Charmless non-leptonic B_s decays to PP, PV and VV final states in the pQCD approach. *Physical Review D*, 76:074018, 2007.

[33] Hai-Yang Cheng, Yong-Yeon Keum, and Kwei-Chou Yang. $B \to J/\psi K^\star$ decays in QCD factorization. *Phys. Rev. D*, 65(9):094023, May 2002.

[34] Mahiko Suzuki. Final-state interactions and s-quark helicity conservation in $B \to J/\psi K^\star$. *Phys. Rev. D*, 64(11):117503, Nov 2001.

[35] Belle Collaboration. *Phys. Rev. Lett.*, 96:171801, 2006.

[36] B. Aubert et al. A Study of $B^0 \to \rho^+\rho^-$ Decays and Constraints on the CKM Angle alpha. *Physical Review D*, 76:052007, 2007.

[37] *BABAR* Collaboration. Measurements of Branching Fraction, Polarization, and Charge Asymmetry of $B^\pm \to \rho^\pm\rho^0$ and a Search for $B^\pm \to \rho^\pm f^0(980)$. *Physical Review Letters*, 97(26):261801, 2006.

[38] *BABAR* Collaboration. b meson decays to $\omega k^\star$, $\omega\rho$, $\omega\omega$, $\omega\phi$, and ωf^0. *Physical Review D (Particles and Fields)*, 74(5):051102, 2006.

[39] *BABAR* Collaboration. Evidence for $B^0 \to \rho^0\rho^0$ Decays and Implications for the Cabibbo-Kobayashi-Maskawa Angle α . *Physical Review Letters*, 98(11):111801, 2007.

[40] Belle Collaboration. Evidence for Neutral B Meson Decays to omega $K^{\star 0}$. *Physical Review Letters*, 101(23):231801, 2008.

[41] *BABAR* Collaboration. Amplitude Analysis of the $B^\pm \to \phi K^{\star\pm}(892)$ Decay. *Physical Review Letters*, 99(20):201802, 2007.

[42] Alakabha Datta, Andrei V. Gritsan, David London, Makiko Nagashima, and Alejandro Szynkman. Testing explanations of the $B \to \phi K^\star$ polarization puzzle. *Physical Review D (Particles and Fields)*, 76(3):034015, 2007.

[43] Prasanta Kumar Das and Kwei-Chou Yang. Data for polarization in charmless $B \to \phi K^\star$: A signal for new physics? *Phys. Rev. D*, 71(9):094002, May 2005.

[44] Amand Faessler, Thomas Gutsche, J. C. Helo, Sergey Kovalenko, and Valery E. Lyubovitskij. Possible resolution of the B-meson decay polarization anomaly in R-parity violating supersymmetry. *Physical Review D (Particles and Fields)*, 75(7):074029, 2007.

[45] *BABAR* Collaboration. Search for $B^0 \to \phi(K^+pi^-)$ decays with large K^+pi^- invariant mass. *Physical Review D (Particles and Fields)*, 76(5):051103, 2007.

[46] Belle Collaboration. Measurements of the Branching Fraction and Polarization in $B^+ \to \rho^+K^\star$ Decays. 95(14):141801, Sep 2005.

[47] The BABAR Collaboration: B. Aubert. Observation of $B^0 \to K^{\star 0}\bar{K}^{\star 0}$ and search for $B^0 \to K^{\star 0}K^{\star 0}$. *Physical Review Letters*, 100:081801, 2008.

[48] C. Amsler et al. Particle Data Group. *Physics Letters B*, 667, 2008 and 2009 partial update for the 2010 edition.

[49] Ch. Paus et al. BottomMods. cdfcodebrowser.fnal.gov/CdfCode/ source/BottomMods/.

[50] K. Anikeev, P. Murat, and Ch. Paus. Description of BGenerator II, 1999. CDF Internal Note 5092.

[51] D. J. Lange. The EvtGen Particle Decay Simulation Package. *Nucl. Instrum. Meth.*, 2001.

[52] CDF Simulation Group. CDF Detector Simulation, 2000. www-cdf.fnal.gov/cdfsim/cdfsim main.html.

[53] The CDF collaboration. Angular Analysis of $B_s \rightarrow J/\psi\phi$ and $B^0 \rightarrow J/\psi K^\star$ Decays and Measurements of $\Delta\Gamma_s$ and ϕ_s. *CDF Pubblic Note*, 8950, 2007.